Manufacturing of lithium-ion battery prototypes through environmentally friendly processes

Auteur : Deckers, Zoé
Promoteur(s) : Job, Nathalie
Faculté : Faculté des Sciences appliquées
Diplôme : Master : ingénieur civil en chimie et science des matériaux, à finalité spécialisée en Chemical Engineering
Année académique : 2022-2023
URI/URL : http://hdl.handle.net/2268.2/17427

University of Liège
Faculty of Applied Sciences

Manufacturing of lithium-ion battery prototypes through environmentally friendly processes

Deckers Zoé

Thesis presented in view of obtaining the degree of
Master in Chemical and Materials Engineering

Supervisor:

Job Nathalie

Academic Year: **2022-2023**

Acknowlegdements

First of all, I am extremely grateful to Professor Nathalie Job for supervising my Master thesis. I would like to thank her for her great availability, her precious advice and her encouragement.

To continue, I would like to thank Cédric Calberg and Alexandre Léonard for agreeing to be part of the jury and for answering my many questions at the laboratory.

I am also grateful to Berke Karaman and Sacris Tambio for showing me how to produce and characterise lithium-ion batteries at the laboratory and for the many useful tips they gave me.

More generally, I would like to thank all the members of the Chemical Engineering Department for their warm welcome and their help in my day-to-day work at the laboratory.

Then, I would like to thank Robert Markowski, PhD student at the Institute of Condensed Matter and Nanosciences of the University of Louvain, for taking the time to show me the three-electrode set up and to perform the associated experiments.

Finally, I would like to thank my family and more precisely my parents for their unconditional support during each step of my studies.

Abstract

The current environmental situation of the world calls for the increasing use of renewable energies to decrease the dependency on fossil resources. However, renewable energies are intermittent and therefore require efficient large-scale storage systems. Such storage systems could be of electrochemical nature. More precisely, lithium-ion batteries could be good candidates due to their high energy density and long life cycle. In addition, lithium-ion batteries have already proven their worth in the field of portable devices.

A lithium-ion battery is composed of a positive and a negative electrode isolated from each other by a separator and in contact with an electrolyte. The lithium-ion battery works on the principle of insertion and deinsertion of lithium ions within the electrode materials and the role of the electrolyte is to transport lithium ions as efficiently as possible between both electrodes. In commercial lithium-ion batteries, the electrolyte is either a liquid or a liquid trapped in a polymer matrix. The classical liquid electrolyte is composed of a lithium salt dissolved in an organic solvent which is a mix of carbonates. The lithium salt present in the electrolyte is highly reactive when put in contact with moisture and this leads to the formation of toxic gaseous components. Concerning the mix of carbonates, it is highly flammable. Even if this classical electrolyte leads to very good electrochemical performances of lithium-ion batteries, the significant safety issues associated cannot be ignored, especially at large-scale.

The objective of this Master thesis was to investigate two safer and greener alternatives to the classical liquid electrolyte for lithium-ion batteries. The first alternative was a semi-solid electrolyte called gel polymer electrolyte, composed of a non-flammable ionic liquid trapped in a polymer matrix. This electrolyte allows to avoid the potential leaks of electrolyte and the associated safety issues. The second alternative investigated was an aqueous electrolyte called water-in-salt electrolyte. It is composed of a highly concentrated lithium salt in water, which allows to widen the electrochemical stability window of water. This aqueous electrolyte therefore discards the safety issues associated to the organic solvent.

The classical liquid electrolyte and the two alternatives were studied from the electrochemical point of view. First, the stability of each electrolyte was investigated. Then, the electrolytes were characterised in combination with $LiFePO_4$ and $Li_4Ti_5O_{12}$ electrodes produced with a water-based manufacturing process. Half-cell and full-cell configurations were assembled and subjected to electrochemical tests. The final objective was to compare the electrochemical performances of the classical liquid electrolyte to those of the gel polymer electrolyte and of the water-in-salt electrolyte.

Résumé

La situation environnementale mondiale actuelle appelle à utiliser de plus en plus d'énergies renouvelables afin de diminuer notre dépendance aux ressources fossiles. Néanmoins, les énergies renouvelables sont intermittentes et nécessitent dès lors des systèmes de stockage à grande échelle efficaces. De tels systèmes de stockage pourraient être de nature électrochimique. Plus précisément, les batteries lithium-ion pourraient représenter une bonne solution de stockage grâce à leur haute densité énergétique et leur longue durée de vie. De plus, les batteries lithium-ion ont déjà fait leurs preuves dans le domaine des appareils portables.

Une batterie lithium-ion est constituée d'une électrode positive et d'une électrode négative, isolées l'une de l'autre par un séparateur et en contact avec un électrolyte. La batterie lithium-ion fonctionne sur le principe d'insertion et de désinsertion des ions lithium au sein des matériaux d'électrodes et le rôle de l'électrolyte est de transporter les ions lithium aussi efficacement que possible entre les deux électrodes. Dans les batteries lithium-ion commerciales, l'électrolyte est un liquide ou un liquide emprisonné dans une matrice polymère. L'électrolyte liquide classique est constitué d'un sel de lithium dissous dans un solvant organique, qui est un mélange de carbonates. Le sel de lithium présent dans l'électrolyte est très réactif lorsqu'il est mis en contact avec de l'humidité, ce qui donne lieu à la formation de produits gazeux toxiques. En ce qui concerne le mélange de carbonates, il est extrêmement inflammable. Même si l'électrolyte classique permet d'obtenir de très bonnes performances électrochimiques pour les batteries lithium-ion, les importants problèmes de sécurité associés ne peuvent pas être négligés, d'autant plus à grande échelle.

L'objectif de cette thèse de Master était d'étudier deux alternatives plus sûres et plus vertes à l'électrolyte liquide classique pour les batteries lithium-ion. La première alternative était un électrolyte semi-solide appelé électrolyte polymère en gel, constitué d'un liquide ionique ininflammable emprisonné dans une matrice polymère. Cet électrolyte permet d'éviter les potentielles fuites d'électrolyte et les problèmes de sécurité associés. La deuxième alternative étudiée était un électrolyte aqueux appelé "water-in-salt". Il est composé d'un sel de lithium très concentré dans de l'eau, ce qui permet d'élargir la fenêtre de stabilité électrochimique de l'eau. Cet électrolyte aqueux supprime les problèmes de sécurité associés au solvant organique.

L'électrolyte liquide classique et les deux alternatives ont été étudiés du point de vue électrochimique. Premièrement, la stabilité de chaque électrolyte a été étudiée. Ensuite, les électrolytes ont été caractérisés avec des électrodes $LiFePO_4$ et $Li_4Ti_5O_{12}$ produites par un procédé de production en voie aqueuse. Des demi-cellules et des cellules complètes ont été assemblées et soumises à des tests électrochimiques. L'objectif final était de comparer les performances électrochimiques de l'électrolyte liquide classique à celles de l'électrolyte polymère en gel et de l'électrolyte "water-in-salt".

Contents

Introduction

Context

Due to the current environmental situation, there is an increasing need for more sustainable energy sources, such as renewable energies, to gradually decrease the dependency on fossil resources. Indeed, fossil resources present the two main disadvantages of being polluting, therefore increasing the impact on global warming, and of being non-renewable. However, most renewable energies are intermittent and quality energy storage systems are thus required for an efficient use of energy. Electrochemical storage systems such as rechargeable batteries are promising candidates for energy storage. More precisely, lithium-ion batteries, which were first commercialised in the 1990s by Sony, have been successfully applied for the portable device market and are expected to be increasingly used in electrical and hybrid vehicles and also for grid storage applications. This success of lithium-ion batteries can be attributed to their numerous advantages such as high energy density, high rate capability and long life cycle [1][2].

A lithium-ion battery is essentially composed of a negative electrode, a positive electrode, an electrolyte which transports lithium ions, and a separator which separates both electrodes from each other. The lithium-ion battery works on the principle of insertion and deinsertion of lithium ions within the positive and negative electrode materials. This working principle is illustrated in Figure I.1. During the charge of the battery, electrons are transferred from the positive electrode to the negative electrode through an external circuit. At the same time, lithium ions are deinserted from the positive electrode and go through the electrolyte and separator to insert into the negative electrode. During the discharge of the battery, the positive and negative electrodes are connected to an external device, which allows electrons to go from the negative to the positive electrode while producing a useful electrical current. Meanwhile, the lithium ions deinsert from the negative electrode, travel through the electrolyte and separator and insert into the positive electrode [3].

The materials used as positive electrode are lithiated compounds, such as lithium metal oxides ($LiCoO_2$), lithium manganese spinels ($LiMn_2O_4$) and olivines ($LiFePO_4$). Concerning the negative electrode, the most used material is graphite, in which the lithium ions from the positive electrode can intercalate. In addition, a more recent alternative to graphite is lithium titanate oxide $Li_4Ti_5O_{12}$ [4]. The crystal structures of common electrode materials can be observed in Figure I.2. The separator is usually a microporous polymeric film or a nonwoven fabric and is placed between the positive and negative electrodes. Its role is to isolate both electrodes from each other to avoid short-circuits while still letting the lithium ions pass through it [5]. Concerning the electrolyte, its role is to conduct lithium

ions between the electrodes. It is classically composed of a lithium salt dissolved in organic solvents. The most commercially used electrolyte is composed of $LiPF_6$ dissolved in a mix of carbonates, such as ethylene carbonate and dimethyl carbonate [5].

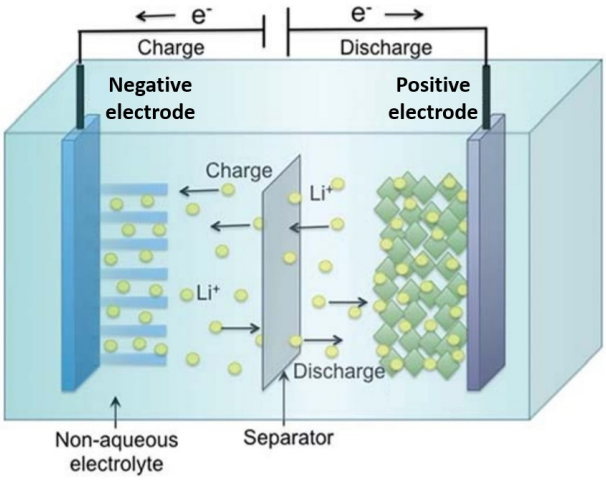

Figure I.1: Schematic representation of the charge and discharge of a lithium-ion battery, modified from [6].

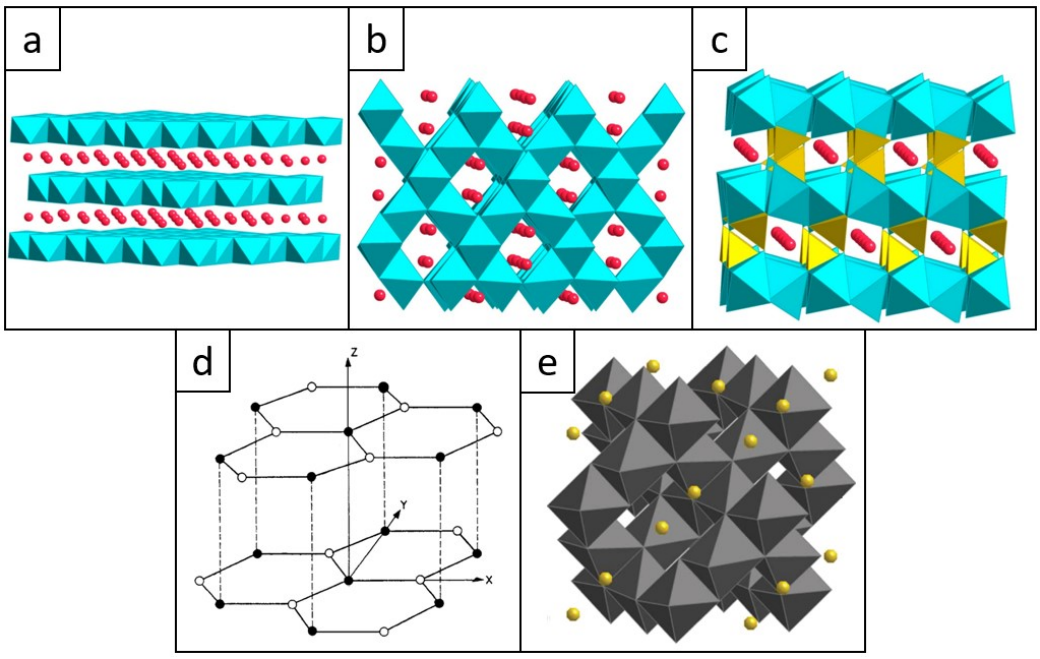

Figure I.2: Crystal structures of common positive electrode materials (red: lithium ions, blue: transition metal ions connected to oxygen ions, yellow: phosphate ions connected to oxygen ions): a) structure of lithium metal oxides such as $LiCoO_2$, adapted from [7], b) structure of spinels such as $LiMn_2O_4$, adapted from [7], c) structure of olivines such as $LiFePO_4$, adapted from [7]. Crystal structures of common negative electrode materials: a) layered structure of graphite, adapted from [8], b) structure of $Li_4Ti_5O_{12}$ (gold: lithium ions, black: titanium ions connected to oxygen ions), adapted from [9].

Safety issues of lithium-ion batteries

Despite the many advantages associated to lithium-ion batteries for energy storage, a lot of safety issues can be associated to them and restrict their commercial use, especially at large-scale. The safety issues can either be attributed to the failure of a single component of the battery or of the overall system due to extreme conditions. A few examples of extreme conditions are overcharge, internal short-circuit due to lithium dendrites, thermal runaway, dissolution of the current collector or gas evolution [3]. Those extreme conditions lead to significant thermal risks within the battery due mostly to the presence of the highly flammable organic electrolyte, which is the most flammable element of the lithium-ion battery. The electrolyte is therefore one of the most important components of the battery concerning safety issues [10].

The classical liquid electrolyte, composed of $LiPF_6$ dissolved in a mix of carbonates, is currently the most used commercially due to its good electrochemical performances and its low-cost. However, its safety is unsatisfactory due to both the lithium salt and the solvent. The lithium salt $LiPF_6$ is thermally unstable and highly sensitive to the presence of moisture, leading to the formation of PF_5, which is a strong Lewis acid capable of reacting with the solvent and decomposing it. In addition, the presence of moisture can lead to the formation of HF, which is highly corrosive and toxic [10][11]. Concerning the carbonates, the safety issues are associated to their very high flammability, especially when the batteries are subjected to extreme conditions and that electrolyte vapors leak out of the battery [10][12][13].

Alternative electrolytes

To develop the applications of lithium-ion batteries at large-scale, improvements have to be made in terms of safety and environmental impacts of the electrolyte. If the objective is to keep a liquid organic electrolyte, $LiPF_6$ could be replaced by a more stable lithium salt and additives could be added to the solvent to reduce its flammability. If an alternative to the liquid organic electrolyte is sought, different possibilities could be considered [10].

An alternative to the liquid organic electrolyte could be polymer electrolytes which can be subdivided in two categories: the solid polymer electrolytes and the gel polymer electrolytes. Both types of polymer electrolytes are present in solid or semi-solid state and therefore remove the risks of leakage of electrolyte and the associated flammability issues. The solid polymer electrolyte is a solid state electrolyte composed of a lithium salt dissolved in a polymer matrix. This electrolyte enhances the safety of batteries but has a low ionic conductivity due to its solid state. The gel polymer electrolyte is a semi-solid electrolyte, which consists in a liquid electrolyte trapped within a polymer matrix. This type of electrolyte combines the properties of solid and liquid electrolytes and presents an ionic conductivity which can be very close to that of the liquid organic electrolyte. The gel polymer electrolyte therefore represents a promising electrolyte material for lithium-ion batteries [10][14].

Another alternative to the liquid organic electrolyte could be an aqueous electrolyte. Aqueous electrolytes remove completely the flammable property of the electrolyte, therefore increasing the safety of lithium-ion batteries and rendering them more environmentally friendly. However, it is known that aqueous electrolytes have a narrow electrochemical stability window due to the decomposition of water through the oxygen and hydrogen evolution reactions. This therefore limits the voltage and power which can be delivered by batteries containing such electrolytes [10][15]. This issue led to research concerning the widening of the electrochemical stability window of aqueous electrolytes and resulted in the introduction of a new class of aqueous electrolytes: the water-in-salt electrolyte. The water-in-salt electrolyte consists in a highly concentrated lithium salt in water. This high concentration of salt allows to widen the stability window of the electrolyte, for example up to 3 V for a 21 mol/$kg_{solvent}$ LiTFSI aqueous solution. This can therefore improve the electrochemical performances of batteries in comparison to classical aqueous electrolytes [16].

Objectives and plan of the Master thesis

The main objective of the Master thesis was to study safer and greener electrolyte alternatives for lithium-ion batteries, namely the gel polymer electrolyte and the water-in-salt electrolyte. The lithium-ion batteries investigated were composed of a lithium iron phosphate positive electrode and a lithium titanate oxide negative electrode, both produced through a water-based manufacturing process. The electrochemical performances of the electrodes with three different electrolytes, the classical liquid organic electrolyte, the gel polymer electrolyte and the water-in-salt electrolyte, were studied and compared.

The Master thesis was realised at the Nanomaterials, Catalysis and Electrochemistry (NCE) laboratory of the University of Liège and is divided in four main chapters.

Chapter 1 focuses on the production process of the lithium iron phosphate and the lithium titanate oxide electrodes. The production process was a water-based process developed by the NCE laboratory [17]. The electrodes were produced by manufacturing an aqueous ink which was then sprayed on current collectors. In addition, the surface of the electrodes was studied through contact profilometry.

Chapter 2 studies each electrolyte separately: the classical liquid organic electrolyte, the gel polymer electrolyte and the water-in-salt electrolyte. For the gel polymer and the water-in-salt electrolytes, their synthesis was realised at the laboratory. For each electrolyte, the electrochemical stability was studied through cyclic voltammetry in two-electrode configuration and, when possible, in three-electrode configuration. The stability results were then analysed and compared.

Chapter 3 focuses on the electrochemical characterisation of the electrodes and the electrolytes in half-cell configurations. Coin cells were assembled for each type of material as positive electrode and with lithium metal as negative electrode, for each electrolyte except the water-in-salt electrolyte. The coin cells were subjected to galvanostatic cycling and cyclic voltammetry to study and compare the electrochemical performances. Concerning

the water-in-salt electrolyte, it was characterised with lithium iron phosphate as positive electrode and activated carbon fabric as negative electrode in a three-electrode system.

Finally, Chapter 4 investigates the electrochemical performances of full-cells composed of lithium iron phosphate as positive electrode, lithium titanate oxide as negative electrode and each type of electrolyte. The systems studied were once again coin cells and were subjected to galvanostatic cycling and cyclic voltammetry. The performances obtained for each electrolyte were then analysed.

CHAPTER 1

Electrode manufacturing

1.1 Introduction

A lithium-ion battery electrode is a composite electrode consisting of four main components: an active material, a binder, a carbon additive and a current collector. A schematic representation of a composite lithium-ion battery electrode can be seen in Figure 1.1. The active material is an intercalation material which stores the lithium ions during the insertion and deinsertion reactions and is therefore responsible for the capacity of the battery. The binder is a polymer which holds together the electrode material, present in the form of a powder. It also allows the material to stick to the current collector and gives mechanical stability to the electrode. Due to both the insulating properties of the polymer binder and the lack of conductive property of the active material, a carbon additive is often added to improve the electronic conductivity of the electrode. Finally, the current collector plays the role of the substrate for the electrode material and conducts the electrons from/towards an external electrical circuit during the charge and discharge processes [18][19].

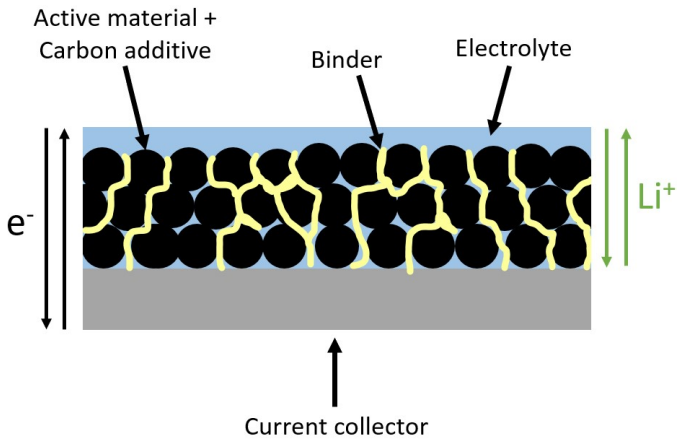

Figure 1.1: Structure of a composite electrode, adapted from [20].

The classical manufacturing process of the composite electrode can be divided in two main steps: the active material slurry preparation and the electrode film formation [19].

The active material slurry preparation consists in mixing the active material, carbon additive and binder with a solvent to obtain a liquid slurry. The mixing step is important to obtain an adequate homogeneity of the slurry and to monitor the viscosity based on the desired casting method [19].

The electrode film formation consists in first casting the slurry on the current collector. This deposition of the slurry can be performed in various ways: slot-die coating, doctor blade, spraying, screen-printing. Once the slurry is casted on the current collector, the solvent must be evaporated through a controlled heating process. Finally, the electrode is potentially subjected to a calendering process during which the electrode is pressed to decrease its porosity and achieve a desired thickness and density [18][19].

This classical manufacturing route is applied industrially and presents some disadvantages, especially concerning the type of binder and solvent used. The most used binder is PVDF (polyvinylidene fluoride), a highly electrochemically stable fluoropolymer. This binder is not soluble in water and requires an organic solvent for its dissolution. The most used solvent is NMP (N-methyl-2-pyrrolidone), which is known to be toxic, flammable and expensive. The use of PVDF and NMP is therefore problematic in terms of sustainability of battery manufacturing since a toxic solvent is used in the electrode processing but also has to be recovered during the solvent removal step [18][19]. In addition, the recycling of the electrodes at the end of life of the batteries is highly impacted by the presence of the PVDF binder. Two methods can be used to remove PVDF from the electrodes: dissolution or pyrolysis. When dissolution is considered, PVDF is highly stable and has a low solubility in most solvents, which means that its separation from the other electrode materials is difficult. Only a few solvents can be used to dissolve PVDF, such as NMP and N,N-dimethylformamide, which are once again highly toxic. Less toxic solvents could also be used such as Cyrene and triethyl phosphate. However, large quantities are required due to the very low solubility of PVDF and high temperatures might also be needed. Concerning the pyrolysis of PVDF, it generates highly toxic hydrogen fluoride gases [18].

Those issues have increased research towards sustainable electrode manufacturing processes, especially towards water-based processes which thus require the use of a water-soluble binder. One of the main challenges concerning this water-soluble binder is that it has to remain stable during battery operation. A few examples of water-soluble binders investigated in the literature are: sodium alginate, guar gum, xanthan gum and carboxymethyl chitosan [18][19].

Within this scope, the NCE laboratory of the University of Liège has performed research and has patented a water-based process for the preparation of composite electrodes [17]. This process involves the use of xanthan gum as binder and MilliQ water as solvent. The active material is mixed with the binder, the carbon additive and MilliQ water to obtain an homogeneous slurry which can then be casted on current collectors. The aqueous slurry formulation developed by the NCE laboratory contains for example 12.2 wt% solids and a classical solid composition follows the following weight percentages: 75% of active material, 20% of conducting carbon and 5% of binder [21].

This chapter focuses on the production of composite electrodes following the water-based

manufacturing process developed at the NCE laboratory.

First, the positive and negative electrode materials were selected based on their characteristics. Afterwards, the aqueous slurry was produced following the water-based process. This slurry was then sprayed by a robot on current collectors to obtain the composite electrodes. A target active material mass for each material had to be determined beforehand based on electrode balancing. Knowing this material mass allowed to stop the spray-coating process when the required mass was reached. Then, the composite electrodes were dried, weighed and stored in an argon-filled glovebox. Finally, the electrodes were characterised through contact profilometry. This technique allows to study the surface height of the electrodes and to obtain an estimation of the void fraction of the electrodes.

1.2 Experimental

1.2.1 Materials selection

Two main active materials were considered in this work: lithium titanate oxide $Li_4Ti_5O_{12}$ (LTO) as negative electrode and lithium iron phosphate $LiFePO_4$ (LFP) as positive electrode. Both of these materials are intercalation materials, in which lithium ions insert and deinsert during the redox reactions [22].

Lithium titanate oxide is a promising negative electrode material for lithium-ion batteries and is a good candidate to replace the more classical graphite material. The insertion and deinsertion of lithium ions in LTO take place at a potential of about 1.55 V *vs.* Li^+/Li, according to the reaction depicted by Equation 1.1. Three lithium ions are exchanged during the reaction and lead to a theoretical capacity of 175 mAh/g [23].

$$Li_4Ti_5O_{12} + 3Li^+ + 3e^- \longleftrightarrow Li_7Ti_5O_{12} \tag{1.1}$$

The insertion/deinsertion reaction takes place at a potential higher than that of graphite, which is below 1 V *vs.* Li^+/Li. This higher potential allows to avoid the decomposition of the carbonates of the classical liquid electrolyte and their reaction with the negative electrode surface, which leads to the formation of the solid-electrolyte interface (SEI). The SEI is a protective layer usually formed on the graphite negative electrode during the first charge-discharge cycles of the battery. Its production decreases the total capacity of the battery and the formed layer shows a resistance to the passage of lithium ions, which leads to a decrease in the capacity as numerous cycles are performed. The presence of this layer is therefore not beneficial and the use of LTO allows to avoid it. In addition, the higher potential of LTO is further away from that of lithium metal and the risks of reduction of lithium ions into lithium metal are decreased. The formation of lithium dendrites and the associated internal short-circuits are therefore less likely to occur [23][24].

LTO is called a "zero strain" material due to its extremely low volume change during the insertion and deinsertion of lithium ions [23]. Indeed, the volume change of LTO is lower than 0.2% while the volume change of the more conventional negative electrode material, graphite, can go up to 12% [25]. This entails that LTO has a better structural stability and

allows to produce batteries with longer cycle life and higher rate capability than graphite [23]. Finally, LTO is also nontoxic and inexpensive. Those advantages make it an attractive negative electrode material [2].

Two main disadvantages of LTO can be pointed out. First, due its higher working potential than graphite, it leads to batteries with a lower output voltage. Second, its electrical conductivity is very low ($< 10^{-13}$ S/cm). However, this last disadvantage can be counterbalanced by the addition of a conducting additive during the electrode manufacturing process [23].

Lithium iron phosphate is an attractive positive electrode material for lithium-ion batteries. The insertion and deinsertion of lithium ions in LFP take place at a potential of about 3.45 V *vs.* Li^+/Li, following the reaction depicted by Equation 1.2. One lithium ion is exchanged during the reaction and this leads to a theoretical capacity of LFP of 170 mAh/g [21][26].

$$LiFePO_4 \longleftrightarrow FePO_4 + Li^+ + e^- \tag{1.2}$$

LFP presents advantages which make it attractive in comparison to the more conventional $LiCoO_2$ (LCO) positive electrode material used commercially. Firstly, LFP has an olivine structure which presents a good structural stability upon cycling, leading to a long cycle life and a good cycling stability. In comparison, LCO has a layered crystal structure which is distorted upon cycling and therefore leads to a lower cycle life than LFP. To continue, LFP is less toxic than LCO due to the presence of iron in its structure, instead of cobalt. The nature of the transition metal also renders LFP less expensive than LCO. Finally, LFP has a better thermal stability than LCO [26][27].

LFP presents two disadvantages, which are its low electronic conductivity and low diffusion of lithium ions. However, the low electronic conductivity (10^{-9}-10^{-11} S/cm) can be counterbalanced once again by adding a conducting additive during the electrode manufacturing process or by modifying the surface of the LFP powder particles, for example by coating them with carbon [26].

1.2.2 Slurry production

The active materials considered for this work were $Li_4Ti_5O_{12}$ (LTO) for the negative electrode and carbon-coated $LiFePO_4$ (LFP) for the positive electrode. LTO was provided by MTI (Batch number 0012003). Carbon-coated LFP was provided by Prayon (P800 Prayophos, Purelead Prayon).

The production of the composite electrodes is similar to what has been performed by Léonard *et al.* [21].

The aqueous slurry was produced by mixing 1.5 g of active material (LFP or LTO), 0.5 g of a conducting carbon/binder mix and 14.4 g of MilliQ water. The components can be seen in Figure 1.2. The masses chosen allowed to experimentally obtain 3 to 4 mg of active material on each current collector during the spray-coating process.

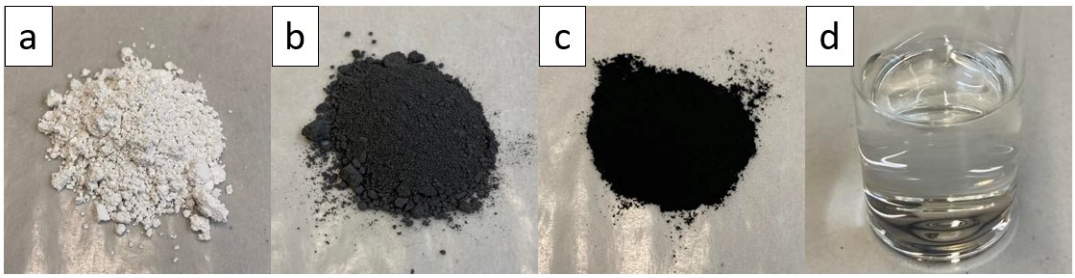

Figure 1.2: a) LTO powder, b) LFP powder, c) conducting carbon/binder mix, d) MilliQ water.

The conducting carbon/binder mix was produced by milling 0.4 g of xanthan gum binder (Sigma Aldrich, Figure 1.3a) and 1.6 g of Super C65 conducting carbon (Timcal, Figure 1.3b). The milling was performed with a plantetary mill Fritsch Monomill P6 (Figure 1.3c) in a stainless-steel jar with a volume of 80 mL and 20 stainless-steel 10 mm diameter balls (Figure 1.3d). The milling was done at 400 rpm during 1 min with 4 repetitions, in reverse mode. The obtained powder was then recovered.

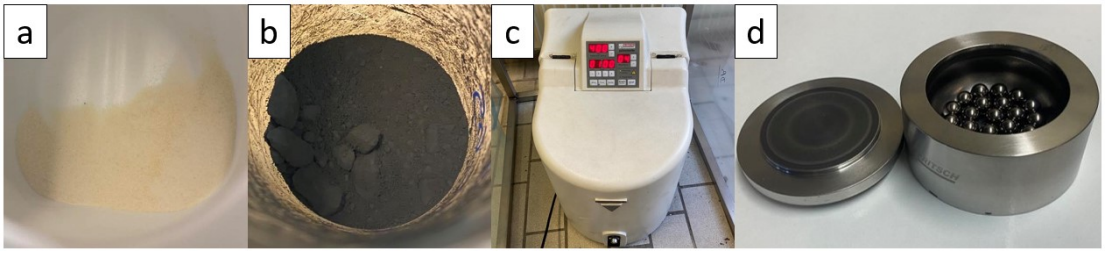

Figure 1.3: a) Xanthan gum, b) Timcal Super C65 conducting carbon, c) Fritsch Monomill P6, d) stainless-steel jar and balls.

Once the slurry was produced, it was stirred magnetically at 1000 rpm for 3 h. The two different slurries obtained can be seen in Figure 1.4.

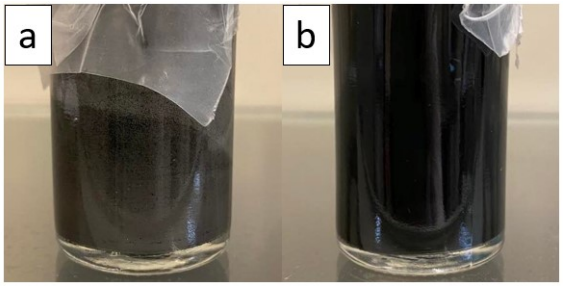

Figure 1.4: a) Final LTO slurry, b) final LFP slurry.

1.2.3 Spray-coating process

The aqueous slurries could then be spray-coated onto the current collectors using a robot spray.

The current collectors used to produce the electrodes were stainless-steel disks (15.5 mm diameter, 0.5 mm thickness, MTI corp.). The current collectors were thoroughly cleaned with acetone and ethanol and were weighed before the spray-coating process. Subtracting the initial weights from the final weights of the electrodes allows to determine the material amount of each electrode. This material amount can then be multiplied by 0.75 to obtain the active material amount, as the active material accounts for 75% of the total mass.

The set-up of the spray-coating process can be seen in Figure 1.5. The program used by the robot for this spray-coating process indicated to the robot that the slurry had to be sprayed in three different lines, spaced by 15 cm. The current collectors were therefore set up in three lines on the surface of the spray chamber. Usually, 15 to 24 electrodes were produced with one batch of slurry. Once the stainless-steel disks were placed, the experiment could be launched. The robot sprayed the slurry on the three lines and then waited 2 min before starting the next spraying cycle. This waiting time allowed the ink to dry and stick to the surface of the current collector. In addition, the surface onto which the current collectors were set was heated to 40°C to accelerate water evaporation.

Figure 1.5: Set-up for the spray-coating process.

To decide when the spray-coating process had to be stopped, the electrodes were weighed as the experiment went on to determine when the target amount of active material was

reached. This implies that the target amount of active material had to be chosen beforehand.

1.2.3.1 Choice of active material mass

The choice of the active material mass for the production of LFP and LTO electrodes had to be made while keeping in mind that one of the objectives of this work was to produce full LFP/LTO batteries. It was therefore of interest to target masses of active material which could be combined. To do so, a research on the capacity ratio between both electrodes within a full battery had to be made.

The capacity ratio is defined as the ratio between the capacity of the negative electrode (LTO) and of the positive electrode (LFP) [28]. The capacity of an electrode is defined by Equation 1.3 [29]:

$$C = n\frac{m}{MM}F \tag{1.3}$$

where

- C is the capacity of the electrode (Ah or Ah/cm^2).
- n is the number of lithium ions exchanged during the insertion/deinsertion reaction of the active material considered (-). n corresponds to 1 and 3 lithium ions for LFP and LTO respectively.
- m is the mass of active material (g or g/cm^2).
- MM is the molar mass of active material (g/mol). MM corresponds to 157.8 g/mol and 459.1 g/mol for LFP and LTO respectively.
- F is the Faraday constant, 96 485 C/mol or 26.8 Ah/mol.

The capacity ratio can therefore be described by Equation 1.4.

$$\text{Ratio} = \frac{C_{LTO}}{C_{LFP}} = \frac{m_{LTO}}{m_{LFP}}\frac{MM_{LFP}}{MM_{LTO}}\frac{n_{LTO}}{n_{LFP}} \tag{1.4}$$

The capacity ratio applied in lithium-ion batteries is usually bigger than 1, leading to an excess of the negative electrode capacity in comparison to the positive electrode capacity. An excess of negative electrode capacity is desired to avoid lithium plating at the negative electrode [30]. This plating leads to the formation of dendrites which can either detach from the negative electrode, leading to dead lithium and to a decrease in the capacity, or can reach the positive electrode and induce internal short-circuits. LTO negative electrodes are less prone to lithium plating than classical graphite negative electrodes due to the fact that they operate at higher voltages, further away from that of lithium metal. However, an excess capacity is still applied for batteries using LTO as negative electrode [23][30].

In this work, it was decided to determine the capacity ratio based on the article written by Castaing *et al.* [31]. The described capacities in the article are respectively 1 mAh/cm^2 and 1.3 mAh/cm^2 for the LFP and LTO electrodes, leading to a capacity ratio of 1.3. This ratio was used with Equation 1.4 to determine the target masses of active material.

As an example, if it is decided to produce LTO electrodes with an active material mass of 3.8 mg, Equation 1.4 can be applied with a ratio of 1.3 and gives an active material mass of LFP of 3.0 mg. Keeping in mind that the active material corresponds to 75% of the total mass sprayed on the current collector, 5.0 mg and 4.0 mg have to be sprayed onto the current collectors for LTO and LFP electrodes respectively.

1.2.4 Drying process

Once the target masses were reached during the spray-coating process, the experiment could be stopped and the electrodes could be retrieved. The LTO and LFP electrodes manufactured can be observed in Figure 1.6. The electrodes were dried overnight at 60°C under air and at atmospheric pressure. They were then weighed and the amount of active material was determined based on the fact that it corresponds to 75% of the mass sprayed on the current collector. The electrodes were then put back in the oven at 110°C and at 20 mbar for 2 h. Afterwards, the electrodes were then stored under argon atmosphere in a glovebox.

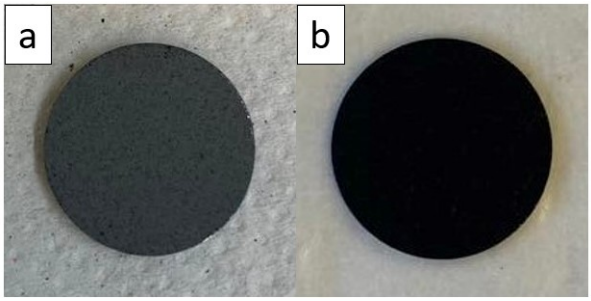

Figure 1.6: a) LTO electrode, b) LFP electrode.

It must be noted that no calendering was performed on the electrodes in this work. Calendering is considered to be an optimisation step which is performed mostly at the industrial scale to reduce the thickness and increase the density of the electrodes. Indeed, the objective at the industrial scale is to obtain high energy densities, both in terms of mass (gravimetric energy density) and volume (volumetric energy density). Calendering therefore allows to improve the volumetric energy density by decreasing the volume of the electrodes [18]. The concepts studied in this work are mainly at the research stage and optimisation was therefore not the main issue considered.

1.2.5 Surface characterisation

The surface of the electrodes was studied through contact profilometry. Contact profilometry allows to measure quantitatively the electrode surface roughness and therefore to

determine the thickness of the electrode material [32]. The profilometer is composed of a stylus with a sharp tip, which acts as a probe. This probe is moved on the surface of the sample along a specific direction. By entering in contact with the rough surface of the sample, the probe moves in the vertical direction to adjust to the surface. This vertical movement is recorded and allows to obtain information concerning the surface roughness [33].

Electrodes of both types were prepared for the profilometry measurement by removing part of the coated material. The material was removed with a toothpick in four different lines, as can be seen in Figure 1.7. The zones with no material were considered to be at a height of 0 μm and were used to determine the height of the coating.

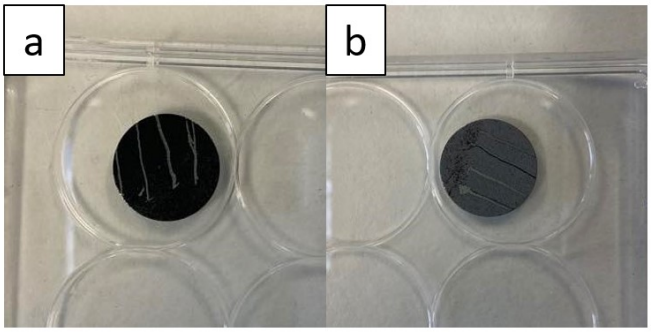

Figure 1.7: Electrodes studied by profilometry: a) LFP, b) LTO.

The profilometer used to perform the measurements was a Bruker Dektak XT profilometer. The electrode was placed on the plate of the profilometer, perpendicularly to the probe movement, as can be seen in Figure 1.8.

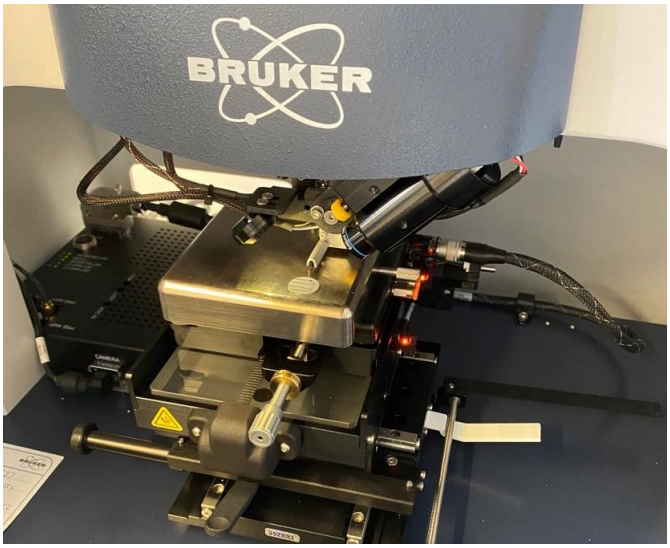

Figure 1.8: Bruker Dektak XT profilometer used for the experiments.

The scan duration was set to 60 s and the scan length was set to 18 000 μm. Both of these

parameters impact the speed at which the probe performs the measurement. The scan range was set to 65.5 μm. This scan range corresponds to the vertical range covered by the probe during the measurement. The maximum expected height of the sample should therefore be within this scan range. Four measurements were performed for each electrode at four different positions.

Once the thickness was obtained through profilometry, it could be used to determine the void fraction of the electrode. To do so, it had first to be kept in mind that the electrodes studied were composite electrodes, schematically represented in Figure 1.1.

The void fraction of the electrode can be determined by comparing the total volume of the composite electrode and the volume of the material, which does not take into account the void fraction between the particles.

The total volume V_{tot} of the electrode is defined by Equation 1.5:

$$V_{tot} = \pi r^2 e \tag{1.5}$$

where

- r is the radius of the electrode which corresponds to the radius of the current collector, 7.75 mm or 7 750 μm.
- e is the thickness of the electrode material, determined through contact profilometry (μm).

The volume of the solid V_{solid} is defined by Equation 1.6:

$$V_{solid} = \frac{m}{\rho_{solid}} \tag{1.6}$$

where

- m is the mass of material on the current collector (mg).
- ρ_{solid} is the density of the material. The material was composed of 75% of active material, 20% of conducting carbon and 5% of xanthan gum binder. The density of the different components are the following: 3.6 g/cm^3 for LFP [34], 3.5 g/cm^3 for LTO [35], 1.6 g/cm^3 for conducting carbon [36] and 1.5 g/cm^3 for xanthan gum [37]. This allowed to determine the density of the two electrode materials: $\rho_{solidLTO}$ = 3.0 g/cm^3 and $\rho_{solidLFP}$ = 3.1 g/cm^3.

The void fraction ϕ is then defined by Equation 1.7:

$$\phi = \frac{V_{tot} - V_{solid}}{V_{tot}} \tag{1.7}$$

Having an estimation of the void fraction allows to know how much electrolyte can permeate the electrode material.

1.3 Results and discussion

1.3.1 Active material masses obtained during spray-coating

The spray-coating process was performed regularly to produce LTO and LFP electrodes during the Master thesis. For each batch of electrodes produced via spray-coating, the active material masses were determined. Ideally, the electrodes produced during the same spray-coating process should have identical active material masses. It is therefore of interest to observe the active material masses obtained for one batch of electrodes to see if the obtained masses are similar or if variations occurred during the process.

The active material masses obtained for one batch of 15 LTO electrodes can be observed in Table 1.1. The average active material mass and the standard deviation have been calculated and are also available in Table 1.1. An example for a batch of 15 LFP electrodes is available in the Appendices.

Table 1.1: Active material masses, average active material mass and standard deviation of a batch of 15 LTO electrodes produced *via* spray-coating.

LTO electrode n°	LTO active material mass (mg)
1	4.4
2	4.1
3	4.1
4	3.8
5	3.9
6	4.1
7	3.9
8	3.9
9	3.7
10	3.6
11	3.7
12	3.5
13	3.5
14	3.5
15	3.5
Average active material mass (mg)	3.8
Standard deviation (mg)	0.3

The standard deviation was calculated with Equation 1.8 [38]:

$$\sigma = \sqrt{\frac{\sum(m_i - \overline{m})^2}{N}} \tag{1.8}$$

where

- σ is the standard deviation (mg).
- m_i is the active material mass of LTO (mg), with i corresponding to the successive electrode numbers.
- $\overline{m}$ is the average active material mass (mg), corresponding in this case to 3.8 mg.
- N is the number of electrodes produced in the considered batch (-). It corresponds to 15 in this case.

From Table 1.1, it can be observed that the active material masses are not identical for all the electrodes. This is also the case for the LFP batch available in the Appendices. Keeping in mind that the electrodes were separated into three rows during the process, three different average masses can be obtained for the batch of Table 1.1: 4.1 mg for the row 1-5, 3.8 mg for the row 6-10 and 3.5 mg for the row 11-15. This variation among the masses obtained by the spray-coating process can probably be explained by the three following reasons:

- During the spray-coating process, the robot sprayed in three different lines spaced by 15 cm. It might be possible that the robot slightly shifted its position from the initially defined lines during the process. This led to a misalignment of the electrodes with the trajectory of the spray during some spraying sequences of the process, and ultimately led to variations among the masses obtained.
- The electrodes might have been misaligned with the trajectory of the spray from the start of the process. Indeed, it was complicated to align perfectly the electrodes with the nozzle of the spray and the positioning of the electrodes was left to the appreciation of the operator. This led to inevitable variations among the three rows.
- Finally, the slurries used in the spray-coating process, especially the LFP slurry, slowly clogged the nozzle of the spray-robot as the process went on. The start of the clogging was difficult to detect during the process and the spraying became slowly less homogeneous than in the beginning. Even if the nozzle was unclogged regularly during the process, it was impossible to obtain a completely homogeneous spraying during the whole process.

The inhomogeneity of masses obtained for a same batch of electrodes is a disadvantage from an industrial point view, where reproducibility is crucial. At the research stage, reproducibility is still sought. However, it can be seen in Table 1.1 that a standard deviation of 0.3 mg from the average is obtained. This means that the masses obtained vary of about +8% and -8% around the average. This deviation is manageable at the research stage, were the different LTO and LFP electrodes manufactured can be associated manually to obtain batteries with a capacity ratio as close as possible to the targeted one.

1.3.2 Contact profilometry results

The contact profilometry results of the first measurements for the LTO and LFP electrodes can be seen respectively in Figures 1.9 and 1.10. The results of the three other measurements are available in the Appendices. The graphs were obtained by treating the raw data such that the zones with no material correspond to 0 μm. The LTO electrode studied had a total mass loading of 3.5 mg while the LFP electrode had a total mass loading of 3.8 mg.

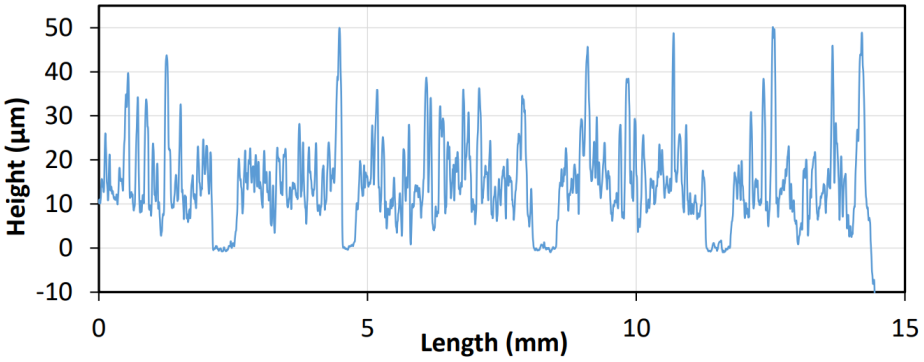

Figure 1.9: Profilometry results for the LTO electrode, first measurement.

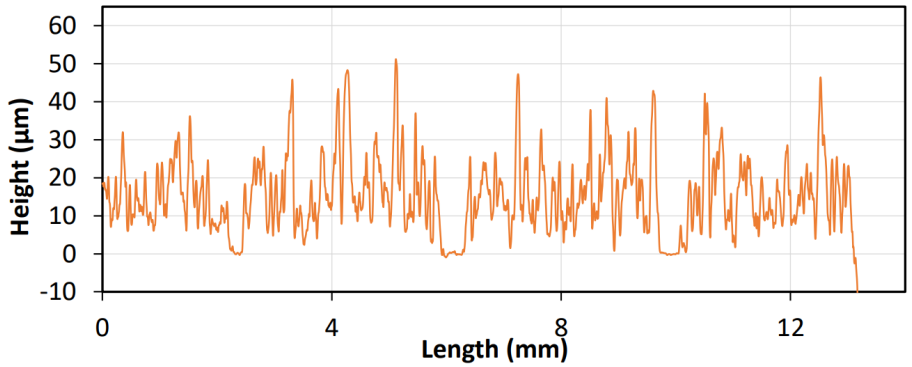

Figure 1.10: Profilometry results for the LFP electrode, first measurement.

By observing the graphs, it can be seen that the surface heights of both electrodes are similar which is expected due to the similar mass loadings of the electrodes, densities of the materials and the identical coating method. It can also be concluded that the surface of the electrodes is quite rough and the thickness is variable. This variability can probably be associated to the spray-coating process performed with the robot. This process could not be controlled totally, and it was seen through the masses obtained in Section 1.3.1 that the way the robot sprayed the ink was not always homogenous. A flatter surface of electrode could have been obtained after the spray-coating process if calendering had been applied. Calendering would have also decreased the overall void fraction of the electrode material.

The mean thickness of the electrode material can be calculated for both types of electrodes from the four different measurements realised. Both types of electrodes have a mean thickness of 17 μm.

The void fractions of the electrodes can be calculated using Equations 1.5 to 1.7. Taking into account that the precision of the analytical scale is of 0.1 mg, that the results of profilometry showed a highly variable surface, that a mean surface height of 17 μm was obtained for both electrodes and that the theoretical densities of the materials are different of 0.1 g/cm^3, it can be expected that the void fractions of both electrodes will be highly similar. The calculation of void fraction is therefore performed for only one of the electrodes, LFP, and will be representative for both LFP and LTO electrodes. It must kept in mind that the void fraction can only be calculated with a limited precision and the results will give an order of magnitude of the void fraction.

The results for the LFP electrode are summarised in Table 1.2.

Table 1.2: Results of the void fraction calculations for the LFP sample.

Total mass (mg)	V_{tot} (cm^3)	V_{solid} (cm^3)	ϕ (-)
3.8	0.0032	0.0012	0.62

It can be concluded that the composite electrodes are highly porous, with void fractions of about 60%. This means that the electrolyte will be able to enter the electrode and not only stay at its surface. The high void fraction leads to a high surface area of contact between the electrolyte and the material. This will enhance the conduction of lithium ions from and towards the electrolyte. However, this high void fraction is detrimental when the volumetric energy density is considered.

1.4 Conclusion and perspectives

Composite electrodes of LFP and LTO have been produced *via* spray-coating, using the water-based process developed at the NCE laboratory. This process allows to avoid the use of toxic solvents and PVDF, which is hard to eliminate upon recycling, and therefore takes a step towards more sustainable electrode manufacturing.

The active material masses obtained during the spray-coating process were analysed. It was shown that inhomogeneities occurred within one batch of electrodes. Indeed, the spray-coating process could not be controlled perfectly, especially the alignment between the electrodes and the trajectory of the spray. The variations in the masses obtained are a disadvantage from the industrial point of view. However, from the research point of view considered in this work, the variations are manageable.

The surface of the electrodes were characterised through contact profilometry. The profilometry results showed a rough surface and the mean thickness of the coating allowed

to determine a void fraction of about 60%. This high void fraction is beneficial in terms of electrolyte infiltration in the electrode material but is detrimental when the volumetric energy density is considered. For the classical liquid electrolyte, the void fraction allows to know the degree to which the electrolyte will be in contact with the material during the operation of the battery. For semi-solid electrolytes such as the gel polymer electrolyte, knowing the void fraction is interesting for operation just as for liquid electrolytes but also for processing. Having an estimation of the void fraction of the electrode material allows to know how much gel polymer electrolyte can be casted to fill this void fraction. This information is interesting if an alternate spraying of electrode material and casting of gel polymer electrolyte is performed. Indeed, knowing the void fraction will allow to add the right amount of gel polymer electrolyte between the different spraying sequences of electrode material to fill the void fraction without forming an insulating layer of electrolyte between two layers of electrode material.

The electrodes manufactured were destined to be used in half-cell and full-cell configurations to study their electrochemical performances in combination with the different electrolytes investigated. Before studying half-cell and full-cell configurations, the different electrolytes had to be analysed individually. The next chapter focuses on the study of the electrochemical stability of the three electrolytes investigated in this work.

CHAPTER 2

Electrolyte study

2.1 Introduction

The electrolyte is an essential component of lithium-ion batteries, without which battery operation would not be possible. Its major role is to conduct lithium ions between the two working electrodes. The electrolyte is usually present in the liquid form and is composed of a salt dissolved in one or more solvents, which are either aprotic or aqueous. Other forms of electrolyte are also investigated. A few examples are polymer electrolytes, which have a solid or gel structure, and ionic liquid-based electrolytes, composed of lithium salts dissolved in ionic liquids [39][40].

To be suitable for battery operation, the electrolyte should have specific properties. It should have a good ionic conductivity, to allow an easy ion transport between the electrodes. It should also be electronically insulating, to prevent electrons from passing directly from one electrode to the other and inducing a short-circuit, which could lead to high self-discharge and thermal runaway. The electrolyte should be stable over a wide electrochemical window to avoid its degradation upon operation within the range of potentials of the studied electrodes. It should also be stable when put in contact with electrodes, separators, current collectors and any other component of the battery. In addition, the thermal stability of the electrolyte is very important to ensure a safe operation. The electrolyte should also be environmentally friendly and ideally low-cost [39][40][42].

It must be kept in mind that the perfect electrolyte does not exist and that a trade-off between the different properties is always necessary. This means that any electrolyte will have advantages as well as disadvantages.

This chapter presents the three different electrolytes investigated in this work as well as the measurement of their electrochemical stability. The first electrolyte studied was the classical liquid electrolyte, 1 M $LiPF_6$ in (1:1 vol.%) EC:DEC. This electrolyte is one of the most used commercially for its desirable properties in terms of ionic conductivity. However, some disadvantages can be associated to this electrolyte in terms of safety and environmental concerns [11]. The second electrolyte investigated was a gel polymer electrolyte, which is a semi-solid electrolyte with the main advantage of preventing leaks from the battery. However, this electrolyte might have lower performances in terms of ionic conductivity [14]. The third and final type of electrolyte investigated was the water-in-salt

electrolyte, consisting in a lithium salt dissolved in water. This electrolyte is therefore an aqueous electrolyte and allows to avoid the use of carbonates. However, some challenges are associated to the use of that electrolyte [16].

2.2 1 M $LiPF_6$ in (1:1 vol.%) EC:DEC

2.2.1 Introduction

The electrolyte based on the $LiPF_6$ salt dissolved in a mix of carbonates is the most commercially used electrolyte in lithium-ion batteries. It represents the class of classical liquid electrolytes, which are composed of two or more aprotic solvents in which a lithium salt is dissolved [39].

The solvent must have specific properties to be used in lithium-ion batteries. The first important property is that the solvent should have a high dielectric constant, meaning that it should dissolve the lithium salt of interest up to a required concentration [39][40]. Indeed, the dielectric constant can be defined as a measurement of the ability of a solvent to dissociate a component into its ions. A high dielectric constant is therefore desirable so that the lithium salt is completely dissociated into its ions in the electrolyte solvent [41]. In addition, the viscosity of the solvent should be low to promote the mobility of lithium ions in the electrolyte. It should also wet the electrodes and separator sufficiently to have good contacts between the electrolyte and the battery elements. The solvent should also stay in liquid state in a wide temperature range, to keep a constant ionic mobility. It should be inert when put in contact with the different elements of the battery, such as the positive and negative electrode materials. Finally, it should be safe, have a low toxicity and be low-cost [39][40].

The most used type of solvents in lithium-ion battery electrolytes are cyclic and linear alkyl carbonates, for which the chemical structures are represented in Figure 2.1 [39][43].

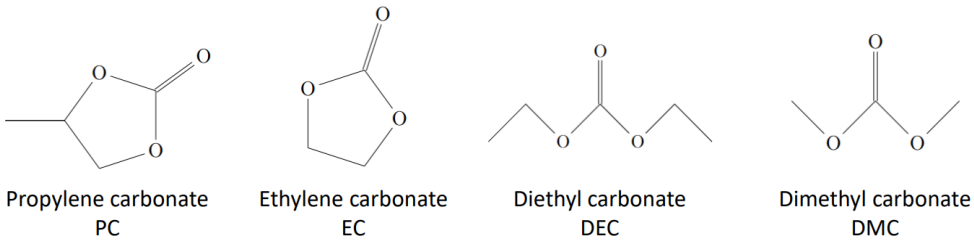

Figure 2.1: Chemical structure of cylic and linear alkyl carbonates.

Two ore more types of carbonates are always used to dissolve the lithium salt. This can be explained by the fact that a combination of carbonates allows to combine the properties of those carbonates to optimise the solvent mix. For example, propylene carbonate (PC) or ethylene carbonate (EC) can usually be used in combination with diethyl carbonate (DEC) or dimethyl carbonate (DMC). On the one hand, PC and EC are cyclic carbonates with

high dielectric constants due to their high polarities but are very viscous and thus have low ionic conductivities. On the other hand, DEC and DMC are linear carbonates which have low dielectric constants and low viscosities. Using an appropriate mix of cyclic and linear carbonates as solvent allows to combine the high dieletric constant of cyclic carbonates with the low viscosity of linear carbonates [39][43].

However, carbonates have the main disadvantage of being highly flammable, leading to important safety issues. Indeed, the linear carbonates present in the solvent mix have a high volatility and flammability as well as low flash points [12].

Just as for the solvent, the lithium salt should ideally have specific properties. It should first completely dissolve in the selected solvent and the resulting ions, more precisely the cations, should be highly mobile in the solvent. Then, it should be highly stable thermally and chemically. The anion of the salt should remain inert to the solvents, it should be non-toxic and remain stable when thermally induced reactions with the solvents or other battery components occur. The anion should also withstand the operating conditions of the battery and remain stable when oxidative decomposition occurs at the positive electrode. Both the anion and cation should remain stable when put in contact with any of the battery components (separator, current collector, *etc.*). To continue, the salt should be able to passivate current collectors made of aluminium to prevent the dissolution or desorption of aluminium. Finally, it should also form solid-electrolyte interphases on the electrodes which are less resistive to the movement of lithium ions [11][39].

The classical liquid electrolyte tested in this work was 1 M $LiPF_6$ in (1:1 vol.%) EC:DEC. $LiPF_6$ is the most commercially used lithium salt in lithium-ion battery electrolytes due to its well-balanced combination of properties. It is not the best salt when looking at a specific property but some properties are in conflict and $LiPF_6$ is the salt with the best compromise [11][39].

The use of $LiPF_6$ is advantageous for several reasons. First, $LiPF_6$ is one of the most conducting lithium salts, with a conductivity of 10.7 mS/cm when dissolved in EC/DMC (1:1). This remarkable conductivity can be explained by the combination of its dissociation constant and its ionic mobility. $LiPF_6$ is not the best available lithium salt for both of those properties but it is the one which combines them the best, as can be seen by the ranking of different lithium salts [11][39]:

- Dissociation constant: LiTf $<$ $LiBF_4$ $<$ $LiClO_4$ $<$ $\mathbf{LiPF_6}$ $<$ $LiAsF_6$ $<$ LiTFSI
- Average ion mobility: $LiBF_4$ $>$ $LiClO_4$ $>$ $\mathbf{LiPF_6}$ $>$ $LiAsF_6$ $>$ LiTf $>$ LiTFSI

Second, $LiPF_6$ mixed in carbonates is highly stable from the electrochemical point view. Indeed, a solution of 1 M $LiPF_6$ in (1:1 vol.%) EC:DMC can withstand oxidation up to 5.1 V *vs.* Li^+/Li and a solution of 1 M $LiPF_6$ in (1:1 vol.%) EC:DEC can withstand oxidation up to 4.8 V *vs.* Li^+/Li [44][39].

Finally, $LiPF_6$ passivates aluminium current collectors and prevents dissolution or desorption of aluminium [11][39].

Despite the advantages of $LiPF_6$, its two main disadvantages cannot be ignored. First,

$LiPF_6$ has a poor thermal stability. At elevated temperatures and in presence of water, even at very low concentrations (ppm level), the reaction depicted in Equation 2.1 is favoured.

$$LiPF_6 + H_2O_{(\text{moisture in electrolyte})} \rightleftharpoons LiF + PF_5 \tag{2.1}$$

The gaseous product generated by the reaction, PF_5, is a strong Lewis acid and can initiate undesirable reactions when in presence of carbonates, such as ring openings and cleavages of ether links [11][39].

The second main disadvantage of $LiPF_6$ is linked again to the presence of moisture in the solvents. The P-F bond present in the salt is very sensitive to moisture and can be hydrolysed even at room temperature. This leads to the formation of HF through the reaction depicted in Equation 2.2 [11][39].

$$LiPF_6 + H_2O_{(\text{moisture in electrolyte})} \rightarrow POF_3 + LiF + 2HF \tag{2.2}$$

In addition, related to the first disadvantage, PF_5 can be hydrolised as well at high temperatures and lead to the formation of HF through the reaction depicted in Equation 2.3 [11][39].

$$PF_5 + H_2O \rightarrow POF_3 + 2HF \tag{2.3}$$

The by-products of those two reactions are corrosive and dangerous, and thus lead to safety issues concerning the use of this electrolyte [11][39].

The disadvantages restrict the use of the 1 M $LiPF_6$ in (1:1 vol.%) EC:DEC electrolyte in terms of operation temperature and water content. However, its advantages make it an interesting electrolyte for applications in lithium-ion batteries and $LiPF_6$ in carbonates is still the leader electrolyte at commercial level [39].

2.2.2 Experimental

2.2.2.1 Cell assembly

To investigate the electrochemical stability of the electrolyte and the performances of the electrodes, coin cell configurations were studied. When non-aqueous electrolytes were used, the assembly of coin cells was performed in an argon-filled glovebox, shown in Figure 2.2a. Coin cell batteries in half-cell configuration were assembled as shown in Figure 2.2b.

When the target was to study the stability of the electrolyte, the positive and negative electrodes were not present in the coin cell. The electrodes were blocking electrodes corresponding to stainless-steel spacers, which are electrochemically inert and allow to study the behaviour of the electrolyte alone. In addition, 2 Celgard separators were added to separate both spacers. Those separators were soaked in 80 μL of 1 M $LiPF_6$ in (1:1 vol.%) EC:DEC electrolyte, which was purchased from Solvionic.

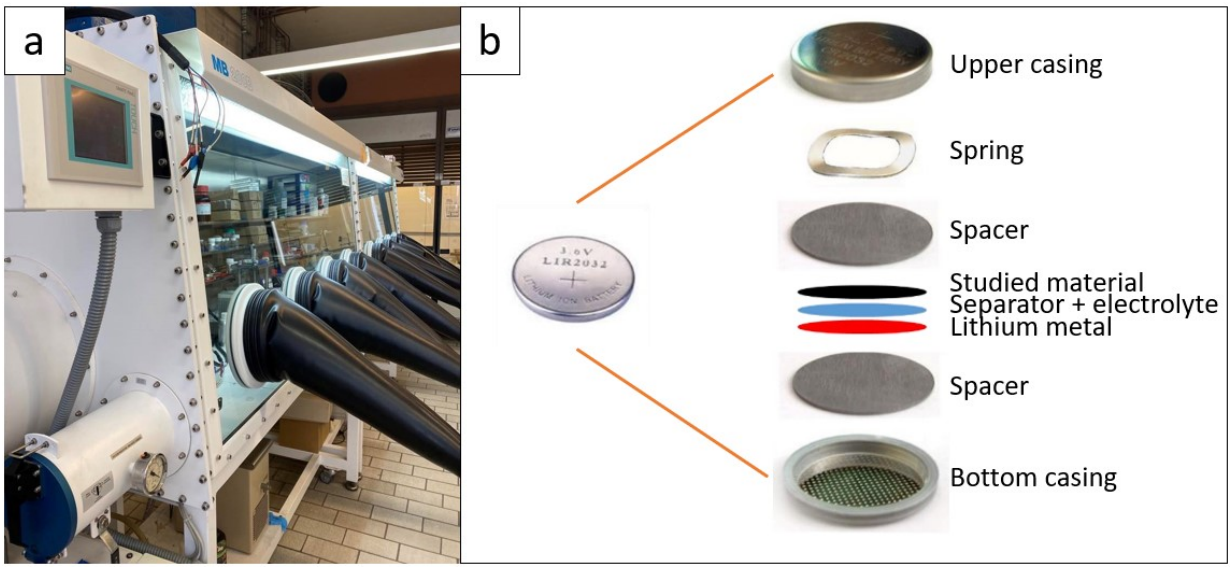

Figure 2.2: a) Glovebox used to assemble the cells, b) general structure of the assembled coin cells in half-cell configuration, modified from [29].

2.2.2.2 Cyclic voltammetry characteristics

Cyclic voltammetry was applied to the assembled coin cells and allowed to observe the decomposition of the electrolyte. Based on the available equipment at the laboratory, cyclic voltammetry could not be applied against a reference electrode because three-electrode systems were not available. Cyclic voltammetry was therefore performed with a two-electrode system, corresponding to the coin cell configuration. The results obtained show the width of the electrochemical stability window but not its position in comparison to a reference, for example Li^+/Li. However, the measurements already give an idea about the stability of the studied electrolyte and allow to compare the different electrolytes.

Cyclic voltammetry was performed with the Biologic VMP3 multichannel potentiostat. Different cyclic voltammetry regimes were applied: between 0 and 1.5 V, 0 and 2 V, 0 and 2.5 V, 0 and 3 V, 0 and 3.5 V, 0 and 4 V. The scan rate was set to 5 mV/s and 5 cycles were performed for each voltage range.

2.2.3 Results and discussion

2.2.3.1 Cyclic voltammetry

The cyclic voltammetry results for the classical liquid electrolyte 1 M $LiPF_6$ in (1:1 vol.%) EC:DEC can be observed in Figure 2.3. Each curve represents the results for the 5^{th} cycle of each voltage range tested.

It can be seen from Figure 2.3 that the currents reached during cyclic voltammetry increase with the voltage range applied, meaning that the electrolyte is less stable when higher voltage windows are tested. However, the intensities of the currents are very low in comparison

to classical currents applied during galvanostatic charge and discharge of batteries. Indeed, for the masses considered in this work, the classical currents applied corresponding to a C-rate of C were around 0.6 mA for the half-cells and 0.3 mA for the full-cells. The C-rate is a measurement associated to the current at which a cell can be charged and discharged completely during a specific time. As an example, a C-rate of C corresponds to a complete charge at a specific current during 1 h and a complete discharge at the same specific current during 1 h. If a C-rate of C/5 is considered, the complete charge and discharge of the battery at a specific current will take respectively 5 h [45]. By comparing the classical currents applied to the intensities of the currents in Figure 2.3, it can be concluded that the currents generated by the reaction of the electrolyte are negligible and the electrolyte is therefore stable over a wide electrochemical window, corresponding to at least 4 V. In addition, it is known from the literature that the electrolyte 1 M $LiPF_6$ in (1:1 vol.%) EC:DEC can withstand oxidation until 4.8 V *vs.* Li^+/Li [44]. This allows to conclude that the electrolyte is suitable for the application in full LFP/LTO batteries targeted in this work, for which the voltage is expected to be around 1.85 V [46].

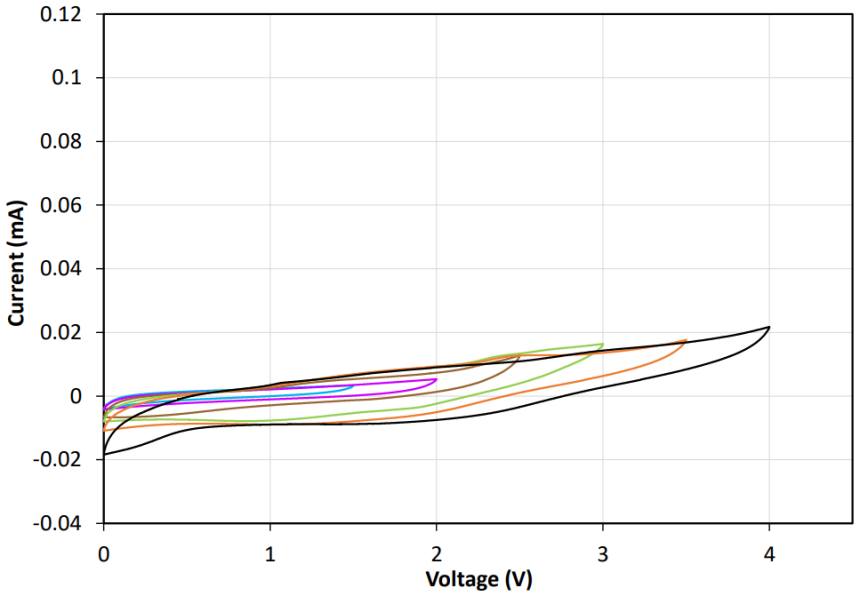

Figure 2.3: Cyclic voltammetry results: 1 M $LiPF_6$ in (1:1 vol.%) EC:DEC, coin cell system: 5^{th} cycle, scan rate of 5 mV/s, voltage ranges: 0-1.5 V (blue), 0-2 V (violet), 0-2.5 V (brown), 0-3 V (green), 0-3.5 V (orange), 0-4 V (black).

2.2.4 Conclusion

This section studied the classical liquid electrolyte 1 M $LiPF_6$ in (1:1 vol.%) EC:DEC. This electrolyte has a high ionic conductivity and a wide electrochemical stability window. This makes it attractive for applications in lithium-ion batteries and it is indeed the most commercially used type of electrolyte. However, this electrolyte presents major disadvantages in terms of safety and environmental issues.

The stability results obtained showed that the electrolyte is stable over at least 4 V. Those

results are used as a basis for comparison with the stability of the two less conventional electrolytes tested in this work, which aim to go towards safer and environmentally friendlier electrolytes.

2.3 Gel polymer electrolyte

2.3.1 Introduction

To overcome the disadvantages and safety issues of liquid electrolytes, increasing attention has been given to polymer electrolytes. A polymer electrolyte is a solid membrane which consists in a high molecular weight polymer matrix in which a lithium salt is dissolved. Polymer electrolytes are good candidates to replace liquid electrolytes because they prevent electrolyte leakage and internal short-circuits, they present a wide electrochemical window and they are thermally stable. In addition, due to the solid-state of the polymer electrolyte, it can play the role of separator between the positive and negative electrodes and thus suppress the need of a supplementary porous separator within the battery. The ionic conductivity is one of the most important properties characterising the performances of an electrolyte and can be an issue when polymer electrolytes are considered. The ionic conductivity of a polymer electrolyte is closely linked to its degree of crystallinity and its viscosity. A higher degree of crystallinity leads to a lower ionic conductivity because the ions have less mobility in a crystalline phase than in an amorphous phase. A higher viscosity of the polymer electrolyte will lead to the formation of less voids within the electrolyte and the ionic conductivity will be decreased [14][47][48].

Two main types of polymer electrolytes are usually considered: the solid polymer electrolyte and the gel polymer electrolyte [14].

Solid polymer electrolytes consist in a lithium salt directly dissolved within the polymer matrix, without the use of any liquid solvents. These electrolytes are widely studied and appear to be good candidates for solid-state batteries. However, this type of electrolyte presents the major disadvantage of having a low ionic conductivity (10^{-8}-10^{-5} S/cm) compared to classical liquid electrolytes (10^{-3} S/cm) due to its high degree of crystallinity. In addition, it has bad contacts with the electrodes, which does not facilitate the mobility of ions. The applications of solid polymer electrolytes in energy storage are therefore currently limited [14][48].

Gel polymer electrolytes (GPEs) consist in a polymer matrix with a liquid electrolyte trapped within it. This type of electrolyte has been increasingly studied because it combines the high ionic conductivity of the liquid electrolyte with the mechanical stability of the solid polymer. Most GPEs have an ionic conductivity extremely close to that of liquid electrolytes, making them very attractive for energy storage applications [14].

The type of GPE studied in this work was an heterogeneous GPE consisting of two different phases: the gel polymer matrix and the liquid electrolyte trapped in its void fraction [14]. The liquid electrolyte plays the role of the plasticizer, increases the ionic conductivity and solvates the lithium salt, meaning that the polymer matrix does not require this solvation

property [49].

The polymer matrix can be composed of one or more monomer types. Different types of polymers have been investigated such as poly(ethylene oxide) (PEO), poly(vinyl chloride) (PVC), poly(vinylidene fluoride) (PVdF), poly(vinylidene fluoride-co-hexafluoropropylene) (PVdF-HFP), poly(acrylic acid) (PAA) and even more. PEO is one of the most popular polymers due to its numerous advantages such as its good dimensional stability, chemical stability, flexibility, *etc.* However, its main disadvantage is that it has a low ionic conductivity at ambient temperature due to the majority of crystalline phase present at that temperature. An alternative to PEO, which has been considered in this work, is a copolymer of PVdF-HFP. This copolymer combines the crystalline phase of PVdF with the amorphous phase of PHFP (poly(hexafluoropropylene)). The amorphous phase of this polymer can trap a large quantity of liquid electrolyte, which is beneficial in terms of ionic conductivity. This leads to a polymer with a high ionic conductivity due to the amorphous phase and a good mechanical strength due to the crystalline phase. This combination of properties is attractive for the use of this polymer in lithium-ion batteries [47][49].

The liquid electrolyte trapped within the polymer matrix is composed of a solvent and a lithium salt, which can be of various natures. The classical liquid organic electrolyte can be used in GPEs. However, safety issues are still associated to this liquid electrolyte even if its risks of leakage are reduced. Another more recent liquid electrolyte which can be used in GPEs and which has been considered in this work is an ionic liquid electrolyte. An ionic liquid is a molten salt at room temperature which presents many advantages such as low volatility, low toxicity, non-flammability, large electrochemical stability window, high thermal and chemical stability. The ionic liquids used as electrolyte can reach high ionic conductivities of the order of that of classical liquid electrolytes when the lithium salts dissolved in it are compatible with the ionic liquid considered. A lithium salt is said to be compatible with an ionic liquid when both of them have the same anion. As an example, the ionic liquid electrolyte considered for the preparation of the GPE in this work was made of the lithium salt LiTFSI (lithium bis(trifluoromethanesulfonyl)imide) and the ionic liquid $PYR_{13}FSI$ (N-Propyl-N-methylpyrrolidiniumbis(fluorosulfonyl)imide), which have similar anions. The main disadvantage of ionic liquid electrolytes is their high cost, which restricts commercial applications [47][50].

Additives can be introduced in the polymer matrix of GPEs to enhance their properties. Such additives are for example inorganic fillers and clay, which lead to enhanced conductivity but also to a better mechanical strength of GPEs. Inorganic fillers play the role of plasticizers and increase the conductivity of the polymer matrix by decreasing the crystallinity of this matrix. Inorganic clay, usually of smectite type, is a good additive to reinforce the polymer matrix. In addition, it also allows to increase the ionic conductivity of the matrix, prevent the growth of lithium dendrites when lithium metal is used as negative electrode of lithium-ion batteries and increase the thermal stability of the electrolyte [51]. The use of a clay such as montmorillonite allows to increase the ionic conductivity of GPEs due to its ability to intercalate the polymer chains and thus decrease the crystallinity of the polymer. The structure of montmorillonite can be observed in Figure 2.4. In addition, if montmorillonite is lithiated through cationic exchange between Na^+ and Li^+, the

lithium ions present between its layers can participate to the ionic conductivity. Finally, this clay is a low-cost material [49][52].

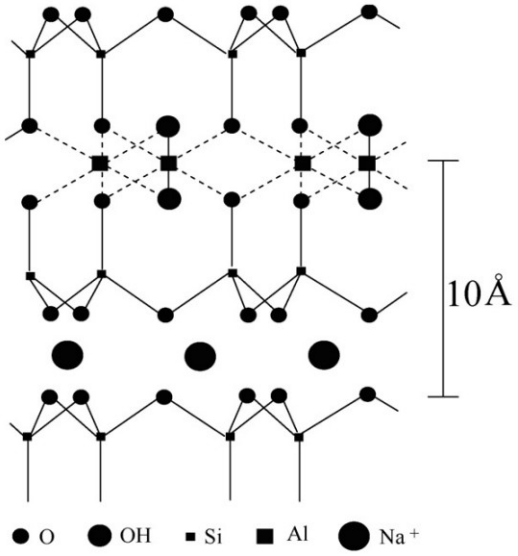

Figure 2.4: Representation of montmorillonite clay, belonging to the smectite group [53].

2.3.2 Experimental

2.3.2.1 Synthesis of the electrolyte

The GPE investigated in this work was composed of poly(vinylidene fluoride-co-hexafluoropropylene) (PVdF-HFP) as the polymer matrix, a binary liquid solution composed of N-Propyl-N-methylpyrrolidiniumbis(fluorosulfonyl)imide ($PYR_{13}FSI$) and lithium bis(trifluoromethanesulfonyl)imide (LiTFSI) and a modified clay acting as reinforcing filler. Acetone was added to dissolve PVDF-HFP and allow the solution to potentially be sprayed without clogging issues by decreasing its viscosity.

The starting formulation used in this work was developed at the NCE laboratory and had the following properties: a mass of lithiated clay equal to 70 wt% of PVdF-HFP, a mass of PVdF-HFP equal to 30 wt% of $PYR_{13}FSI$ and a concentration of LiTFSI in $PYR_{13}FSI$ equal to 3 M.

For the first tests performed, the following masses and volumes of components were used: 1.2 g of PVdF-HFP (Solvay Specialty Polymers France, SOLEF 21216/1001, Batch C.3074/11.F.2), 0.84 g of lithiated montmorillionite clay (Cloisite-Na+ Polymer additive BYK Batch No. 0001969652 lithiated with $LiNO_3$), 2.58 g of LiTFSI (99.9%, Solvionic, S001A250, L19112501), 3 mL of $PYR_{13}FSI$ (99.9%, Solvionic, L19030101), 90 mL of acetone (AnalR NORMAPUR, VWR Chemicals, 20066.330, Batch 17L124016).

A batch of lithiated clay was already available at the laboratory. However, if lithiated clay must be produced, the following procedure must be followed. The sodium ions are exchanged and replaced by lithium ions in the montmorillonite clay by cationic exchange.

To perform this exchange, 30 g of montmorillonite clay are dispersed in 3 L of distilled water, to which has been added 60 g of $LiNO_3$. The solution must be stirred for two days at 50 °C to perform the exchange. The solution is then centrifuged to separate the lithiated clay from the supernatant which contains additional ions. A last purification step is done by dispersing the clay in 3 L of distilled water and centrifuging again. The clay is then dried during one night under vacuum at 80 °C [49].

To obtain the GPE solution, the mass of LiTFSI and volume of $PYR_{13}FSI$ required were first removed from the argon-filled glovebox. They were mixed together in a synthesis bottle (Figure 2.5a). Afterwards, the PVdF-HFP (Figure 2.5b) and the lithiated clay (Figure 2.5c) were weighed and added to the mixture. Finally, the required volume of acetone was measured and added to the synthesis bottle. The solution was then stirred during one night. A yellow-brownish solution with a low viscosity was obtained and was ready to be used (Figure 2.6).

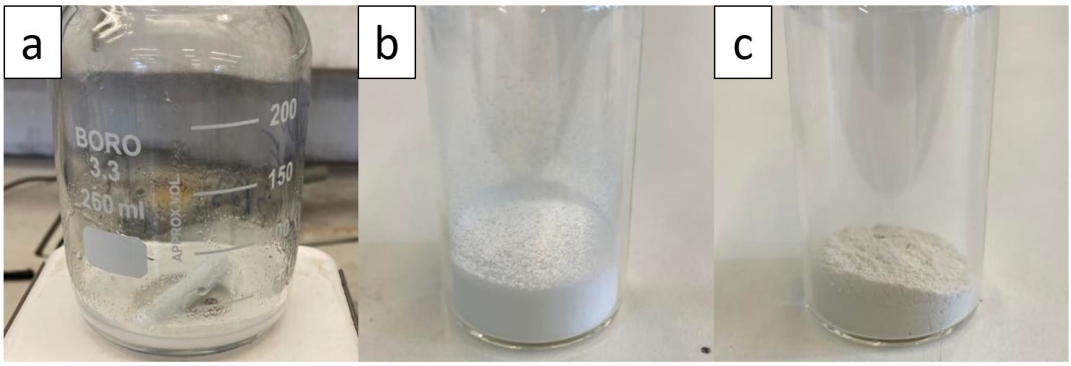

Figure 2.5: a) Binary liquid, b) PVdF-HFP, c) lithiated montmorillionite.

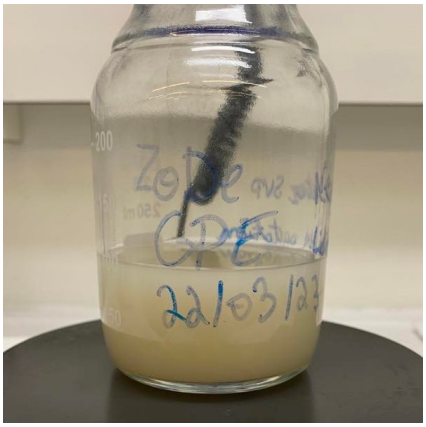

Figure 2.6: GPE solution after one night of stirring.

2.3.2.2 Drop-casting of GPE on current collectors

To apply the GPE in lithium-ion batteries, the GPE solution had to be casted onto the electrodes to obtain a gel-like structure which plays the roles of the electrolyte and separa-

tor. An optimal GPE weight on the electrodes after drying was determined in a work which studied a similar GPE in lithium metal batteries consisting of a $LiCoO_2$ positive electrode and a lithium metal negative electrode. This optimal weight determined corresponds to about 40 mg/cm^2 [49]. This amount of GPE was therefore used as a first target in this work.

Before being applied in half-cell and full-cell configurations, the GPE was studied alone. To do so, the GPE was drop-casted on stainless-steel current collectors. Taking into account that the stainless-steel current collector diameter was of 15.5 mm, the target amount of GPE on the current collectors after drying was of 75.5 mg. Knowing that acetone corresponds to 89.15% of the total solution and was completely evaporated during the drying process, the amount of GPE solution which had to be casted on the current collectors before drying was of 695.9 mg. The target weights were kept in mind during the casting process.

The main casting process investigated in this work was drop-casting. Drop-casting was performed on current collectors with a glass Pasteur pipette. During the process, the current collectors were set on a plate heated to 45°C, to facilitate the evaporation of acetone. To determine the number of drops which had to be added on the current collectors, one drop of solution was quickly weighed with an analytical balance and corresponded to 6.3 mg. This led to the conclusion that about 110 drops of solution were required for each current collector. Once the process was over, the electrodes with GPE were dried overnight at 45°C and 20 mbar to remove acetone and part of the water present in the electrolyte. A GPE-casted current collector can be observed in Figure 2.7. It can be observed that the GPE did not spread completely to the sides of the current collector. This can probably be attributed to the smooth surface of the stainless-steel current collector which hindered the adhesion of GPE and to the fast evaporation of acetone during the casting process which did not leave enough time for the GPE to spread completely.

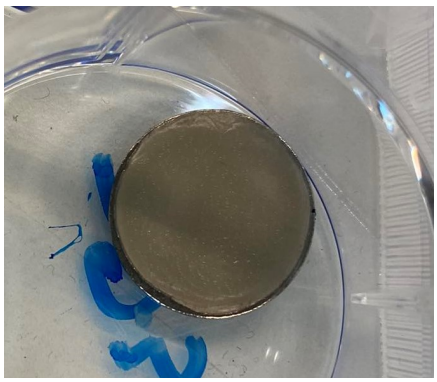

Figure 2.7: GPE-casted current collector after drying.

Before being transferred to the glovebox, the GPE-casted current collectors were weighed to determine if the required amount of GPE had been added. It was observed that instead of having 40 mg/cm^2 on the current collectors, about 50 mg/cm^2 were obtained. This might be explained by the fact that the drop of solution weighed before performing the process was weighed too slowly and that part of the acetone had already evaporated. This

led to the addition of too many drops of solution on the current collectors and therefore a higher mass than the one targeted. For the study of the stability of the electrolyte, the expected consequence is that the thickness of the GPE layer is higher and therefore reduces the risk of internal short-circuit, as more distance is put between both current collectors.

The current collectors were then transferred to the argon-filled glovebox and were ready to be assembled in coin cells.

2.3.2.3 Cell assembly

To study the electrochemical stability of GPE through cyclic voltammetry, coin cells containing two GPE-casted stainless-steel current collectors were assembled. No separator was needed as GPE already separates both current collectors. Two GPE-casted current collectors were used instead of only one to make sure that the GPE thickness was sufficient to avoid short-circuits. Indeed, it was seen that the GPE did not spread completely to the sides of the current collectors and using a bare current collector as counter electrode might induce short-circuits if the current collectors touch on their sides.

2.3.2.4 Cyclic voltammetry characteristics

Cyclic voltammetry was performed with the Biologic VMP3 multichannel potentiostat. Different cyclic voltammetry regimes were applied: between 0 and 1.5 V, 0 and 2 V, 0 and 2.5 V, 0 and 3 V, 0 and 3.5 V, 0 and 4 V. The scan rate was set to 5 mV/s and 5 cycles were performed for each voltage range. Only the width of the electrochemical stability window could be determined since the system studied did not contain a reference electrode.

2.3.3 Results and discussion

2.3.3.1 Cyclic voltammetry

The cyclic voltammetry results of the GPE can be observed in Figures 2.8a and 2.8b. It must be noted that about 50 mg/cm^2 were put on each stainless-steel current collector.

By observing the cyclic voltammetry results until 3 V shown in Figure 2.8a and comparing them to the stability of the classical liquid electrolyte, it can be seen that the stability of the GPE is similar to that of the classical liquid electrolyte for a voltage range of 2 V. When a voltage range of 2.5 to 3 V is considered, the GPE becomes slightly less stable than the classical liquid electrolyte. An increasing current is indeed observed as the voltage range is increased. However, the intensities of the currents are once again negligible in comparison to the classical currents applied during galvanostatic cycling and corresponding to a C-rate of C, for the masses of active material used in this work.

When even higher voltage ranges are studied, such as 0-3.5 V and 0-4 V, the stability of the GPE decreases further more as can be seen in Figure 2.8b. The stability results of the range 0-3.5 V could still be considered stable because the currents reached are small. However, when the voltage range 0-4 V is studied, it can be seen that the current increases and reaches a peak at about 0.75 mA. This peak might indicate undesirable degradation reactions of

the electrolyte. Nevertheless, it occurs when large voltage windows are considered. An issue which might be pointed out is that it is not known at which potential *versus* a reference this instability occurs. However, a similar type of GPE has been investigated in the literature and was successfully applied experimentally for LCO/Li metal batteries. The LCO/Li metal battery has a voltage of 4.2 V, which is much higher than that of LFP/LTO batteries [49]. Indeed, the LCO electrode has a higher potential *vs.* Li^+/Li than LFP while Li metal has a lower potential than LTO. If a similar type of GPE was stable for the operation of LCO/Li metal batteries, it is expected that the GPE investigated in this work will be stable for the operation of LFP/Li metal, LTO/Li metal and LFP/LTO batteries [54].

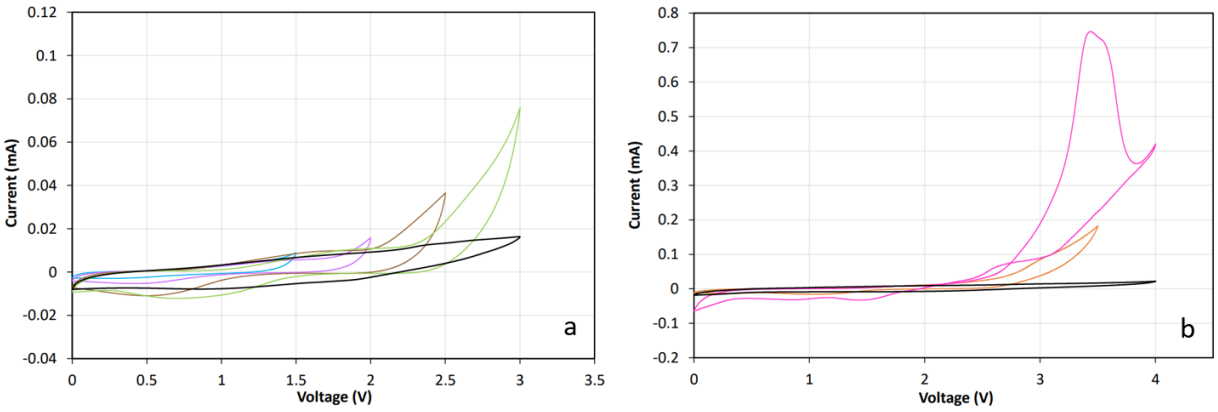

Figure 2.8: Cyclic voltammetry results: GPE, coin cell system: 5^{th} cycle, scan rate of 5 mV/s. a) GPE, voltage ranges: 0-1.5 V (blue), 0-2 V (violet), 0-2.5 V (brown), 0-3 V (green). Classical liquid electrolyte, voltage range: 0-3 V (black). b) GPE, voltage ranges: 0-3.5 V (orange), 0-4 V (pink). Classical liquid electrolyte, voltage range: 0-4 V (black).

2.3.4 Conclusion

This section studied a GPE, which is a safer alternative to the classical liquid electrolyte. A GPE is a semi-solid electrolyte composed of a polymer matrix which traps the liquid electrolyte. The risks of leakage and the safety and environmental issues associated are thus decreased due to the semi-solid property of the electrolyte. The electrochemical stability of the GPE investigated in this work was studied and seems to be sufficient for applications in batteries involving LFP and LTO electrodes. The main issue concerning the GPE is its ionic conductivity, which might be hindered due to the crystallinity of the polymer matrix. However, different elements can increase the ionic conductivity, such as the trapped liquid electrolyte and the addition of clay. The effect of ionic conductivity can be observed through galvanostatic cycling of assembled batteries. If the ionic conductivity of GPE is lower than that of the classical liquid electrolyte, the capacities obtained during cycling will be lower as well.

2.4 Water-in-salt electrolyte

2.4.1 Introduction

Aqueous electrolytes have been increasingly studied to replace the classical organic liquid electrolytes in lithium-ion batteries due to their many advantages. First of all, the issue of flammable organic solvents is completely discarded as the solvent used in aqueous electrolytes is water. In addition, the restrictions in terms of moisture during the cell assembly processes are avoided, leading to a decrease in the constraints and costs. Finally, the aqueous electrolytes display an ionic conductivity much higher than that of classical organic electrolytes, sometimes even twice as significant. Therefore, aqueous electrolytes are safe and environmentally friendly electrolytes, making them highly attractive for energy storage applications [55].

However, aqueous electrolytes have a major disadvantage, which is their narrow electrochemical stability window. Indeed, the stability window is limited by the oxygen (positive electrode) and hydrogen (negative electrode) evolution reactions, respectively depicted by Equations 2.4 and 2.5, which correspond to water electrolysis and lead to a stability window of 1.23 V at a pH of 7. This window is too limited in comparison to the window of classical organic electrolytes, which is usually above 3 V and is used in lithium-ion batteries. This narrow window therefore restricts the applications of aqueous electrolytes for energy storage [15][55][56].

$$2H_2O \rightarrow O_2 + 4H^+ + 4e^- \tag{2.4}$$

$$2H_2O + 2e^- \rightarrow H_2 + 2OH^- \tag{2.5}$$

A new class of aqueous electrolytes, with a wider electrochemical stability window, has been introduced in 2015 by Suo *et al.* [16] and is called water-in-salt (WIS) electrolyte. This electrolyte corresponds to a highly concentrated salt in water and the name "water-in-salt" is given when the salt is present in a higher volume and mass than the solvent. The water-in-salt electrolyte investigated by Suo *et al.* is composed of a 21 $mol/kg_{solvent}$ LiTFSI aqueous solution. LiTFSI (lithium bis(trifluoromethanesulfonyl)imide) is a highly soluble lithium salt in water and has a very high resistance against hydrolysis. The water-in-salt electrolyte synthesised has a very high ionic conductivity, of the order of 10 mS/cm, which is similar to that of classical organic electrolytes. In addition, the electrochemical stability window of the electrolyte is expanded from 1.23 V to about 3 V, between 1.9 V and 4.9 V *vs.* Li^+/Li. This allows its use in lithium-ion batteries with a various range of electrode materials [16][56].

The reasons for the widening of the electrochemical stability window by the water-in-salt electrolyte are widely discussed in the literature. Two types of factors have been associated to this widening: thermodynamic and kinetic factors [56].

Concerning the thermodynamic factors, two main elements can be distinguished: the solvation structure and the pH modification. The solvation structure is associated to the bulk of the electrolyte and is highly different between aqueous electrolytes with a low salt concentration and water-in-salt electrolytes. In aqueous electrolytes with low salt concentration,

the H-bonds of water molecules constitute the ionic network and many free water molecules are in the solvent. When considering the water-in-salt electrolyte, the anion $TFSI^-$ from the highly concentrated LiTFSI salt breaks the structure of the H-bond network and forms a new anionic network to conduct lithium ions. In addition, no more free water molecules are present in the solvent, because they are all used to solvate the salt. This results in a widening of the electrochemical stability window. An illustration of the difference between the solvation structure in an aqueous electrolyte with low salt concentration and in the water-in-salt electrolyte can be seen in Figure 2.9. It must be kept in mind that the solvation structure only impacts the bulk properties of water molecules [16][56].

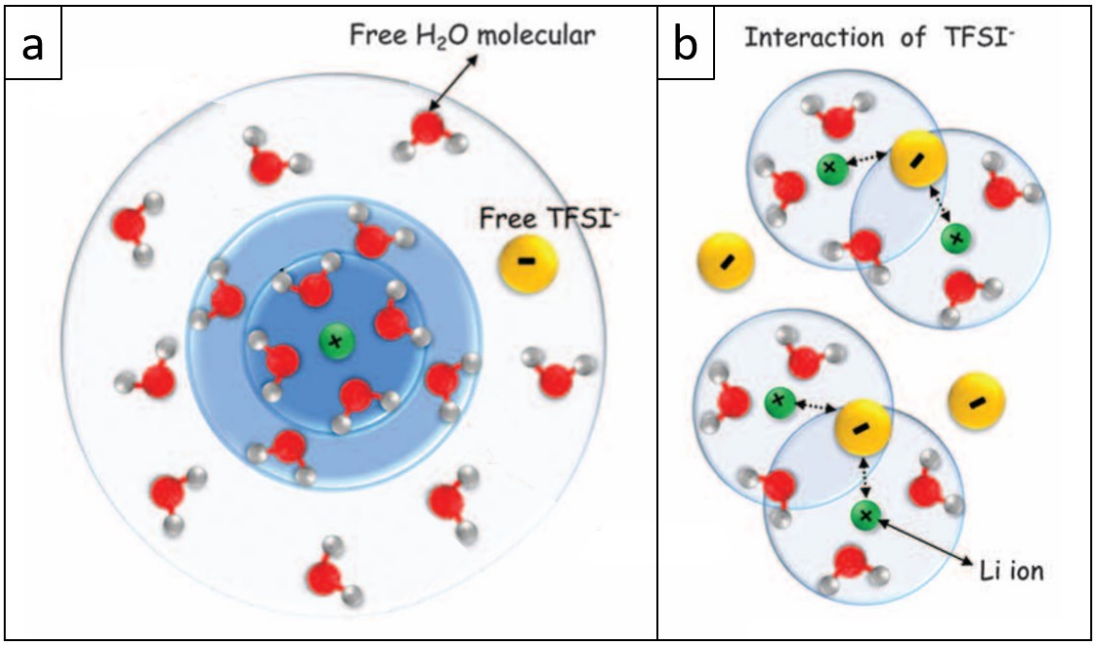

Figure 2.9: a) Solvation structure in an aqueous electrolyte with a low salt concentration, b) solvation structure in a water-in-salt electrolyte. Modified from [16].

Concerning the second element of the thermodynamic factors, the modification of pH, it is known that this modification impacts the potentials of the oxygen and hydrogen evolution reactions through the concentrations of different species involved in the Nernst equation. The pH is modified when the concentrations in H^+ and OH^- change through the oxygen and hydrogen evolution reactions and this therefore allows to modify the electrochemical stablity window, more precisely to widen it. However, the change in the electrochemical stability window is usually very small and thus negligible [56].

The kinetic factors also contain two elements and are more focused on interface relationships as the oxygen and hydrogen evolution reactions occur at the interface between the electrolyte and the electrodes. The impacting elements are the solid electrolyte interphase (SEI) and the electrical double layer, occurring at a smaller scale than the SEI [56].

Concerning the SEI, its formation is widely discussed in the literature. Two main theories are discussed. The first one claims that the modification of the solvation structure due to

the increased salt concentration leads to a change in the reduction potential of the anion $TFSI^-$, which reduces before water. This reduction leads to the formation of a layer of LiF on the negative electrode. In addition, other reactions also occur with dissolved gases such as O_2 and CO_2 which lead to the formation of layers of Li_2CO_3 and Li_2O which also cover the negative electrode. The second theory claims that water decomposition happens and leads to the formation of OH^-, which perform a nucleophilic attack on the anions $TFSI^-$. This induces the formation of a SEI layer on the negative electrode. Both of those theories explain the formation of a SEI layer on the negative electrode and really show that the nature of the salt is of primary importance. Indeed, the $TFSI^-$ anion is a major player in the production of the SEI. Both theories are illustrated in Figure 2.10 [56].

When focusing on a smaller scale, the second kinetic factor concerns the electrical double layer formed at the surface of the electrodes, more precisely the positive electrode. Molecular dynamics simulations and experiments showed that the inner Helmholtz plane of the electrical double layer at the positive electrode is completely filled by $TFSI^-$ anions when the water-in-salt electrolyte is considered. This means that no water molecule is directly in contact with the positive electrode surface and the potential at which the oxygen evolution reaction occurs is increased, leading to a widened electrochemical stability window. An illustration of this kinetic factor can be seen in Figure 2.10. When the negative electrode is taken into account, it was shown through molecular dynamics simulations that Li^+ ions surrounded by water were in the inner Helmholtz plane. The presence of water at the surface of the negative electrode promotes the decomposition of water and therefore has a negative impact and participates to the narrowing of the electrochemical stability window [56].

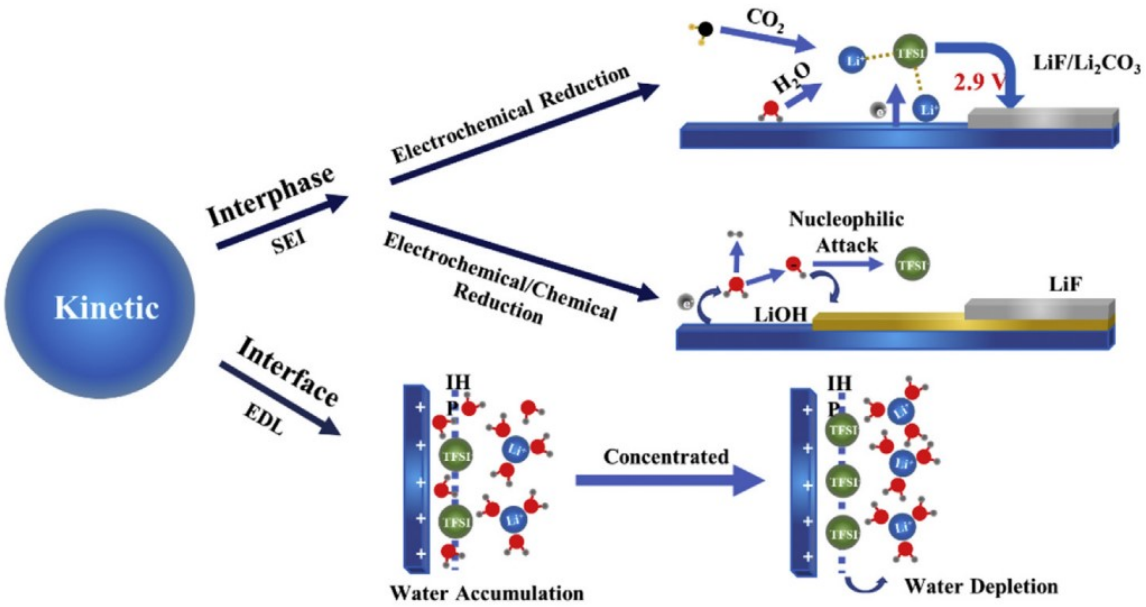

Figure 2.10: Illustration of the kinetic factors explaining the widening of the electrochemical stability window in the water-in-salt electrolyte [56].

To obtain an aqueous electrolyte with an even wider electrochemical stability window, improvements of the water-in-salt electrolyte have been researched in the literature. A few examples are the following. The water-in-bisalt electrolyte, involving a 21 mol/$kg_{solvent}$ LiTFSI and 7 mol/$kg_{solvent}$ LiOTf (lithium trifluoromethanesulfonate) aqueous solution was investigated by Suo *et al.* [57]. This electrolyte leads to a concentration in Li^+ cations of 28 mol/$kg_{solvent}$, which allows to obtain a stronger SEI and an electrochemical stability window of 3.1 V [57]. Another improvement of the water-in-salt electrolyte, developed by Chen *et al.* [58], involves an aqueous electrolyte composed of a 42 mol/$kg_{solvent}$ LiTFSI and 21 mol/$kg_{solvent}$ Me_3EtN.TFSI aqueous solution, leading to a concentration in Li^+ of 63 mol/$kg_{solvent}$. This electrolyte is called water-in-hybrid-salt and allows to obtain an electrochemical stability window of 3.25 V [58].

Even if the water-in-salt electrolyte has numerous advantages from the safety and the environmental point of views, it has also disadvantages which cannot be ignored. A major disadvantage is the cost of the water-in-salt electrolyte, which is very high due to the high lithium salt concentration required [15]. In addition, the use of the $TFSI^-$ based salt restricts the type of current collector which can be used. LiTFSI corrodes severly aluminium current collectors and this therefore restricts the use of LiTFSI based electrolytes for lithium-ion batteries [11]. It was also shown that copper is affected by corrosion when used in LiTFSI aqueous-based electrolytes [59]. The current collectors used in the literature with the 21 mol/$kg_{solvent}$ LiTFSI water-in-salt electrolyte are stainless-steel current collectors [16].

2.4.2 Experimental

2.4.2.1 Synthesis of the electrolyte

The water-in-salt (WIS) electrolyte studied was inspired by the article written by Suo *et al.* [16]. The electrolyte was synthesised by preparing a 21 mol/$kg_{solvent}$ aqueous solution of LiTFSI, lithium bis(trifluoromethanesulfonyl)imide (99.9%, Solvionic, S001A250, L19112501). In a first approach, 6.03 g of LiTFSI were dissolved in 1 g of MilliQ water. LiTFSI is a highly hygroscopic compound, as can been seen by the dissolution drops present on the sides of the powder in Figure 2.11a. It is therefore kept in the glovebox under argon atmosphere and must either be weighed in the glovebox or weighed as quickly as possible if taken out of the glovebox to avoid a change of composition due to the presence of water. The lithium salt was dissolved in MilliQ water using magnetic stirring. At the start of the dissolution, the solution was turbid as can be seen in Figure 2.11b. The dissolution can be facilitated by heating the solution up to 40 °C. Indeed, LiTFSI is highly thermally stable, as it melts at 236 °C without decomposition and decomposes at 360 °C [39]. When the dissolution was over, the obtained electrolyte was transparent and viscous (Figure 2.11c). The water-in-salt electrolyte was kept under agitation during its period of use. If it was not kept under agitation, the solution solidified into a white gel, as can be seen in Figure 2.11d.

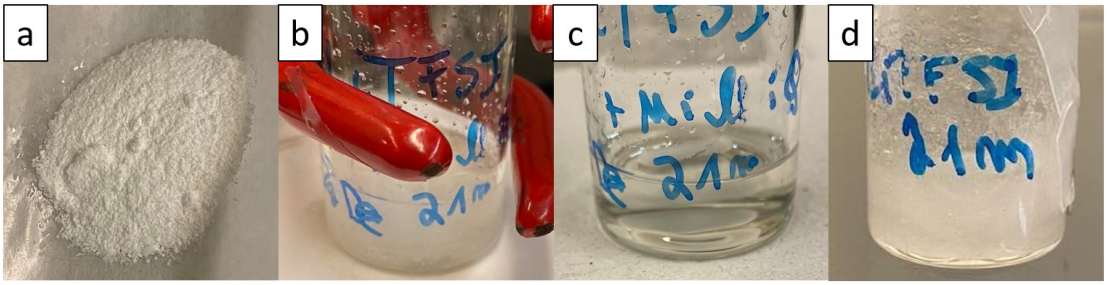

Figure 2.11: a) LiTFSI powder, b) beginning of the dissolution of the water-in-salt electrolyte, c) final water-in-salt electrolyte, d) solidified water-in-salt electrolyte.

2.4.2.2 Electrode stability in the WIS electrolyte

The LFP and LTO electrodes used in this work were manufactured using a water-based process developed at the NCE laboratory. This water-based process allows to avoid the use of toxic solvents and binder, which are respectively replaced by water and xanthan gum. Xanthan gum is a water-soluble binder and therefore allows the recovery of the current collector by immersing the electrode in water [21].

The advantage of the water-in-salt electrolyte is that it allows to avoid the use of flammable and toxic solvents because it is composed of a lithium salt dissolved in water. However, the stability of the electrodes in this electrolyte must be studied due to the aqueous base of the electrolyte.

To study the stability of the electrodes, electrode samples were immersed in the electrolyte and the behaviour over time was studied. The objective was to determine if the xanthan gum binder could withstand the contact with the water-in-salt electrolyte.

The electrodes used to study the stability of the binder were LFP electrodes prepared according to the procedure described in Chapter 1. Two electrodes, called W1 and W2, were immersed in MilliQ water to observe the classical decomposition of the electrode material in water. Two electrodes, called W3 and W4, were immersed in the 21 $mol/kg_{solvent}$ LiTFSI aqueous solution to observe the potential decomposition of the electrode material in the water-in-salt electrolyte. The set-up can be observed in Figure 2.12.

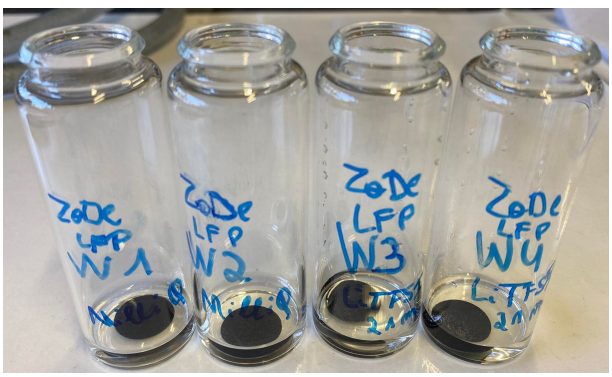

Figure 2.12: Set-up for the electrode stability test in the water-in-salt electrolyte.

2.4.2.3 Cell assembly

To study its electrochemical stability, the water-in-salt electrolyte was subjected to cyclic voltammetry. Coin cells containing stainless-steel spacers with 2 Celgard separators soaked in 160 μL of water-in-salt electrolyte were assembled. The chosen volume was higher than in the case of the classical liquid electrolyte because the water-in-salt electrolyte is highly viscous and a higher volume was required to wet the separators sufficiently.

2.4.2.4 Cyclic voltammetry characteristics

Cyclic voltammetry was performed with the Biologic VMP3 multichannel potentiostat. Different cyclic voltammetry regimes were applied: between 0 and 1.5 V, 0 and 2 V, 0 and 2.5 V, 0 and 3 V. The scan rate was set to 5 mV/s and 5 cycles were performed for each voltage range. Once again, only the width of the stability window could be determined.

2.4.2.5 Improvement of the water-in-salt electrolyte: water-in-bisalt electrolyte synthesis and cyclic voltammetry testing

The water-in-bisalt (WIBS) electrolyte tested was inspired by the article written by Suo *et al.* [57]. The electrolyte was synthesised by preparing a 21 mol/$kg_{solvent}$ LiTFSI and 7 mol/$kg_{solvent}$ LiOTf aqueous solution, leading to a concentration in Li^+ of 28 mol/$kg_{solvent}$. LiOTf is also a lithium salt, lithium trifluoromethanesulfonate (99.995 % trace metal basis, Sigma-Aldrich, PCode 1003382549, Source MKCH6451). This electrolyte is said to be more stable electrochemically than the classical water-in-salt electrolyte [57].

In a first approach, 3.01 g of LiTFSI were dissolved in 0.5 g of MilliQ water using magnetic stirring. Once the salt was completely dissolved, 0.55 g of LiOTf were added to the solution. LiOTf, visible in Figure 2.13a, is also highly hygroscopic and is stored in the glovebox. The final electrolyte obtained was a transparent viscous solution, which can be observed in Figure 2.13b. The WIBS electrolyte was also kept under agitation during its use period. If not agitated, the electrolyte solidified into a white gel which can be seen in Figure 2.13c. This solidification was even faster than in the case of the WIS electrolyte.

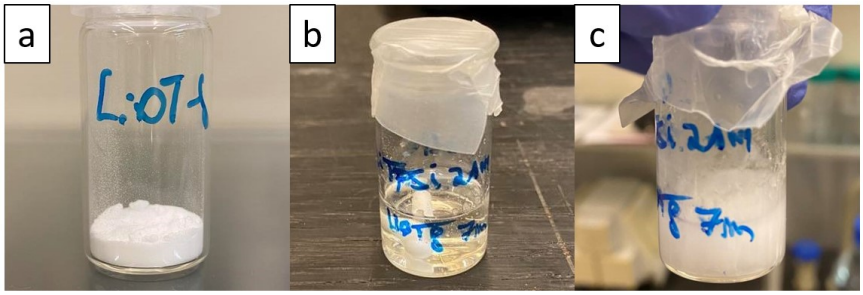

Figure 2.13: a) LiOTf powder, b) final water-in-bisalt electrolyte, c) solidified water-in-bisalt electrolyte.

The water-in-bisalt electrolyte was subjected to the same cyclic voltammetry regime in coin cell configuration as the water-in-salt electrolyte.

2.4.2.6 Additional study of the WIS electrolyte: three-electrode system

The coin cell configurations assembled and subjected to cyclic voltammetry only allow to determine the width of the electrochemical stability window of the studied electrolyte and not its position *versus* a reference. However the position of the window is a critical information, which allows to determine what material can or cannot be used as electrode with the studied electrolyte. The position of the window can be determined using a three-electrode system, which contains a reference electrode in between the working and counter electrodes. To go deeper into the study of the water-in-salt electrolyte, three-electrode systems have been studied with the help of the researchers of the University of Louvain, more precisely from the Institute of Condensed Matter and Nanosciences, which possesses the required three-electrode equipment.

First of all, the water-in-salt electrolyte was synthesised. An additional argon bubbling step was performed to remove oxygen from the sample, which could induce undesirable reactions during the experiments. The bubbling set-up can be observed in Figure 2.14. The green needle injected argon into the electrolyte while the yellow needle allowed the air to escape the bottle. The bubbling of the electrolyte was performed for about 15 min.

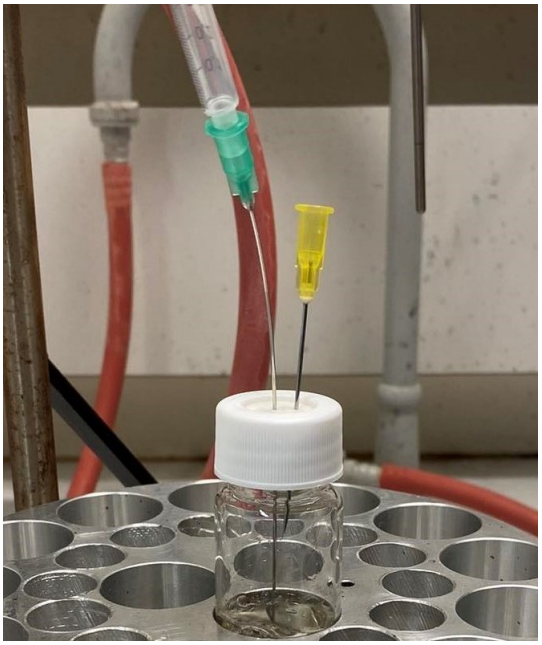

Figure 2.14: Set-up for the argon bubbling of the water-in-salt electrolyte.

The stability of the electrolyte was studied by performing cyclic voltammetry between stainless-steel electrodes and against an Ag wire reference, to obtain results *vs.* Ag^+/Ag. The oxido-reduction potential of Ag^+/Ag depends on the medium in which the reference is immersed because it is a pseudo-reference. Therefore, the Ag^+/Ag reference had to be calibrated by measuring its potential against a stable reference, with a potential which does not change in function of the medium. The reference chosen for the calibration was Ag/AgCl. Once the calibration was done, the results of the stability measurements of the

electrolyte could be observed against the Ag^+/Ag reference. Those results could then be converted to be observed against the Li^+/Li reference.

To study the electrochemical window of the electrolyte, the three-electrode system had to be assembled. The three-electrode system used for this study was a Swagelok T-cell, which consists of a working electrode, a counter electrode and a reference electrode. A schematic representation of a Swagelok T-cell can be observed in Figure 2.15.

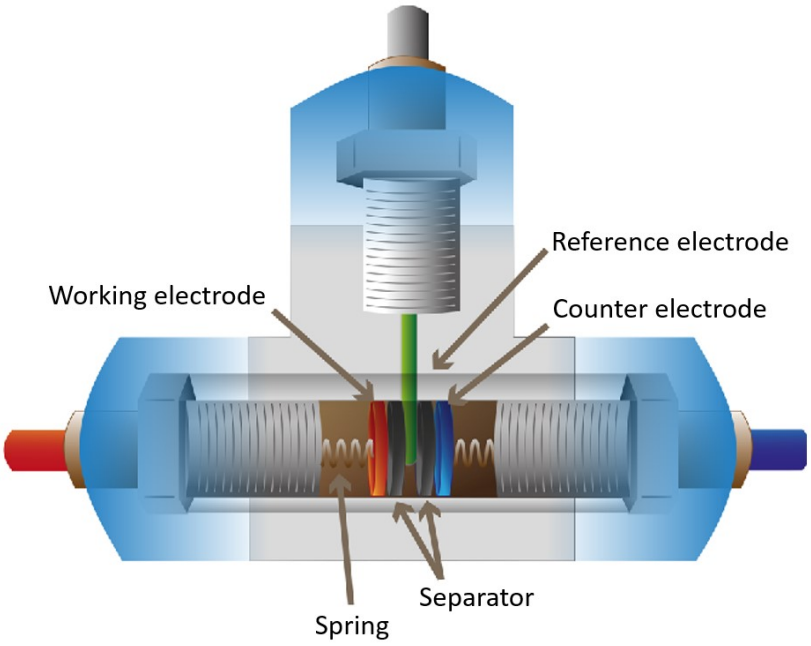

Figure 2.15: Schematic representation of a Swagelok T-cell three-electrode system, modified from [60].

In this case, both the working and counter electrodes were stainless-steel plungers and the reference was an Ag wire connected to a stainless-steel plunger. The different elements used to construct the three-electrode system can be observed in Figure 2.16. The working and counter electrodes can be seen in Figures 2.16a and 2.16b. Only of one of the electrodes possessed a spring to press the different components together when the Swagelok T-cell was sealed. The support of the reference electrode can be seen in Figure 2.16c. An Ag wire of about 3 cm was polished, cleaned with acetone, and tied to the support. In addition, the support of the reference was covered in Teflon in order to isolate the support and prevent short-circuits. Once it was done, the Ag wire was cut to only keep 0.5 to 1 cm of wire. The final reference electrode can be seen in Figure 2.16d. The body of the Swagelok T-cell can be observed in Figure 2.16e. It was made of PFA polymer (perfluoroalkoxy alkane) instead of the more traditional stainless-steel body to once again decrease the risks of short-circuit. Figures 2.16f and 2.16g show the nuts and the ferrules which were respectively put on the body of the Swagelok and on the electrodes and participated to the sealing of the Swagelok T-cell.

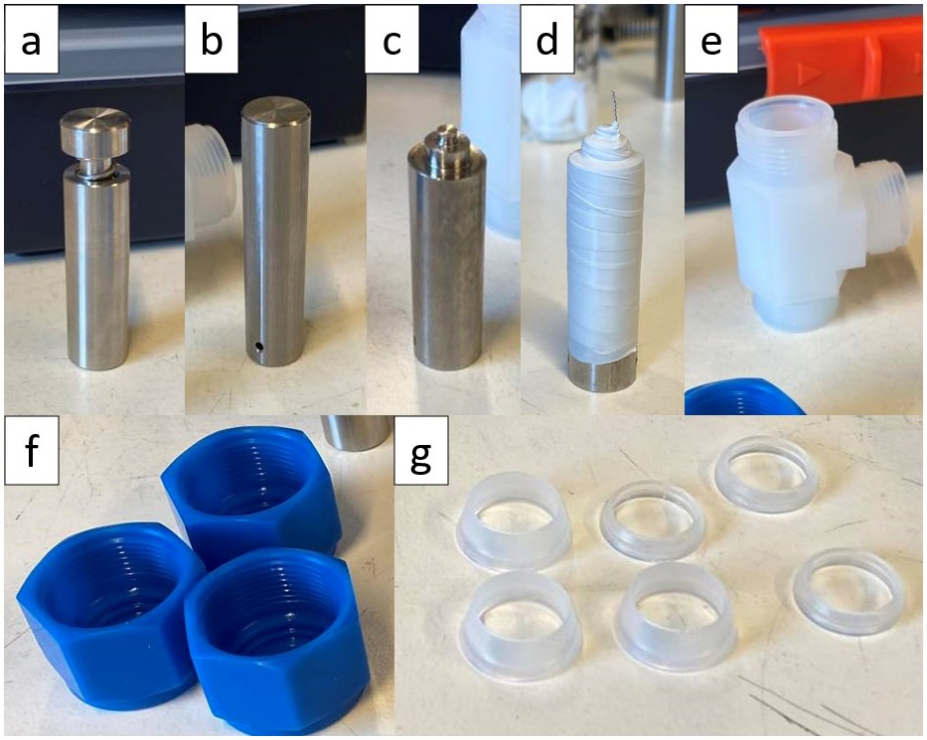

Figure 2.16: Components of the Swagelok T-cell: a) working electrode, b) counter electrode, c) reference electrode support, d) final reference electrode e) body of the Swagelok T-cell, f) sealing nuts, g) ferrules.

The assembly of the cell could be performed following Figure 2.15. The counter electrode with two ferrules was added to the PFA body and partially sealed with a nut. A glass fiber separator of 12.7 mm diameter was put on top of the counter electrode. To continue, the reference electrode with ferrules was inserted on top of the separator, as can be seen in Figure 2.17. Ten to twenty drops of electrolyte were added on the reference and the separator, to soak both of them with the electrolyte. When the position of the reference was well adjusted, the nut could be used to seal the reference electrode in its place. The second separator was then added, as well as the working electrode with ferrules. The working electrode contained a spring, which had to be contracted to press all of the components together. Finally, the third nut was added to seal the working electrode in its place. Once all of the components were well adjusted, the three nuts were sealed completely and the Swagelok T-cell was ready.

The cell was let to settle for a about 15 to 20 min so that the electrolyte soaked completely the separators and reference. Afterwards, the cell could be connected to the potentiostat and the cyclic voltammetry measurements could be performed. The potentiostat used for the experiment was a Biologic VMP3 mutlichannel potentiostat. The cell was connected to the potentiostat as shown in Figure 2.18. The red connection corresponded to the working electrode, the blue connection corresponded to the counter electrode and the white connection corresponded to the reference electrode.

Figure 2.17: Inside view of the Swagelok T-cell. The reference had to be positioned against the first separator and covered by the electrolyte.

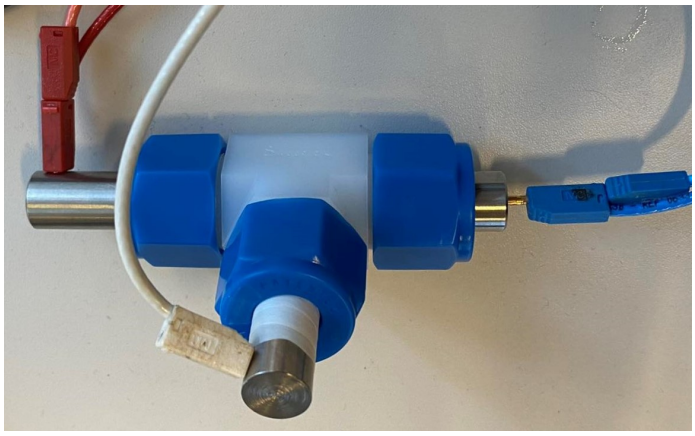

Figure 2.18: Assembled Swagelok T-cell connected to the VMP3 Biologic potentiostat.

Two different cyclic voltammetry measurements were performed to determine the electrochemical stability window of the electrolyte. The first measurement allowed to observe the cathodic degradation of the electrolyte. To do so, cyclic voltammetry was performed between 0 V and 3 V *vs.* Ag^+/Ag, with a scan rate of 0.05 mV/s. The second measurement was performed on a new cell and allowed to observe the anodic degradation of the electrolyte. To do so, cyclic voltammetry was performed between -3 V and 0 V *vs.* Ag^+/Ag, with a scan rate of 0.05 mV/s.

Concerning the calibration of the Ag^+/Ag reference, it was performed against an Ag/AgCl reference, which was stored in a KCl solution. The tips of the Ag^+/Ag and Ag/AgCl references were immersed in the water-in-salt electrolyte and the potential difference between the Ag/AgCl and the Ag^+/Ag references was measured using a voltmeter.

2.4.3 Results and discussion

2.4.3.1 Electrode stability in the WIS electrolyte

The degradation over time of electrode W1 in MilliQ water can be seen in Figure 2.19. The results for electrode W2 are available in the Appendices. The degradation over time of electrode W3 in the water-in-salt electrolyte can be seen in Figure 2.20. The results for electrode W4 are available in the Appendices.

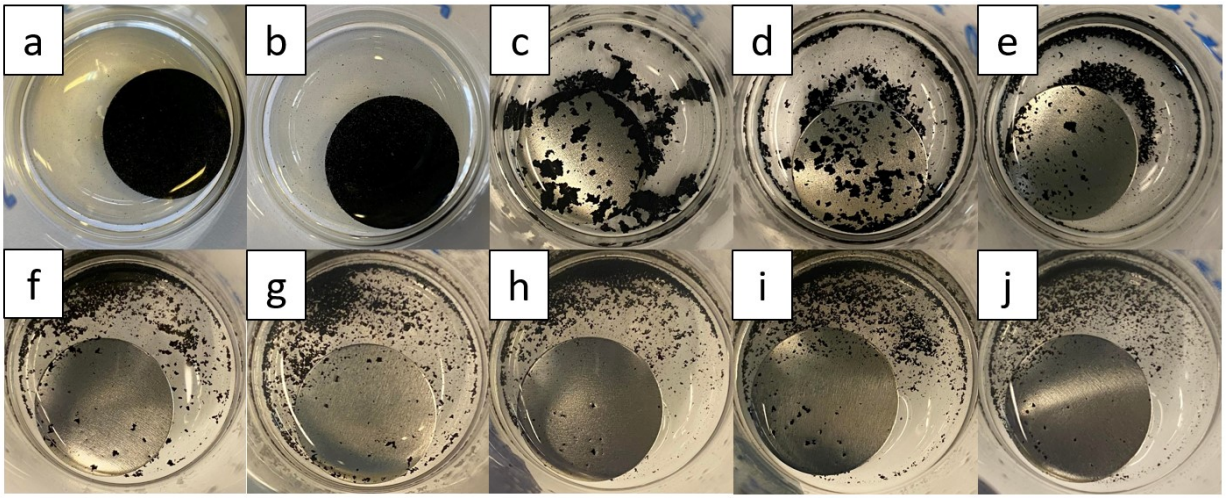

Figure 2.19: Degradation of electrode W1 in MilliQ water: a) t_0, b) t_0 + 1 h, c) t_0 + 19 h, d) t_0 + 21 h, e) t_0 + 27 h, f) t_0 + 43 h, g) t_0 + 49 h, h) t_0 + 115 h, i) t_0 + 166 h, j) t_0 + 213 h.

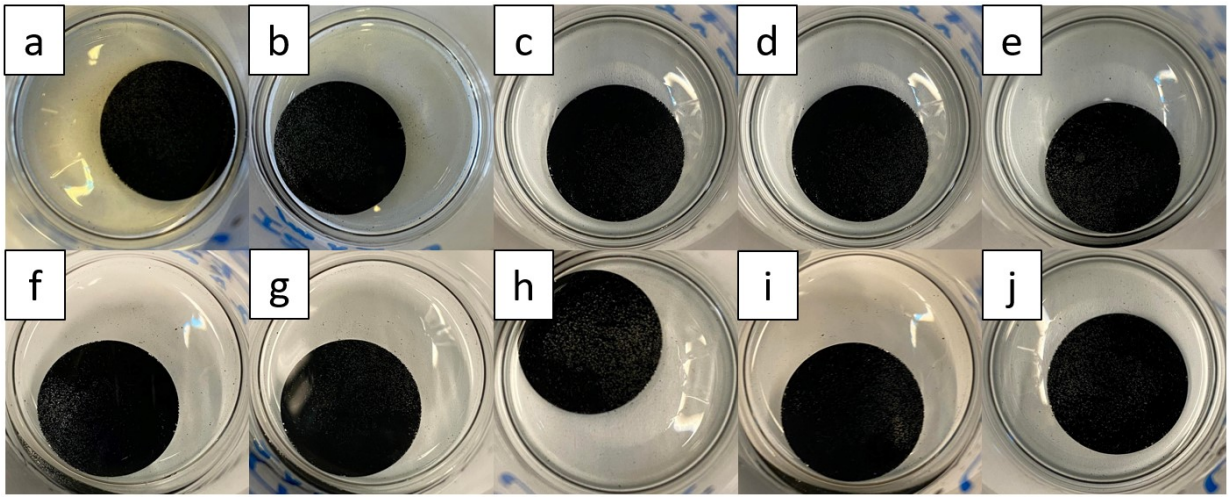

Figure 2.20: Degradation of electrode W3 in the LiTFSI 21 mol/$kg_{solvent}$ aqueous solution: a) t_0, b) t_0 + 1 h, c) t_0 + 19 h, d) t_0 + 21 h, e) t_0 + 27 h, f) t_0 + 43 h, g) t_0 + 49 h, h) t_0 + 115 h, i) t_0 + 166 h, j) t_0 + 213 h.

It can clearly be seen from Figure 2.19 that the electrode material detaches from the current collector over time due to the immersion in water. This is expected as xanthan

gum is a water-soluble binder and therefore decomposes, leading to the dispersion of the electrode material in water. This dissolution of xanthan gum is an advantage of the water-based process as it allows to separate the electrode material from the current collector and therefore facilitates recycling.

When observing Figure 2.20, it can be seen that the electrode material seems quite stable over time as no material detaches from the current collector. This leads to the conclusion that the xanthan gum binder does not dissolve in the LiTFSI 21 mol/$kg_{solvent}$ aqueous solution. This can probably be explained by the fact that the solution is almost fully saturated in salt, leading to a decrease in the number of free water molecules available to dissolve the binder. The binder is therefore able to withstand the contact with the electrolyte and the integrity of the electrode material is maintained.

2.4.3.2 Cyclic voltammetry results WIS and WIBS: Coin cell system

The results of the cyclic voltammetry measurements in coin cell configuration for the water-in-salt and the water-in-bisalt electrolytes can be seen respectively in Figures 2.21 and 2.22.

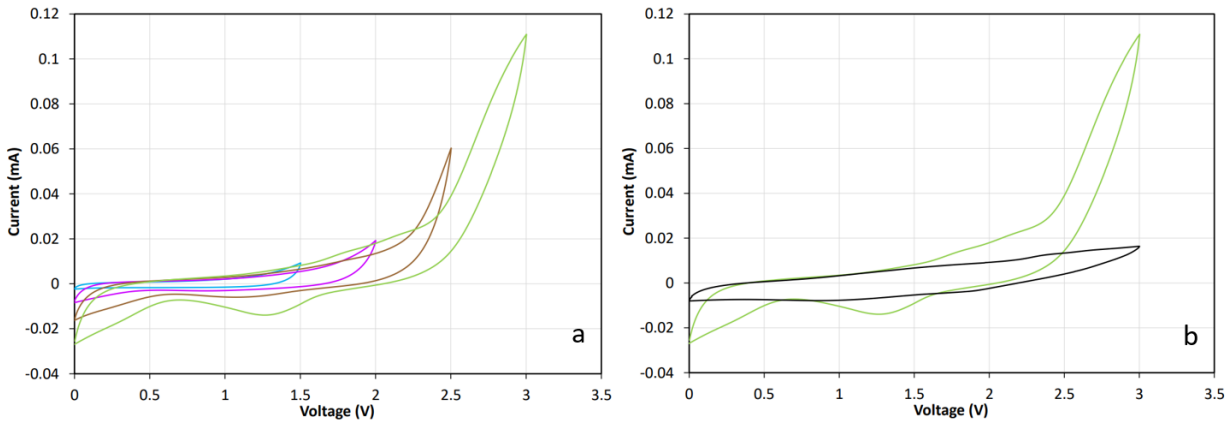

Figure 2.21: Cyclic voltammetry results: water-in-salt electrolyte, coin cell system: 5^{th} cycle, scan rate of 5 mV/s. a) WIS electrolyte, voltage ranges: 0-1.5 V (blue), 0-2 V (violet), 0-2.5 V (brown), 0-3 V (green). b) WIS electrolyte, voltage range: 0-3 V (green). Classical liquid electrolyte, voltage range: 0-3 V (black).

Figure 2.21a shows the cyclic voltammetry results of the water-in-salt electrolyte for different voltage ranges until 3 V. It can be seen that the stability of the electrolyte decreases with increasing voltage ranges, as expected. When considering the classical currents of 0.6 mA and 0.3 mA associated to a C-rate of C for half-cells and full-cells with the active material masses considered in this work, it can be concluded that the electrolyte is quite stable within a voltage range of 2.5 V. Indeed, within the voltage range 0-2.5 V, the maximal current obtained is around five to ten times smaller than the classical currents.

When compared to the classical liquid electrolyte in Figure 2.21b, the water-in-salt electrolyte is clearly less stable when a voltage range of 3 V is tested.

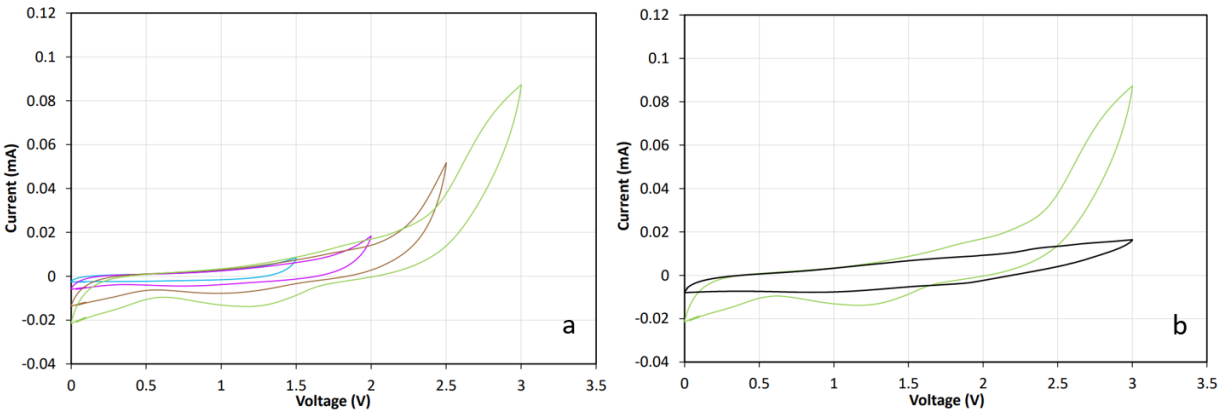

Figure 2.22: Cyclic voltammetry results: water-in-bisalt electrolyte, coin cell system: 5th cycle, scan rate of 5 mV/s. a) WIBS electrolyte, voltage ranges: 0-1.5 V (blue), 0-2 V (violet), 0-2.5 V (brown), 0-3 V (green). b) WIBS electrolyte, voltage range: 0-3 V (green). Classical liquid electrolyte, voltage range: 0-3 V (black).

Figures 2.22a and 2.22b show the cyclic voltammetry results of the water-in-bisalt electrolyte. The results obtained are similar to the water-in-salt electrolyte for the voltage ranges 0-1.5 V and 0-2 V. For the voltage ranges 0-2.5 V and 0-3 V, it can be seen that the evolution of the curves are once again similar to that of the water-in-salt electrolyte with the only difference that the maximum currents achieved are smaller of about 0.02 mA. This shows that the water-in-bisalt electrolyte is indeed more stable electrochemically than the water-in-salt electrolyte, as described in the literature [57].

2.4.3.3 Cyclic voltammetry results WIS: three-electrode system

The results of the calibration of the Ag^+/Ag reference showed a potential difference of -0.06 V between the Ag/AgCl and the Ag^+/Ag references. Knowing that the Ag/AgCl reference used at the laboratory is at 0.2 V *versus* the standard hydrogen electrode (SHE), it is deduced that the Ag^+/Ag reference is at 0.26 V *vs.* SHE. Taking into account that Li^+/Li is at a potential of -3.04 V *vs.* SHE [1], the data obtained from cyclic voltammetry can be converted from the Ag^+/Ag reference to the Li^+/Li reference by adding 3.3 V to the potentials. The corrected data for the cathodic cyclic voltammetry measurement of the water-in-salt electrolyte can be observed in Figure 2.23.

It can be seen from Figure 2.23 that the electrolyte is stable from around 3.45 V until 4.92 V *vs.* Li^+/Li. Afterwards, the current starts to increase and reaches values of the order of 1.2 mA, at which the cyclic voltammetry measurement was stopped due to the high currents. This increase in current is associated to the decomposition of the electrolyte, linked to the electrochemical instability of the electrolyte at the tested potentials. The stability window observed in this cathodic cyclic voltammetry measurement has a width of about 1.5 V.

The LFP electrode has an oxido-reduction potential of about 3.45 V *vs.* Li^+/Li [21], which is included within the stability window of the water-in-salt electrolyte. It is therefore

expected that this material can be used as positive electrode in batteries involving the water-in-salt electrolyte.

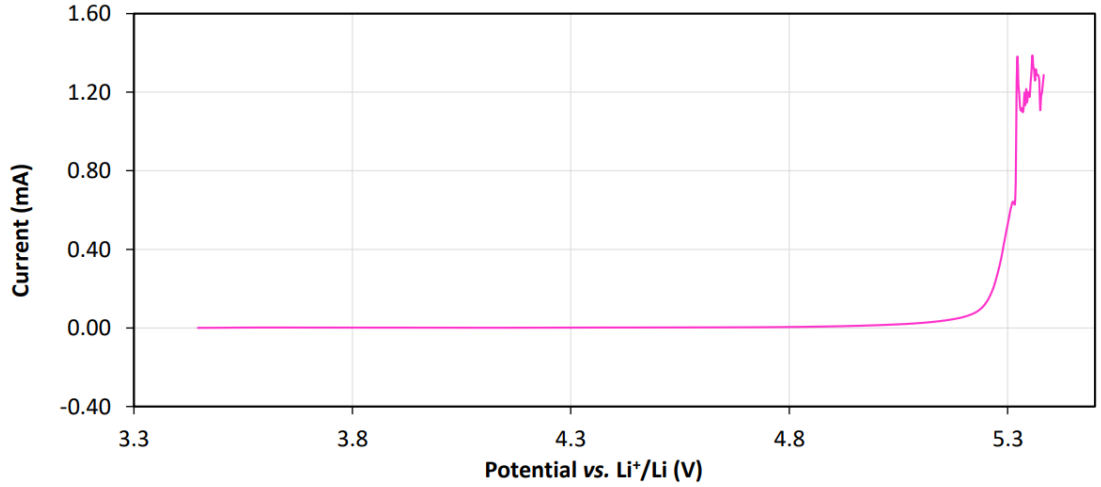

Figure 2.23: Cyclic voltammetry results: water-in-salt electrolyte in three-electrode system: cathodic results, scan rate of 0.05 mV/s.

Concerning the anodic cyclic voltammetry measurement, the corrected data can be observed in Figure 2.24.

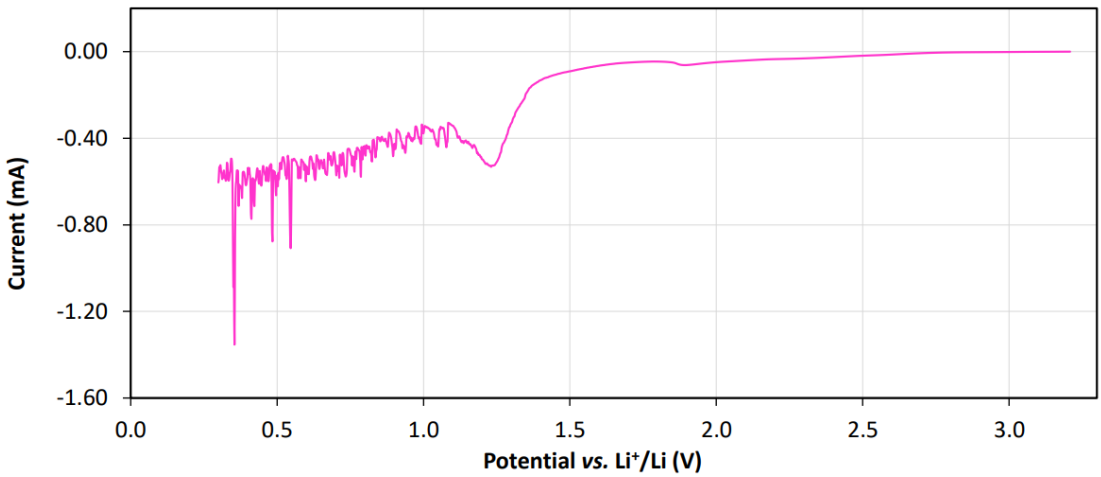

Figure 2.24: Cyclic voltammetry results: water-in-salt electrolyte in three-electrode system: anodic results, scan rate of 0.05 mV/s.

Figure 2.24 shows the voltammetry cycle performed from around 3.2 V to 0.3 V *vs.* Li^+/Li and not the reverse scan for clarity. The complete voltammetry cycle performed before stopping the experiment can be found in the Appendices and includes the reverse scan, which shows even more the instability of the electrolyte.

It can be seen from Figure 2.24 that the moment at which the electrolyte becomes unstable is less clear than for the cathodic results. It can be observed that the current slowly starts to decrease around 2.5 V *vs.* Li^+/Li and it is only when going towards 2 V and 1.5 V *vs.* Li^+/Li that a clear decrease can be observed and be associated to a complete decomposition of the electrolyte. It can probably be considered that the electrolyte is stable from 2.5 V until 3.2 V *vs.* Li^+/Li. The width of the electrochemical stability window on the anodic side is thus of about 0.7 V. The anodic results lead to the conclusion that LTO can probably not be used with this water-in-salt electrolyte. Indeed, LTO has an oxido-reduction potential of about 1.55 V *vs.* Li^+/Li [23], which is not included within the stability window measured in this case.

When looking at both the cathodic and anodic results, it can be seen that the potential range 3.2 V - 3.45 V *vs.* Li^+/Li did not appear in the results. However, it can clearly be expected that the electrolyte is stable within this range. The combination of the cathodic and anodic results therefore lead to a stable electrolyte between 2.5 V and 4.92 V *vs.* Li^+/Li. This leads to an electrochemical stability window with a width of 2.42 V, which is lower than the 3 V width obtained in the literature [16]. This can probably be explained by the synthesis of the water-in-salt electrolyte. The LiTFSI salt is highly hygroscopic and was weighed in the glovebox with a scale with a limited precision. This probably led to a lower mass than expected and the solution obtained had a lower concentration than 21 $mol/kg_{solvent}$ in LiTFSI, which led to a narrower electrochemical stability window.

After the cyclic voltammetry measurements, one of the cells was disassembled to observe the state of the materials. The separators and the tip of the working electrode can be seen in Figure 2.25.

Figure 2.25: State of the separators and the working electrode after the cyclic voltammetry measurements of the water-in-salt electrolyte in three-electrode system.

It can be observed that some parts of the separators, which were initially white, turned to a brownish color. This can be associated to the decomposition of the electrolyte, which led to a deposit on the separators. Analysing the nature of this deposit could allow to understand *via* which reaction the electrolyte decomposed.

2.4.4 Conclusion

This section studied the water-in-salt electrolyte and the water-in-bisalt electrolyte. It was determined that the xanthan gum binder is stable when immersed in the water-in-salt electrolyte, meaning that the electrode material should not decompose when put in contact with the electrolyte in a battery. To continue, the water-in-salt and water-in-bisalt electrolytes were subjected to cyclic voltammetry in coin cell configurations. Those measurements lead to the observations that the water-in-salt and water-in-bisalt electrolytes are stable for a window of about 2.5 V, but it is not known where this window is *versus* a reference. In addition, the water-in-bisalt electrolyte is more stable than the water-in-salt electrolyte, as expected. The water-in-bisalt electrolyte was not studied further in this work because its behaviour was expected to be similar to that of the water-in-salt electrolyte, even though it is slightly more stable. Finally, the water-in-salt electrolyte was subjected to cyclic voltammetry in a three-electrode configuration, which allows to determine the position of the electrochemical stability window *versus* a reference. This allowed to determine that the water-in-salt electrolyte is stable from 2.5 V to 4.92 V *vs.* Li^+/Li.

From the stability window, it could be concluded that the LFP electrode can be used with the water-in-salt electrolyte because its potential is within the stability window. This electrode was characterised in half-cell configuration. However, since the electrolyte is aqueous, it could not be characterised in half-cell configuration with a lithium metal negative electrode due to safety issues. To overcome this problem, the LFP electrode had to be characterised in a three-electrode configuration, against an Ag^+/Ag reference and an activated carbon fabric negative electrode. The results of the half-cell characterisation of LFP are available in Chapter 3. Concerning the LTO electrode, it was seen that its potential is a bit below the stability window. It was therefore not characterised in half-cell configuration. Nevertheless, full LFP/LTO batteries, with a voltage of 1.85 V, were characterised with the water-in-salt electrolyte to observe the expected electrolyte decomposition and the results are available in Chapter 4.

2.5 Global comparison of the electrolyte stability and conclusion

To finish this chapter, a final comparison is performed between the different electrolytes investigated. This graphical comparison can be seen in Figure 2.26.

It must be noted that the results shown were obtained through cyclic voltammetry performed with a coin cell in a two-electrode configuration. The results therefore show the overall stability of each electrolyte but this stability is not compared to a reference such as Li^+/Li. To be more precise, it would be beneficial to perform the same measurements in a three-electrode system such as a Swagelok T-cell, shown in Section 2.4.2.6.

The most electrochemically stable electrolyte is the classical liquid electrolyte, 1 M $LiPF_6$ in (1:1 vol.%) EC:DEC. This result was expected as this electrolyte is the one used commercially. However, this electrolyte presents different issues in terms of safety and environment

as explained in this chapter.

The second most stable electrolyte is the GPE, which allows to discard the issue of leakage and the associated toxicity and flammability of the classical electrolyte thanks to the semi-solid state of the GPE. This electrolyte could be a good candidate to replace the classical liquid electrolyte. The electrochemical performances of this electrolyte were determined by performing galavanostatic cycling of half-cells and full-cells to see how the electrodes react in such a medium. The main issue in this case was to determine if the ionic conductivity of the electrolyte is high enough so that not too much capacity of the electrodes is lost. The results for the half-cells and full-cells with GPE are presented in Chapters 3 and 4.

The third and the least stable electrolyte type is the water-in-salt electrolyte (or water-in-bisalt electrolyte). This electrolyte allows to discard the toxicity associated to carbonates while keeping the liquid state and thus the high ionic conductivity. The water-in-salt electrolyte was used to perform galavanostatic cycling of half-cells in three-electrode configuration and full-cells in coin cell configuration. The main issue expected in this case concerned the ability of performing cycling in such an electrolyte, which is not well documented concerning LFP and LTO electrodes produced with a water-based process. In addition, it was expected that the full-cells would most probably not withstand cycling as the voltage range tested is slightly out of the limits of the stability window of the water-in-salt electrolyte. The results for the half-cells and full-cells with the water-in-salt electrolyte are presented in Chapters 3 and 4.

The next chapter focuses on half-cell configurations and on determining the electrochemical performances associated to one composite electrode.

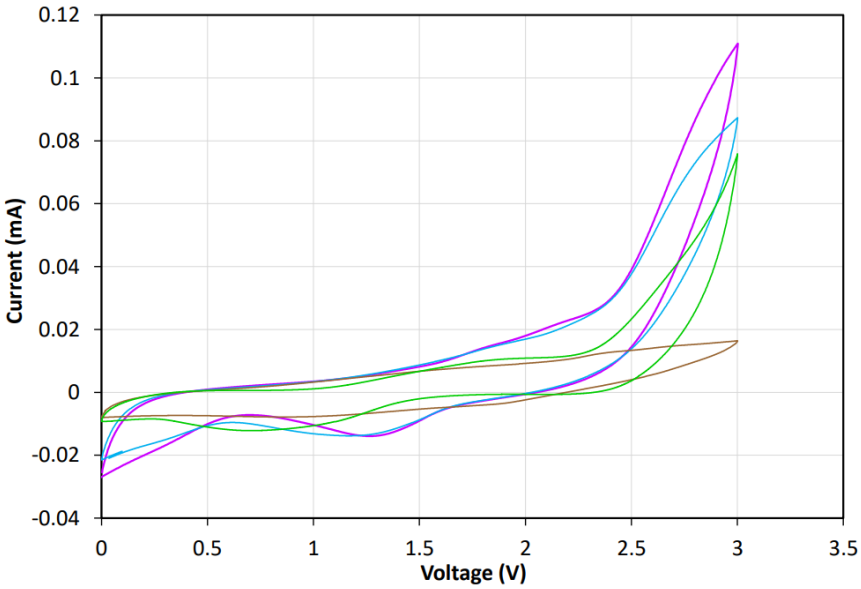

Figure 2.26: Cyclic voltammetry results of each electrolyte tested, coin cell system: 5^{th} cycle of the voltage range 0-3 V, scan rate of 5 mV/s: 1 M $LiPF_6$ in (1:1 vol.%) EC:DEC (brown), GPE (green), water-in-salt electrolyte (violet) and water-in-bisalt electrolyte (blue).

CHAPTER 3

Half-cell characterisation

3.1 Introduction

To characterise the electrochemical performances of the electrode materials separately, so-called "half-cell configurations" are assembled and subjected to various tests. Two main half-cell configurations are depicted in the literature: the two-electrode system and the three-electrode system. Both of these systems can be observed in Figure 3.1 [61][62].

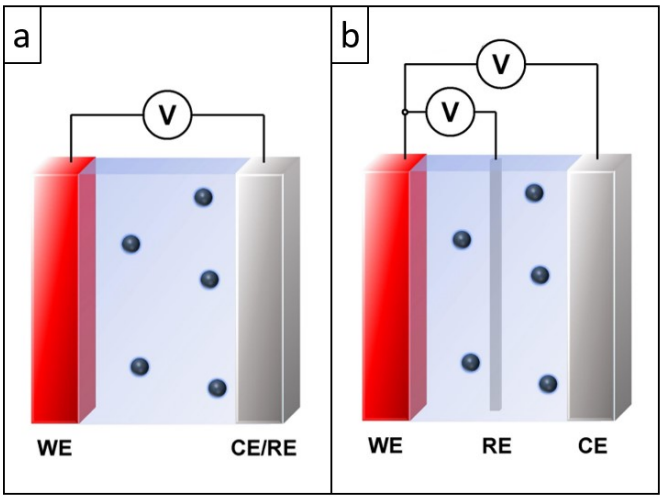

Figure 3.1: a) Two-electrode half-cell configuration, b) three-electrode half-cell configuration, modified from [63].

The two-electrode half-cell configuration is composed of the electrode of interest which is the working electrode (WE) and a counter electrode (CE) which also plays the role of the reference electrode (RE), as can be seen in Figure 3.1a. This type of system allows to focus on the working electrode by monitoring its potential *versus* the reference electrode. However, this monitoring is only possible at low current densities. Indeed, at high current densities, the polarisation effects associated to the counter electrode are too high and lead to a drop in the measured cell voltage. This leads to mistakes in the interpretation of the characterisation results because the potential of a reference electrode must be stable for good interpretation. A way to overcome this issue would be to use a three-electrode

half-cell configuration, shown in Figure 3.1b. In this configuration, the counter electrode and the reference electrode are distinct and the potentials of both the working and the counter electrodes can be monitored *versus* the reference electrode if needed [62].

In lithium-ion batteries, the half-cells assembled are most of the time two-electrode systems composed of the electrode of interest as working electrode and lithium metal as counter electrode and reference electrode. Lithium metal is a highly attractive counter electrode material due its extremely high specific capacity of 3860 mAh/g which represents a quasi unlimited source of lithium ions during the electrochemical characterisation measurements. This allows to focus on the characteristics of the working electrode, as the counter electrode will not be limiting in terms of capacity. In addition, lithium metal is an interesting reference electrode due to its stable potential at low current densities [61][62]. Despite the advantages of lithium metal, it must be kept in mind that some safety issues might occur when operating such cells, such as the formation of lithium dendrites which could ultimately lead to short-circuits [63]. It must be noted that the half-cell denomination is disputed in the literature concerning the use of lithium metal as counter electrode. Indeed, the cells assembled with an electrode material as working electrode and lithium metal as counter electrode are full working batteries, which are widely investigated in the literature as lithium metal batteries [62][64].

In this chapter, half-cells were assembled in two-electrode configuration, more precisely in coin cell configuration for the tests performed with the classical liquid electrolyte and the GPE. Concerning the water-in-salt electrolyte, half-cells were assembled in a three-electrode configuration, more precisely in a Swagelok T-cell configuration. The three-electrode configuration had to be used because the aqueous electrolyte could not be applied in two-electrode configuration with lithium metal as negative electrode. To characterise the electrode materials, two main measurement methods were applied. The first one was galvanostatic cycling, which consists in charging and discharging the cell at specified currents, while limiting the minimum and maximum voltages. This method allows to observe the electrochemical performances of the cell at different currents, which can be associated to different C-rates, as well as the cycling stability of the cell after multiple cycles [20]. The second method was cyclic voltammetry, which had been applied previously to investigate the electrolyte stability. When focusing on the electrodes, cyclic voltammetry allows to observe the oxidation and reduction peaks associated to the deinsertion and insertion of lithium ions within the electrode material when the voltage is increased and decreased at a specific scan rate. Cyclic voltammetry therefore gives information on the electrochemical reactions occurring during battery operation [65].

3.2 Experimental

3.2.1 Drop-casting of GPE on the electrodes

To study the electrochemical performances of half-cells containing GPE, GPE had to be drop-casted on the electrodes. The same casting method and drying step as Section 2.3.2.2 was applied. The GPE-casted electrodes can be observed in Figure 3.2. It must be noted

that 10 additional drops were added to the LFP electrodes because the GPE solution did not seem to spread completely to the sides of the electrodes, in comparison to the LTO electrodes.

Figure 3.2: GPE casted on the LFP (first row) and LTO (second row) electrodes by drop-casting.

Similarly to the GPE-casted current collectors, the electrodes were weighed before being transferred to the glovebox to determine the amount of GPE added. It was also seen that instead of having 40 mg/cm^2 on the electrodes, about 50 mg/cm^2 were obtained due to the error on the drop weighed before performing the casting. Two consequences of the higher mass can be expected. The first one is that the capacity of the cells assembled might be lower than expected due to the increased thickness of the GPE layer and the resulting decrease in ionic conductivity. The second consequence is that the increased thickness might reduce the risk of internal short-circuit, as more distance is put between both electrodes.

The electrodes were then transferred to the argon-filled glovebox and were ready to be assembled in half-cells.

3.2.2 Half-cell assembly: coin cell configuration

For the electrochemical characterisation of the electrodes, half-cells were assembled in coin cell configuration.

In the case of the 1 M $LiPF_6$ in (1:1 vol.%) EC:DEC electrolyte, the cells were assembled with lithium metal as negative electrode, 2 Celgard separators (16 mm diameter) soaked in 80 μL of electrolyte and LFP or LTO as the positive electrode.

Concerning the drop-casted GPE electrodes, the cells were assembled with lithium metal as negative electrode and GPE-covered LFP or LTO as positive electrode. No separator was required as GPE separates both electrodes. The quantity of GPE casted onto each electrode was 50 mg/cm^2. The electrodes had a diameter of 15.5 mm, which means that there was a total of 94 mg of GPE per battery.

In both cases, lithium metal was used as negative electrode and no additional reference electrode was introduced in the system. Therefore, the hypothesis that low current densities

would be applied and that the potential of the lithium metal reference would be stable at such currents was made.

3.2.3 Half-cell assembly: three-electrode configuration

To study the LFP electrodes with the water-in-salt electrolyte, lithium metal could not be used as negative electrode due to the aqueous base of the electrolyte. Therefore, the LFP electrodes were characterised against an activated carbon fabric electrode with an Ag^+/Ag reference in a three-electrode configuration. This experiment was performed at the Institute of Condensed Matter and Nanosciences of the University of Louvain.

To do so, new LFP electrodes had to first be produced using the water-based process depicted in Chapter 1, with different current collectors as the ones used previously. In this case, the current collector choice was restricted by the dimensions of the Swagelok T-cell and by the fact that the water-in-salt electrolyte is not compatible with aluminium current collectors. The three-electrode system had a diameter of 12.7 mm, in which the 15.5 mm diameter MTI stainless-steel current collectors did not fit. The current collectors used were 11 mm diameter stainless-steel 316 disks, visible in Figure 3.3a. Such a diameter was chosen to prevent short-circuits during cycling. A final LFP electrode obtained can be observed in Figure 3.3b. All of the LFP electrodes produced in this batch had an average active material mass of 3 mg.

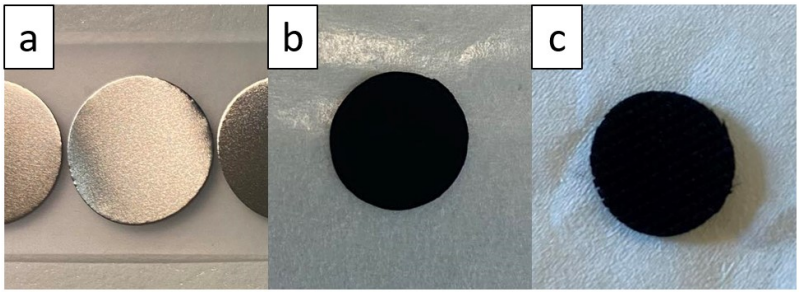

Figure 3.3: a) Stainless-steel 316 disks used for the three-electrode system, b) LFP-coated stainless-steel disks, c) Kynol activated carbon fabric used as negative electrode.

A three-electrode system could be assembled, similarly to the one depicted in Section 2.4.2.6. In this case, the working electrode was the LFP electrode, onto which a glass fiber separator was positioned. The reference electrode was still an Ag wire, positioned in between the separator which was on the LFP electrode and a separator used to isolate the reference from the negative electrode. The negative electrode was here composed of two activated carbon fabric disks of 12.7 mm diameter. The activated carbon fabric disks can be seen in Figure 3.3c and were made of Kynol activated carbon fabric (ACC-5092-20). The process associated to the activated carbon is a capacitive process and this type of material is used in the literature in electric double layer capacitors [66]. Two disks of carbon were superimposed to have enough surface for the adsorption of lithium ions during the charge and discharge of the half-cell.

3.2.4 Galvanostatic cycling characteristics: coin cell configuration

The coin cells were subjected to galvanostatic charge and discharge on MTI battery cyclers, which can be seen in Figure 3.4. The cells were kept in a thermostated chamber at 25°C.

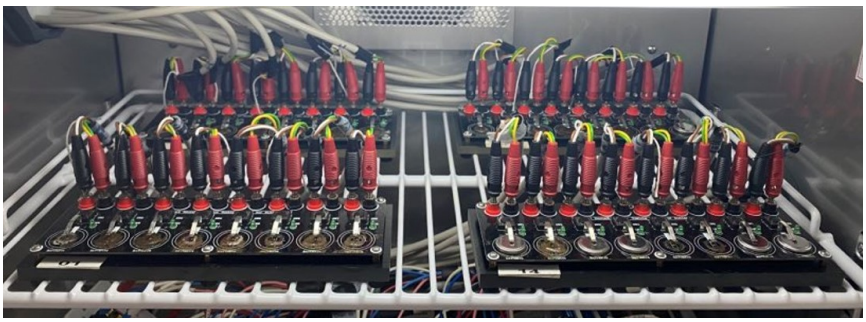

Figure 3.4: MTI battery cyclers.

The batteries were cycled at currents associated to different C-rates, corresponding to different charge and discharge times. The following equation was applied to determine the currents [29]:

$$I = \frac{Q}{t}m \tag{3.1}$$

where

- I is the current (mA) to apply to the cell and associated to a specific C-rate.
- Q is the theoretical capacity of the active material (mAh/g). The theoretical capacities of LTO and LFP are respectively 175 mAh/g and 170 mAh/g [23][26].
- t is the charge and discharge time (h) associated to the targeted C-rate.
- m is the mass of active material (g).

The cycling regime shown in Table 3.1 was applied to each half-cell in coin cell configuration.

Table 3.1: Galvanostatic cycling regime applied to half-cells in coin cell configuration.

	Formation (F)		Sequence 1 (S1)					Sequence 2 (S2)				
C-rate	C/5	C	C/5	C/2	C	2C	5C	C/5	C/2	C	2C	5C
Cycles	10	10	10	10	10	10	10	10	10	10	10	10

The currents associated to the C-rates were calculated using Equation 3.1. The coin cell was first let to rest for 30 min, so that the electrolyte could soak the material sufficiently

when it was in the liquid state. After the rest period, the first 20 cycles applied were considered to be formation cycles. The following cycles tested the cycling stability of the samples and were divided in two sequences. Galvanostatic cycling was performed between 1 and 2.5 V *vs.* Li^+/Li for the LTO half-cells and between 2 and 4.2 V *vs.* Li^+/Li for the LFP half-cells.

3.2.5 Galvanostatic cycling characteristics: three-electrode configuration

The three-electrode cell was subjected to a different cycling regime during galvanostatic cycling. The system studied, the LFP electrode against the Ag^+/Ag reference and the activated carbon negative electrode with the water-in-salt electrolyte, was more challenging than the previously studied systems. For this reason, a shorter cycling regime was applied because the objective was to first determine if the combination of materials and electrolyte was viable, that is to say if an insertion/deinsertion of lithium ions could happen.

First, the cell was let to rest for 5 h. A longer resting time was chosen for the three-electrode configuration because the viscous electrolyte needed time to soak all of the materials. After that, 20 cycles at a current associated to a C-rate of C/5 were performed. The currents were once again calculated with Equation 3.1. The cell was first cycled between -1 V and 1 V *vs.* Ag^+/Ag to observe the insertion/deinsertion plateau of LFP. The results showed the plateau around 0.5 V *vs.* Ag^+/Ag but the electrolyte was unstable during cycling because the voltage window studied was too large. Therefore, new cycling experiments were performed to decrease the width of the window applied. The final cycling tests were performed between 0.35 V and 0.7 V *vs.* Ag^+/Ag, and thus between 3.65 V and 4 V *vs.* Li^+/Li when the 3.3 V difference between the references was taken into account.

3.2.6 Cyclic voltammetry characteristics: coin cell configuration

Additional cyclic voltammetry tests were perfomed on half-cells in coin cell configuration to observe the oxidation and reduction peaks, corresponding to the deinsertion and insertion of the lithium ions. The tests were performed on LFP and LTO half-cells with the 1 M $LiPF_6$ in (1:1 vol.%) EC:DEC electrolyte and with the GPE.

Cyclic voltammetry was performed with the Biologic VMP3 mutlichannel potentiostat. It was performed between 1 and 2.5 V *vs.* Li^+/Li for the LTO half-cells and between 2 and 4.2 V *vs.* Li^+/Li for the LFP half-cells. Different scan rates were applied for each half-cell: 0.1 mV/s, 0.5 mV/s, 1 mV/s, 5 mV/s and 10 mV/s. Five cycles were performed for each scan rate.

3.3 Results and discussion

3.3.1 Cycling Results: 1 M $LiPF_6$ in (1:1 vol.%) EC:DEC

3.3.1.1 LTO electrodes

The galvanostatic cycling results for two LTO half-cell samples with the 1 M $LiPF_6$ in (1:1 vol.%) EC:DEC electrolyte can be observed in Figure 3.5.

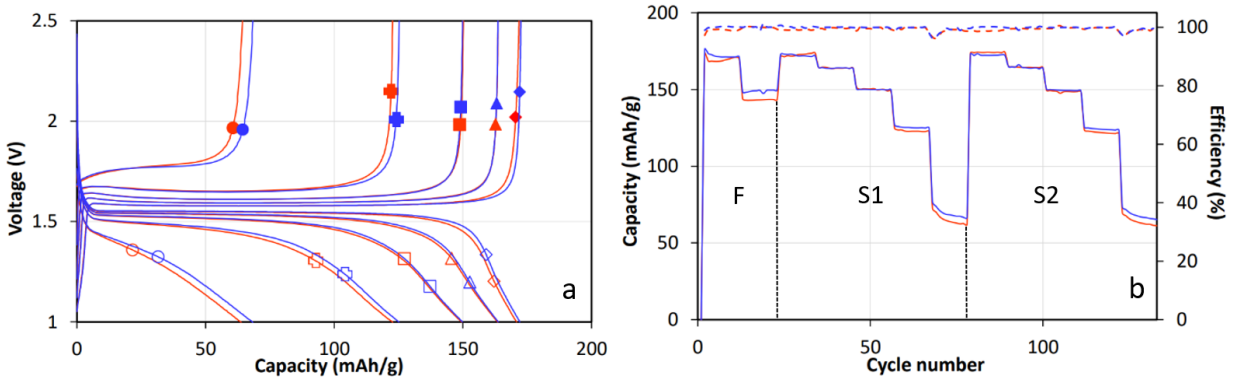

Figure 3.5: Results of galvanostatic charge and discharge for two LTO half-cell samples, LTO1 (red) and LTO2 (blue), with the 1 M $LiPF_6$ in (1:1 vol.%) EC:DEC electrolyte. a) Voltage profiles as a function of capacity at different C-rates during sequence 1. The 5^{th} cycle is shown for each C-rate. Charge: (◆) C/5, (▲) C/2, (■) C, (✚) 2C, (●) 5C. Discharge: (◇) C/5, (△) C/2, (□) C, (✚) 2C, (○) 5C. b) (——) Charge capacity upon cycling at different C-rates. (- - -) Coulombic efficiency upon cycling at different C-rates.

Figure 3.5a shows the voltage profiles as a function of the capacity for the 5^{th} cycle of each C-rate of sequence 1. A voltage plateau can be observed at about 1.55 V *vs.* Li^+/Li and corresponds to the insertion/deinsertion reaction of lithium ions in LTO. In addition, it can be seen that the gap between the charge and discharge curves is small at low C-rates, meaning that the electrochemical process is not so much affected by kinetic limitations. Those potential kinetic limitations can be associated to the movement of lithium ions and electrons. However, when the C-rate is increased, the movement of lithium ions through the electrolyte and electrode materials and the movement of electrons through the electrode materials are hindered. Therefore, the charges do not have the time to move and perform the insertion/deinsertion reaction correctly. The gap between the charge and discharge curves therefore increases as the C-rate is increased because the kinetic limitations become more and more significant [21][67]. It can also be seen that the voltage profiles are quite flat for moderate C-rates, which indicates that the capacity will be stored and delivered by the battery over a narrow potential window. This is desirable to obtain a battery which operates at constant voltage [21].

Figure 3.5b shows the evolution of the charge capacity during cycling at different C-rates as well as the evolution of the coulombic efficiency during cycling. It can be seen that the capacity drops as the C-rate is increased. This is expected as increasing the C-rate is

equivalent to increasing the speed at which the battery is charged and discharged, meaning that the lithium ions and electrons do not have the time to move and perform the reactions, as explained previously.

Concerning the coulombic efficiency, it varies between 96 and 101% during cycling at different C-rates. The coulombic efficiency can be defined as the ratio between the discharge capacity and charge capacity of a battery at a specific cycle. If the operation of the battery is not impacted by parasitic reactions, the charge and discharge capacities would stay the same during operation, meaning that the coulombic efficiency would remain at 100%. However, in practice, the battery is always affected by parasitic reactions which impact the value of the coulombic efficiency [68]. Examples of parastic reactions impacting the charge and discharge capacities of the battery and therefore the coulombic efficiency are the loss of lithium ions due to the formation of the SEI and the loss of lithium ions due to electrolyte instability [69]. In addition, leakage currents between the electrodes, which correspond to internal currents occurring within the battery [70], also impact the value of coulombic efficiency. In this case, the values of coulombic efficiency remain high, which indicates a good cycling behaviour of the batteries.

Table 3.2 focuses on the charge capacity of both samples for the 5^{th} cycle at different C-rates of sequence 1.

Table 3.2: Charge capacity of two LTO half-cell samples with the 1 M $LiPF_6$ in (1:1 vol.%) EC:DEC electrolyte during the first sequence at different C-rates from C/5 to 5C. The results for the 5^{th} cycle of each C-rate are shown.

Sample	Active material (mg)	Charge capacity (mAh/g)				
		C/5	C/2	C	2C	5C
LTO1	4.1	172	164	150	123	65
LTO2	4.1	173	164	150	125	69

It can be seen from Table 3.2 that after formation as well as 5 cycles at C/5, the capacity remains at about 98% of the theoretical capacity of LTO, which is 175 mAh/g. However, when cycling is performed at the highest C-rate, 5C, the charge capacity drops to 37-39% of the theoretical capacity.

Finally, it can be seen in Figure 3.5b that applying sequence 2 leads to similar results as sequence 1, meaning that a good cycling stability is observed. In addition, both samples behave similarly when subjected to cycling, which shows that there is a good reproducibility.

3.3.1.2 LFP electrodes

The galvanostatic cycling results for two LFP half-cell samples with the 1 M $LiPF_6$ in (1:1 vol.%) EC:DEC electrolyte can be observed in Figure 3.6. The results can be analysed

similarly to the results of the LTO electrodes.

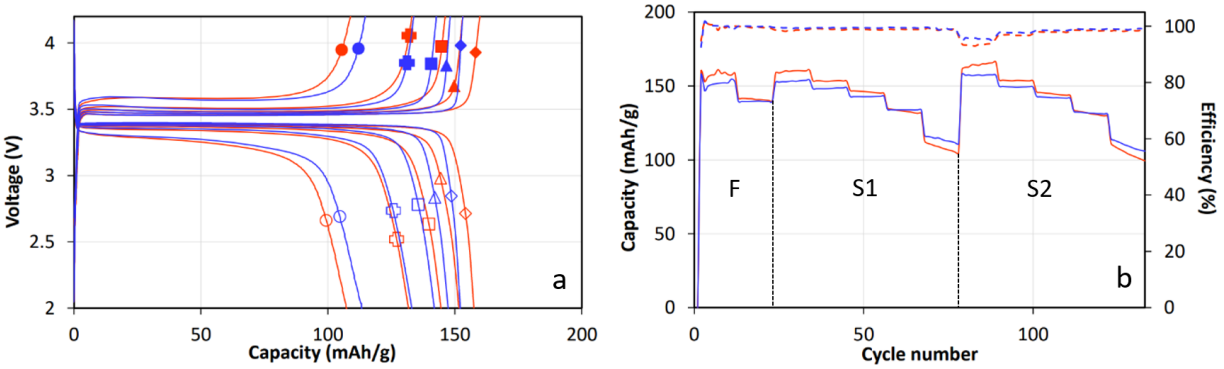

Figure 3.6: Results of galvanostatic charge and discharge for two LFP half-cell samples, LFP1 (red) and LFP2 (blue), with the 1 M $LiPF_6$ in (1:1 vol.%) EC:DEC electrolyte. a) Voltage profiles as a function of capacity at different C-rates during sequence 1. The 5^{th} cycle is shown for each C-rate. Charge: (◆) C/5, (▲) C/2, (■) C, (✚) 2C, (●) 5C. Discharge: (◇) C/5, (△) C/2, (□) C, (✚) 2C, (○) 5C. b) (——) Charge capacity upon cycling at different C-rates. (- - -) Coulombic efficiency upon cycling at different C-rates.

Figure 3.6a shows the voltage profiles as a function of the capacity for the 5^{th} cycle of each C-rate of sequence 1. Just as for LTO, a voltage plateau corresponding to the insertion/deinsertion of the lithium ions in LFP during cycling can be observed. This plateau occurs at about 3.45 V *vs.* Li^+/Li. When looking at the gap between the charge and discharge curves, it can once again be seen that it is small at low C-rates and that it increases due to kinetic limitations associated to the movement of charges when increasing C-rates are considered. In addition, the voltage profiles are in this case even flatter than for LTO, meaning that the batteries will be able to operate at a constant voltage.

Figure 3.6b shows the evolution of the charge capacity during cycling at different C-rates as well a the evolution of coulombic efficiency. It can be seen that the capacity drops as the cycling rate is increased. This drop is however less sharp than the drop observed in the case of LTO. The coulombic efficiency during cycling remains between about 93 and 101%.

Table 3.3 shows the charge capacity of both samples for the 5^{th} cycle at different C-rates of sequence 1.

Table 3.3: Charge capacity of two LFP half-cell samples with the 1 M $LiPF_6$ in (1:1 vol.%) EC:DEC electrolyte during the first sequence at different C-rates from C/5 to 5C. The results for the 5^{th} cycle of each C-rate are shown.

Sample	Active material (mg)	Charge capacity (mAh/g)				
		C/5	C/2	C	2C	5C
LFP1	3.8	160	153	146	133	109
LFP2	3.6	153	148	143	134	115

It can be seen from Table 3.3 that after formation and cycling during 5 cycles at C/5, the charge capacity remains at about 90-94% of the theoretical capacity, which is 170 mAh/g. When increasing the C-rate to 5C, the charge capacity decreases to about 64-68% of the theoretical capacity. This therefore means that in comparison to the performances of LTO, the LFP half-cells start with a capacity further away from the theoretical capacity but this capacity drops less sharply during cycling.

Finally, it can be seen by observing Figure 3.6b that the performances during sequence 2 seem to be better than sequence 1 for some of the C-rates applied.

3.3.2 Cyclic voltammetry results: 1 M $LiPF_6$ in (1:1 vol.%) EC:DEC

3.3.2.1 LTO electrodes

The cyclic voltammetry results of the LTO half-cell configuration with the 1 M $LiPF_6$ in (1:1 vol.%) EC:DEC electrolyte can be observed in Figure 3.7.

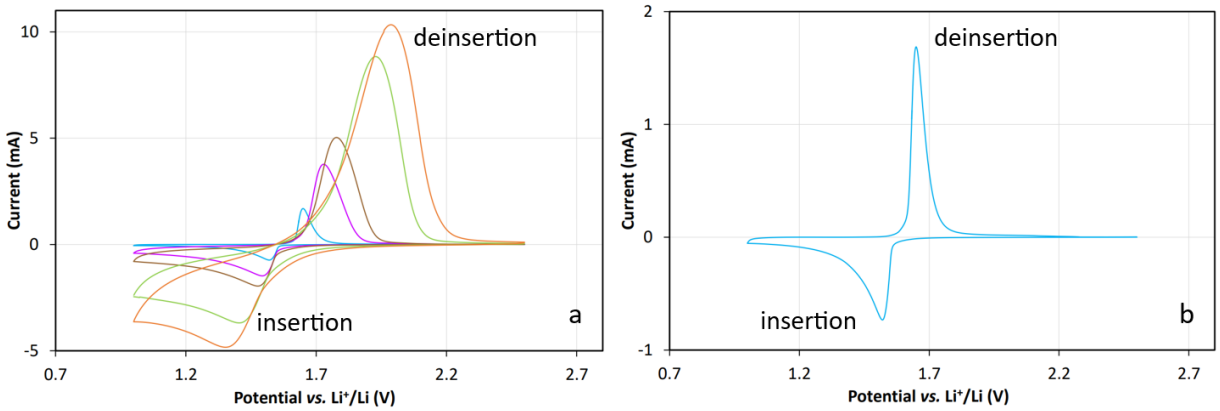

Figure 3.7: Cyclic voltammetry results of a LTO/Li half-cell sample with the 1 M $LiPF_6$ in (1:1 vol.%) EC:DEC electrolyte. a) Different scan rates were applied: 0.1 mV/s (blue), 0.5 mV/s (violet), 1 mV/s (brown), 5 mV/s (green), 10 mV/s (orange). The 5^{th} cycle is shown for each scan rate and corresponds to a stable cycle. b) Zoom on the 5^{th} cycle for the scan rate 0.1 mV/s (blue).

Figure 3.7a shows the most stable cycles at each scan rate applied while Figure 3.7b focuses on the smallest scan rate applied, 0.1 mV/s. Both Figures show the oxidation and reduction peaks. On the one hand, the oxidation corresponds to the positive current peak and the deinsertion of lithium ions from LTO. On the other hand, the reduction corresponds to the negative current peak and the insertion of lithium ions in LTO.

It can also be seen from Figure 3.7a that the oxidation and reduction peak potentials are dependent on the scan rate. Indeed, the oxidation peak potential increases and the reduction peak potential decreases with an increasing scan rate. When focusing on the results of the smallest scan rate in Figure 3.7b, it can be seen that the oxidation peak occurs at a potential of about 1.65 V *vs.* Li^+/Li and the reduction peak occurs at a potential of about 1.52 V *vs.* Li^+/Li, which is coherent with the plateau at 1.55 V *vs.*

Li^+/Li observed during galvanostatic cycling. When a scan rate of 10 mV/s is applied, the oxidation peak occurs at a potential of about 2 V *vs.* Li^+/Li and the reduction peak occurs at a potential of about 1.37 V *vs.* Li^+/Li. This dependence in scan rate can be explained by the fact that the insertion/deinsertion reaction of lithium ions in a composite electrode material is a quasi-reversible reaction. This quasi-reversible reaction is limited by the transfer of electrons and lithium ions and leads to a shift of the potentials when the scan rate is varied [65]. More simply, an increased scan rate does not leave the necessary time for electrons and ions to move and perform the insertion/deinsertion reaction completely. This can also explain that the reduction peak is less visible as the scan rate increases, because the insertion of lithium ions in LTO is hindered. This increase of scan rate could be compared to an increase in C-rate during galvanostatic cycling.

In addition, the absolute currents observed at the oxidation and reduction peaks also increase with the scan rate. This can be explained by the fact that the number of charges exchanged (in C) during the reactions can be computed by multiplying the current (in A, which corresponds to C/s) and the time (in s). Increasing the scan rate means decreasing the time during which the current is generated. To keep the number of charges exchanged constant, the current must therefore increase when the scan rate is increased [71].

Even if the movement of ions and electrons is difficult when increasing scan rates are considered, it can be seen that the oxidation and reduction peaks are still quite visible. This can be attributed to the liquid electrolyte, which has a high ionic conductivity and can conduct ions easily even if the scan rate is increased.

3.3.2.2 LFP electrodes

The cyclic voltammetry results of the LFP half-cell configuration with the 1 M $LiPF_6$ in (1:1 vol.%) EC:DEC electrolyte can be observed in Figure 3.8.

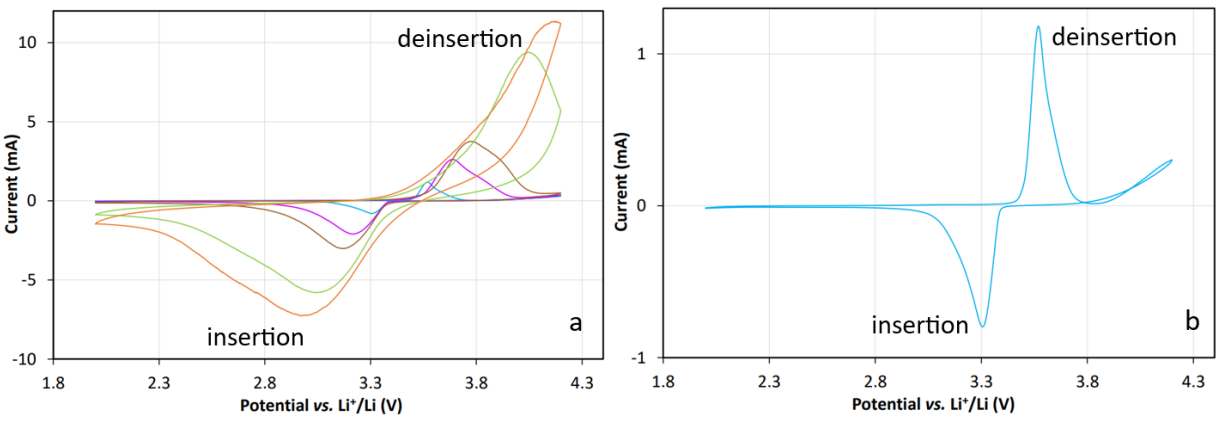

Figure 3.8: Cyclic voltammetry results of a LFP/Li half-cell sample, with the 1 M $LiPF_6$ in (1:1 vol.%) EC:DEC electrolyte. a) Different scan rates were applied: 0.1 mV/s (blue), 0.5 mV/s (violet), 1 mV/s (brown), 5 mV/s (green), 10 mV/s (orange). The 5^{th} cycle is shown for each scan rate and corresponds to a stable cycle. b) Zoom on the 5^{th} cycle for the scan rate 0.1 mV/s (blue).

The results shown in Figure 3.8 can be analysed similarly to Figure 3.7. From Figure 3.8b, it can be seen that the oxidation peak occurs at a potential of 3.57 V *vs.* Li^+/Li while the reduction peak occurs at a potential of 3.3 V *vs.* Li^+/Li, which is coherent with the voltage plateau observed at about 3.45 V *vs.* Li^+/Li during galvanostatic cycling.

Once again, an increasing scan rate leads to an absolute increase in the currents and the potentials at which oxidation and reduction occur. This can again be attributed to the quasi-reversibility of the reaction. The peaks associated to oxidation are less visible with an increasing scan rate, due to the difficulty of movement of ions and electrons. However, the liquid electrolyte has a high ionic conductivity, which counterbalances the effect of the scan rate and still allows to see oxidation and reduction peaks.

3.3.3 Cycling Results: GPE

3.3.3.1 LTO electrodes

The galvanostatic cycling results of two LTO half-cell samples with 50 mg/cm^2 of GPE on LTO, leading to a total of 94 mg of GPE in the battery, can be observed in Figure 3.9.

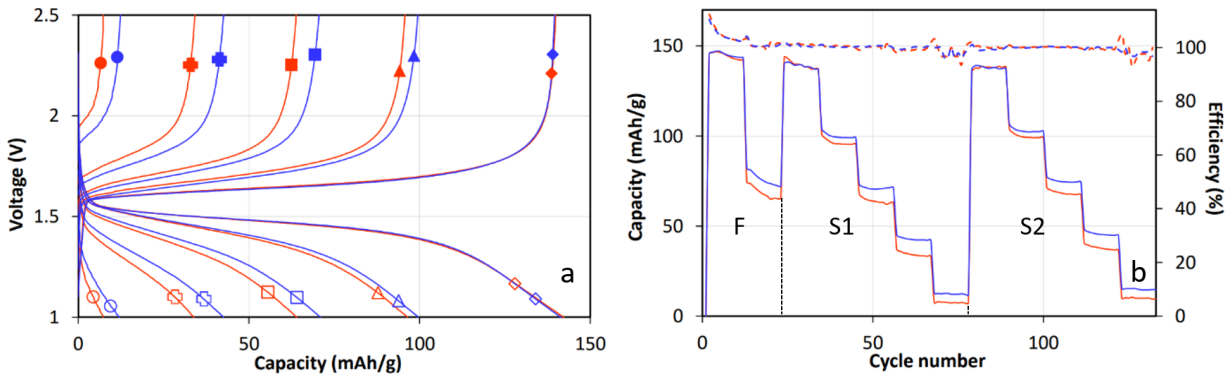

Figure 3.9: Results of galvanostatic charge and discharge for two LTO-GPE half-cell samples, LTO-GPE1 (red) and LTO-GPE2 (blue). a) Voltage profiles as a function of capacity at different C-rates during sequence 1. The 5th cycle is shown for each C-rate. Charge: (◆) C/5, (▲) C/2, (■) C, (✚) 2C, (●) 5C. Discharge: (◇) C/5, (△) C/2, (□) C, (✚) 2C, (○) 5C. b) (——) Charge capacity upon cycling at different C-rates. (- - -) Coulombic efficiency upon cycling at different C-rates.

Figure 3.9a shows the voltage profiles as a function of the capacity for the 5th cycle of each C-rate tested in sequence 1. This graph shows a voltage plateau around 1.55 V *vs.* Li^+/Li, which corresponds to what had been obtained with the classical liquid electrolyte. However, it can be seen that the plateau is less flat than in the classical case due to the fact that the charge and discharge curves are more sloping. This sloping behaviour means that the capacity of the battery will not be delivered or stored at a constant voltage, which is undesirable for battery operations. In addition, it can be seen that there is an increasing gap between the charge and discharge curves at increasing C-rates. This increase of the gap is even bigger than for the tests performed with the classical liquid electrolyte and

can once again be explained by kinetic limitations of the insertion/deinsertion reaction of lithium ions at higher C-rates.

Figure 3.9b shows the evolution of the charge capacity during cycling at different C-rates and the evolution of the coulombic efficiency during the application of the different cycling regimes. It can be observed that the capacity drops as the C-rate is increased, as expected. However, this drop is sharper than for the tests performed with the classical liquid electrolyte, meaning that the insertion/deinsertion of lithium ions becomes more and more difficult as the C-rate is increased for the GPE. This can be explained by the fact that the ionic conduction of the GPE is smaller than for the classical liquid electrolyte. This is due to the fact that the lithium ions have to pass through the semi-solid electrolyte rather than a completely liquid one and their movement is therefore even more hindered at a high C-rate than in the case of the classical liquid electrolyte.

When looking at the coulombic efficiency, it can be seen that it varies between 93 and 112% during cycling at different C-rates. The value of 112%, which is observed during the first cycles of battery, probably indicates the presence of leakage currents within the battery.

Table 3.4 shows numerical values of the charge capacity of both samples for the 5^{th} cycle at different C-rates of sequence 1.

Table 3.4: Charge capacity of LTO-GPE half-cells during the first sequence at different C-rates from C/5 to 5C. The results for the 5^{th} cycle of each C-rate are shown.

Sample	Active material (mg)	Charge capacity (mAh/g)				
		C/5	C/2	C	2C	5C
LTO-GPE1	2.7	140	96	64	34	8
LTO-GPE2	2.6	140	99	71	43	13

It can be observed from Table 3.4 that after the formation and the first 5 cycles at C/5, the capacity remains at 80% of the theoretical capacity of LTO. When higher C-rates are considered, for example 5C, the capacity drops to 5-7% of the theoretical capacity. This really shows that the capacity losses are higher when using the GPE due to the more difficult movement of lithium ions.

Finally, when observing sequence 2 in Figure 3.9b, it can be seen that no further losses occur and that the results are similar to sequence 1. This means that there is a good cycling stability, even if the obtained capacities are lower than for the liquid electrolyte. Finally, both samples show similar performances, which indicates a good reproducibility.

3.3.3.2 LFP electrodes

The galvanostatic cycling results of two LFP half-cell samples with 50 mg/cm^2 of GPE on LFP, leading to a total of 94 mg of GPE in the battery, can be observed in Figure 3.10.

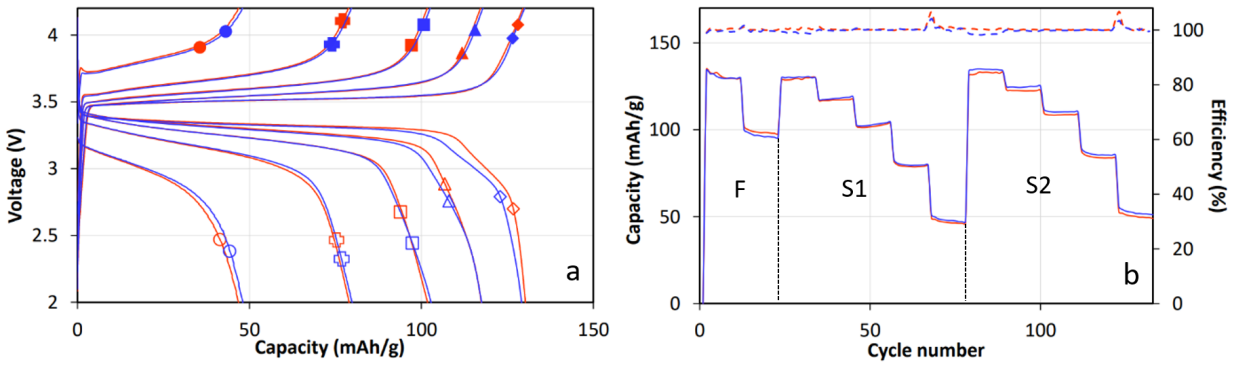

Figure 3.10: Results of galvanostatic charge and discharge for two LFP-GPE half-cell samples, LFP-GPE1 (red) and LFP-GPE2 (blue). a) Voltage profiles as a function of capacity at different C-rates during sequence 1. The 5th cycle is shown for each C-rate. Charge: (◆) C/5, (▲) C/2, (■) C, (✚) 2C, (●) 5C. Discharge: (◇) C/5, (△) C/2, (□) C, (✚) 2C, (○) 5C. b) (——) Charge capacity upon cycling at different C-rates. (- - -) Coulombic efficiency upon cycling at different C-rates.

When observing Figure 3.10a, which shows the voltage profiles as a function of the capacity for the 5 th cycle for each C-rate from sequence 1, it can be seen that a voltage plateau occurs around 3.45 V *vs.* Li^+/Li. This is similar to what had been obtained previously with the classical liquid electrolyte. However, the plateau is once again not flat, the curves are sloping and the gap between the charge and discharge curves increase with the C-rate, meaning that the voltage will not be constant during battery operation and that the operation at higher C-rates is impacted by kinetic limitations associated to the movement of charges.

The evolution of the capacity during cycling at different C-rates and the evolution of the coulombic efficiency can be observed in Figure 3.10b. It can once again be seen that the capacity drops, more sharply than for the LFP electrodes tested with the classical liquid electrolyte but less sharply than the LTO electrodes tested with the GPE. When focusing on the coulombic efficiency in Figure 3.10b, it can be observed that it varies between 99 and 106%. The value of 106% can once again probably be associated to the presence of leakage currents.

Table 3.5 shows the charge capacity of both samples for the 5th cycle at different C-rates of sequence 1.

Table 3.5: Charge capacity of LFP-GPE half-cells during the first sequence at different C-rates from C/5 to 5C. The results for the 5th cycle of each C-rate are shown.

Sample	Active material (mg)	Charge capacity (mAh/g)				
		C/5	C/2	C	2C	5C
LFP-GPE1	2.9	130	117	102	79	47
LFP-GPE2	2.8	130	118	103	80	48

It can be seen from Table 3.5 that after the formation and the 5 cycles at C/5, the capacity remains at 76% of the theoretical capacity, which is lower than in the case of the LTO electrode tested with the GPE. When applying higher C-rates, such as 5C, it can be observed that the capacity drops to around 28% of the capacity, which is much higher than what was obtained with the LTO electrode with GPE.

In addition, sequences 1 and 2 show similar results, meaning that there is a good cycling stability. Finally, the results obtained for both samples are very similar, which means that there is a good reproducibility.

3.3.4 Cyclic voltammetry results: GPE

3.3.4.1 LTO electrodes

The results of cyclic voltammetry for one LTO-GPE sample can be observed in Figure 3.11.

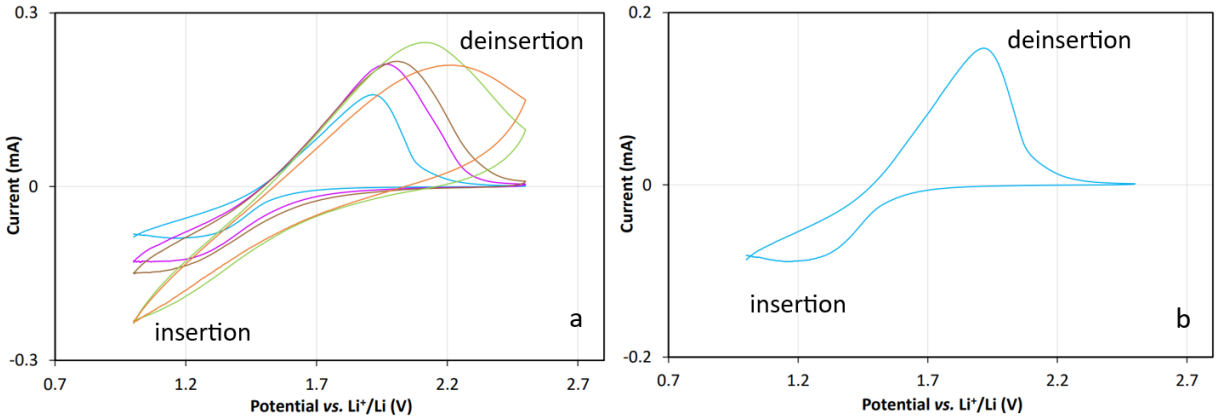

Figure 3.11: Cyclic voltammetry results of a LTO/Li GPE half-cell sample. a) Different scan rates were applied: 0.1 mV/s (blue), 0.5 mV/s (violet), 1 mV/s (brown), 5 mV/s (green), 10 mV/s (orange). The 5^{th} cycle is shown for each scan rate and corresponds to a stable cycle. b) Zoom on the 5^{th} cycle for the scan rate 0.1 mV/s (blue).

Figure 3.11a shows the most stable cycles for each scan rate applied during cyclic voltammetry while Figure 3.11 focuses on the smallest scan rate 0.1 mV/s.

It can be seen from Figure 3.11a that the oxidation peaks can be observed but are very wide and that the reduction peaks are hardly visible. This can be explained by the fact that the movement of lithium ions is more difficult through the semi-solid GPE than through the liquid electrolyte. The scan rates applied in this case might be too fast to observe the movement of the ions through the GPE and a much lower scan rate could be useful to observe the insertion and deinsertion reactions correctly.

By analysing Figure 3.11b, it can be seen that the oxidation peak occurs at 1.92 V *vs.* Li^+/Li and it can be estimated that the reduction peak occurs around 1.2 V *vs.* Li^+/Li. This potential range contains the 1.55 V *vs.* Li^+/Li corresponding to the flat

charge/discharge plateau. However, the range obtained with Figure 3.11b is not precise enough. Moreover, the current intensities are much lower than in the case of the classical liquid electrolyte, which shows that the reactions are hindered and cannot occur completely.

3.3.4.2 LFP electrodes

The cyclic voltammetry results of a LFP-GPE sample can be observed in Figure 3.12.

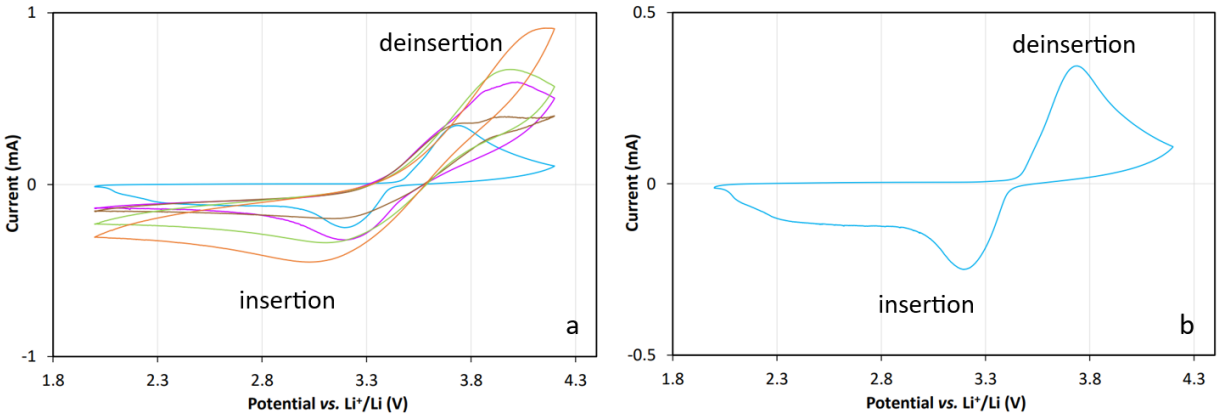

Figure 3.12: Cyclic voltammetry results of a LFP/Li GPE half-cell sample. a) Different scan rates were applied: 0.1 mV/s (blue), 0.5 mV/s (violet), 1 mV/s (brown), 5 mV/s (green), 10 mV/s (orange). The 5^{th} cycle is shown for each scan rate and corresponds to a stable cycle. b) Zoom on the 5^{th} cycle for the scan rate 0.1 mV/s (blue).

Figures 3.12a and 3.12b can be studied in the same way as Figures 3.11a and 3.11b.

From Figure 3.12a, it can once again be seen that the oxidation and reduction peaks are not clearly visible for the different scan rates. This allows to conclude once again that the scan rates applied are too fast and that the insertion and deinsertion reactions cannot occur to their full extent.

By looking at Figure 3.12b, it can be observed that in this case both the oxidation and reduction peaks can be seen. However, the peaks are wide and the currents generated are low. This can be explained by the hindered movement of lithium ions within the GPE.

In addition, the oxidation peak can observed at a potential of 3.75 V *vs.* Li^+/Li and the reduction peak can be seen at a potential of 3.21 V *vs.* Li^+/Li. This potential range contains the plateau at 3.45 V *vs.* Li^+/Li observed in galvanostatic cycling. However, the potential range is once again too wide and applying a lower scan rate could allow to obtain more precise results.

3.3.5 Cycling results: Water-in-salt electrolyte

The galvanostatic cycling results of the three-electrode system containing the LFP positive electrode, the Ag^+/Ag reference, the activated carbon negative electrode and the water-in-

salt electrolyte can be observed in Figure 3.13. The Figure only shows the five first cycles performed at C/5. The results for the 20 cycles can be found in the Appendices.

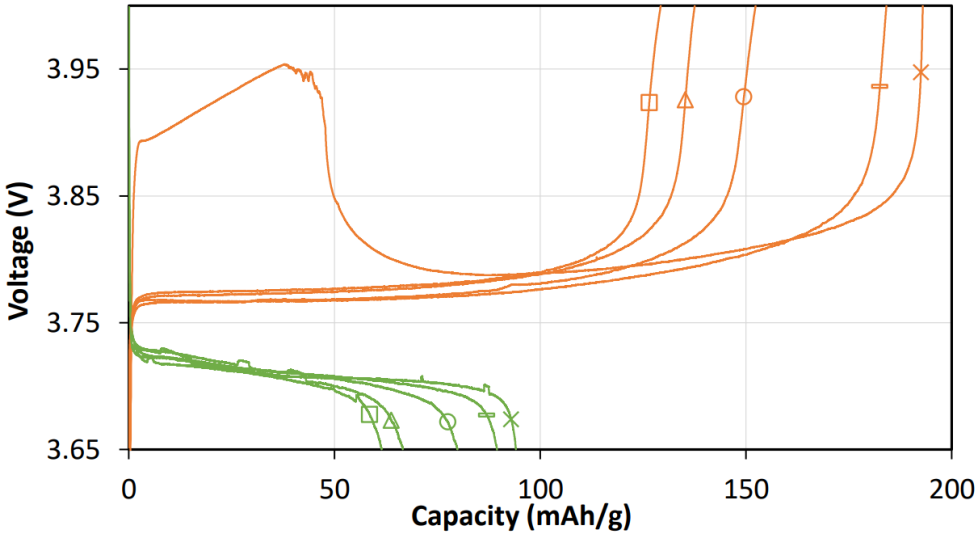

Figure 3.13: Results of galvanostatic charge and discharge for the three-electrode system containing the LFP electrode, the Ag^+/Ag reference, the activated carbon negative electrode and the water-in-salt electrolyte. Voltage profiles as a function of capacity at a C-rate of C/5. The charge and discharge profiles are respectively in orange and green. First cycle: (×). Second cycle: (▭). Third cycle: (○). Fourth cycle: (△). Fifth cycle: (□).

By analysing Figure 3.13, a first observation can be made concerning the voltage plateau. Previously, the voltage plateau concerning LFP occurred at 3.45 V *vs.* Li^+/Li for the test performed with a lithium metal negative electrode. In this case it can be seen that the plateau occurs around 3.75 V *vs.* Li^+/Li. This shift of 30 mV has two potential explanations. The first explanation is that the electrolyte is highly concentrated and might have impacted the voltage at which the plateau occurs. The second explanation is that the reference used in this case, Ag^+/Ag, might not be stable at the cycling conditions applied and led to a shift in the voltage measured.

To continue, it can be observed that the first charge performed has a voltage peak around 40 mAh/g. The voltage then decreases and the voltage profile goes back to an expected behaviour. This peak can be explained by the fact that it was the very first charge performed on the battery and that it is not unusual to observe surprising behaviours during the first charges and discharges of a battery. This behaviour can probably be associated to a degradation of the electrolyte. That is why formation cycles are performed industrially, so that the material can settle and the electrochemical behaviour of the battery can stabilise.

The capacity obtained at the first charge is around 192 mAh/g. This value is higher than the theoretical capacity of LFP, 170 mAh/g. However, the mass of active material considered can explain this issue. Indeed, an average mass of 3 mg was taken into account

but it is possible that the electrode tested in this cycling experiment had a slightly higher mass. This led to an overestimation of the capacity per gram.

When focusing on the evolution of the capacity with the cycles performed, it can be seen that the discharge capacity is always lower than the charge capacity and that both capacities decrease as numerous cycles are performed. This is confirmed when looking at the results for the 20 cycles performed available in the Appendices. This loss of capacity can probably be associated to the loss of mobile lithium ions from the electrolyte due to a lack of stability of the aqueous electrolyte. Even if the voltages tested are within the stability window measured through cyclic voltammetry, the water molecules free of salt within the water-in-salt electrolyte might have decomposed. Indeed, the water-in-salt electrolyte is almost saturated in salt but it is impossible to be sure that all the water molecules are used for salt solvation. Through the different cycles performed, this free water might have decomposed into H_2, OH^-, O_2, H^+ and electrons through the hydrogen and oxygen evolution reactions. In addition, it might be possible that the lithium ions within the water-in-salt electrolyte have reacted with the OH^-, leading to the formation of LiOH. The result of the electrolyte instability can therefore be twofold: the medium through which lithium ions travel was decomposed and the quantity of lithium ions was decreased through the reaction with the products from water decomposition.

An additional hypothesis for the capacity loss could be the incompatibility of the electrodes with the electrolyte. Indeed, the LFP electrodes are composed of a water-soluble binder. The stability of the LFP electrode has been studied by immersing the electrode in the electrolyte and no visible deterioration could be observed. However, the binder could possibly not be stable during cycling and the electrode material could slowly deteriorate and lead to a capacity loss. Therefore, the xanthan gum binder should also be further investigated.

3.4 Conclusion and perspectives

Half-cells composed of the different electrolytes and electrodes have been subjected to galvanostatic cycling and cyclic voltammetry.

The results concerning the classical liquid electrolyte, 1 M $LiPF_6$ in (1:1 vol.%) EC:DEC, show good capacities and good cycling stability of both the LFP and LTO electrodes. The voltage plateaus are flat, leading to battery operations at constant voltage. In addition, the gaps between the voltage profiles are reasonable at moderate C-rates. This means that the ionic conductivity of the electrolyte is quite good and that the performances at moderate C-rates are not hindered by kinetic limitations of lithium ion diffusion. This electrolyte is the most commercially used type of electrolyte and the results obtained with this study therefore represent the target performances for the other less conventional electrolytes.

Concerning the GPE, it was observed that lower capacities are obtained in comparison to the classical liquid electrolyte. Moreover, the voltage profiles are less flat, even at moderate C-rates. This means that the battery will deliver or store its capacity at a variable voltage, which is not desirable for commercial battery operation. In addition, the capacities drop

more sharply and the gaps between the charge and discharge profiles increase faster than for the classical liquid electrolyte when the C-rate is increased. Those issues can most probably be attributed to the lower ionic conductivity of the GPE due to its semi-solid state which hinders the movement of the lithium ions in comparison to their movement in the liquid state electrolyte. In addition, the thickness of the GPE layer might also impact negatively the performances of the battery by increasing the path of the lithium ions between the electrodes. A last issue which might be pointed out is the connection between the electrolyte and the electrode material. It is not known how deep the GPE enters the electrode material during the casting process and the connections between the electrolyte and the material might not be optimal.

To improve the electrochemical performances of the GPE, different possibilities could be considered:

- The quantity of GPE casted on the electrode could be decreased. Indeed, the first tests were performed with 50 mg/cm^2 of electrolyte on the electrode but it is known from the literature that a quantity of 40 mg/cm^2 might be more appropriate [49]. Decreasing the electrolyte quantity could allow to decrease the thickness of the electrolyte layer and therefore facilitate the movement of lithium ions from one electrode to the other. The capacities obtained during cycling could therefore be increased. However, an issue might occur if the layer is not thick enough. Indeed, by decreasing the thickness, both electrodes would be closer within the battery and the risks of internal short-circuits would be increased.
- The GPE could be casted on the electrode simultaneously to the spraying of the electrode material on the current collector. More precisely, the electrode material could for example be sprayed in 5 different steps. The total active mass targeted on the electrode would be divided by 5 to know exactly the ink volume which must be sprayed at each step. In between the spraying steps, a specific quantity of GPE would be casted on the electrode. This quantity would be calculated based on the electrode void fraction determined in Chapter 1. The GPE quantity determined would allow to fill completely the void fraction of the material at each casting step, without forming an insulating layer of electrolyte in between two layers of electrode material. Once this process is over, a thin layer of GPE would be casted on the final electrode to separate the positive and negative electrodes in the assembled batteries. The thickness of this layer would have to be optimised to be as thin as possible while avoiding internal short-circuits. It is expected that this method of casting the GPE would enhance the contacts between the electrode material and the electrolyte and therefore lead to a better ionic conductivity. However, this method is complex, especially concerning the casting of the electrolyte, the quantity of which must be precisely determined to avoid the formation of an insulating layer and the associated loss of capacity.
- To enhance the contacts between the electrode material and the GPE, part of the solution of GPE could be mixed with the ink of active material before spraying. The resulting mixture could then be sprayed on the current collectors. This would result in a composite electrode containing a mix of active material, conducting carbon, binder

and GPE. A thin layer of GPE would once again be casted on top of the electrode to separate one electrode from the other in the battery. This technique could hopefully enhance the contacts and therefore increase the ionic conductivity and the capacities obtained during cycling. However it should first be verified that the mix of the ink and the GPE solution does not change the overall chemistry of the final electrode material and does not lead to issues during the spraying process.

Concerning the water-in-salt electrolyte, the results showed that the cycling is not stable and that the capacity is lost very quickly. This loss can probably be associated to a lack of stability of the electrolyte, even if the voltages applied are within the stability window. This therefore implies that the stability of the electrolyte has to be further investigated and improved before such type of electrolyte can be used in lithium-ion batteries. In addition, the compatibility of the binder with the electrolyte during cycling should be further studied.

The electrodes have been characterised in half-cell configuration with the different electrolytes. The next chapter focuses on the electrochemical characterisation of the electrodes and electrolytes in full-cell configuration.

CHAPTER 4

Full-cell characterisation

4.1 Introduction

After having characterised the electrode materials separately in half-cell configuration, full-cells can be assembled to study the behaviour of the materials jointly. Two main full-cell configurations are depicted in the literature: the two-electrode system and the three-electrode system. Both of theses systems can be observed in Figure 4.1 [61][62].

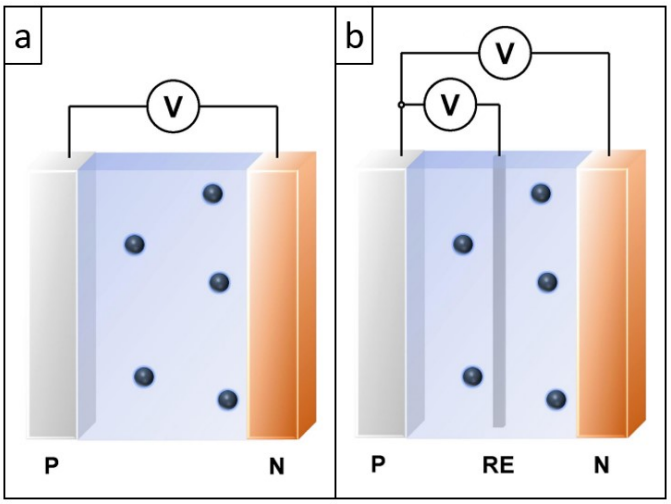

Figure 4.1: a) Two-electrode full-cell configuration, b) three-electrode full-cell configuration, modified from [63].

The two-electrode full-cell configuration is composed of both of the electrodes of interest, the positive electrode (P) and the negative electrode (N), as can be seen in Figure 4.1a. The terms working electrode and counter electrode are more specific for the half-cell configuration and are less used for full-cell configuration. The two-electrode full-cell system is operated by monitoring the cell voltage, which is the difference between the potentials of both electrodes. If it is of crucial importance to monitor the potential of each electrode, then a three-electrode system, shown in Figure 4.1b, is the most suitable configuration. This system contains a reference electrode, which has a stable potential, in between the positive and negative electrodes [62].

As explained in Chapter 1, the positive and negative electrodes in a full-cell must have balanced capacities. Indeed, the objective is to have similar capacities on both electrodes in order not to waste valuable material in dead capacity. However, it is known that negative electrodes are usually produced with an excess capacity in comparison to positive electrodes. The main reason for that is to prevent lithium plating on the negative electrode. The positive electrode is therefore the limiting electrode of the full-cell [28][61].

In this chapter, full-cells were assembled in two-electrode configuration, more precisely in coin cell configuration, for all of the electrolytes tested. The main electrochemical characterisation methods applied were once again galvanostatic cycling and cyclic voltammetry.

4.2 Experimental

4.2.1 Drop-casting of GPE on the electrodes

To study the electrochemical performances of full-cells with GPE, GPE had to be casted on the electrodes. In the case of full-cells, the casting was performed with a micropipette to avoid the error on the masses of GPE observed in Sections 2.3.2.2 and 3.2.1. The drying step applied was unchanged.

A volume of 40 μL of GPE solution was dried and weighed. This volume corresponded to 4.4 mg of dried GPE and this result could be used to determine the number of 40 μL volumes to be added on the electrodes based on the target GPE mass.

For the first cycling tests of full-cells with GPE, it was decided to target 50 mg/cm^2 per electrode, which was similar to what was obtained for the electrodes used in half-cells. However, it was expected that a mass of 50 mg/cm^2 of GPE per electrode would be too high. Indeed two electrodes were used per full cell and led to a total GPE amount of 188 mg per cell. It was expected that this high quantity would lead to a decrease in cell capacity due to the high thickness and the reduced ionic conductivity of the electrolyte.

For the second cycling tests of full-cells with GPE, new electrodes were therefore drop-casted with a lower mass of GPE. Moreover, different configurations were analysed, based on the mass repartition of GPE between the positive and negative electrodes. Theses configurations can be seen in Table 4.1.

Table 4.1: GPE masses drop-casted for the second cycling tests of the full-cell configuration.

Number of full-cells	GPE mass on LTO (mg/cm^2)	GPE mass on LFP (mg/cm^2)
2	40	10
2	10	40
2	25	25

4.2.2 Full-cell assembly

For the electrochemical characterisation of both electrodes, full-cells were assembled in coin cell configuration.

In the case of the 1 M $LiPF_6$ in (1:1 vol.%) EC:DEC electrolyte, the cells were assembled with LFP as positive electrode, LTO as negative electrode and 2 Celgard separators (16 mm diameter) soaked in 80 μL of electrolyte.

Concerning the drop-casted GPE electrodes, the cells were assembled with GPE-covered LFP as positive electrode and GPE-covered LTO as negative electrode. No separator was required as the GPE electrolyte separates both electrodes. Different types of full-cells were assembled based on the quantity of GPE casted on the electrodes. The following masses of GPE were considered: 50 mg/cm^2 on both LTO and LFP, 40 mg/cm^2 on LTO and 10 mg/cm^2 on LFP, 10 mg/cm^2 on LTO and 40 mg/cm^2 on LFP, and 25 mg/cm^2 on LTO and 25 mg/cm^2 on LFP.

Finally, concerning the water-in-salt electrolyte, the cells were assembled with LFP as positive electrode, LTO as negative electrode and 2 Celgard separators (16 mm diameter) soaked in 160 μL of electrolyte. It must be noted that the full-cells containing WIS electrolyte had to be assembled out of the glovebox, due to the aqueous base of the electrolyte. No argon bubbling of the electrolyte was considered in this case.

4.2.3 Cycling characteristics

The assembled coin cells were subjected to galvanostatic charge and discharge on MTI battery cyclers. The cells were kept in a thermostated chamber at 25°C.

The batteries were cycled at currents associated to specific C-rates, corresponding to different charge and discharge times. The currents applied were calculated in the following way. First, the capacity of each electrode, LFP and LTO, was calculated using Equation 4.1 [29]:

$$\mathrm{C} = \mathrm{Q.m} \tag{4.1}$$

where

- C is the capacity of the electrode (mAh).
- Q is the theoretical capacity of the active material (mAh/g). The theoretical capacities of LTO and LFP are respectively 175 mAh/g and 170 mAh/g [23][26].
- m is the mass of active material (g).

The current could then be calculated using Equation 4.2:

$$\mathrm{I} = \frac{1}{\mathrm{t}} \frac{1}{\frac{1}{\mathrm{C_{LTO}}} + \frac{1}{\mathrm{C_{LFP}}}} \tag{4.2}$$

where

- I is the current (mA) to apply to the cell and associated to a specific C-rate.

- t is the charge and discharge time (h) associated to the targeted C-rate.
- C_{LTO} is the capacity of the LTO electrode (mAh).
- C_{LFP} is the capacity of the LFP electrode (mAh).

The cycling regime shown in Table 4.2 was applied to each full-cell.

Table 4.2: Galvanostatic cycling regime applied to full-cells.

	Formation (F)	Sequence 1 (S1)	Sequence 2 (S2)						Sequence 3 (S3)
C-rate	C/5	C	C/5	C/2	C	2C	5C	10C	C/5
Cycles	20	100	10	10	10	10	10	10	10

The currents associated to the different C-rates were calculated based on Equations 4.1 and 4.2. The galvanostatic cycling was performed between 1 and 2.5 V *vs.* Li^+/Li.

It must be noted that the graphs obtained through galavanostatic cycling are expressed in terms of the limiting electrode, which is LFP. Therefore, when the capacity is shown in a graph, it is expressed as mAh/g_{LFP}. For simplicity, the subscript LFP is not written in the Figures.

4.2.4 Cyclic voltammetry characteristics

Cyclic voltammetry was applied to full-cells to observe the insertion/deinsertion reactions taking place.

Cyclic voltammetry was performed with the Biologic VMP3 multichannel potentiostat, between 1 and 2.5 V *vs.* Li^+/Li.

For the full battery with the 1 M $LiPF_6$ in (1:1 vol.%) EC:DEC electrolyte, a scan rate of 1 mV/s was applied and 11 cycles were performed.

No cyclic voltammetry measurements were performed for the full battery with the GPE electrolyte due to time constraints.

For the full battery with the water-in-salt electrolyte, a scan rate of 1 mV/s was applied and 11 cycles were performed.

4.3 Results and discussion

4.3.1 Cycling Results: 1 M $LiPF_6$ in (1:1 vol.%) EC:DEC

The galvanostatic cycling results of two LFP/LTO full-cell samples with the 1 M $LiPF_6$ in (1:1 vol.%) EC:DEC electrolyte can be observed in Figure 4.2.

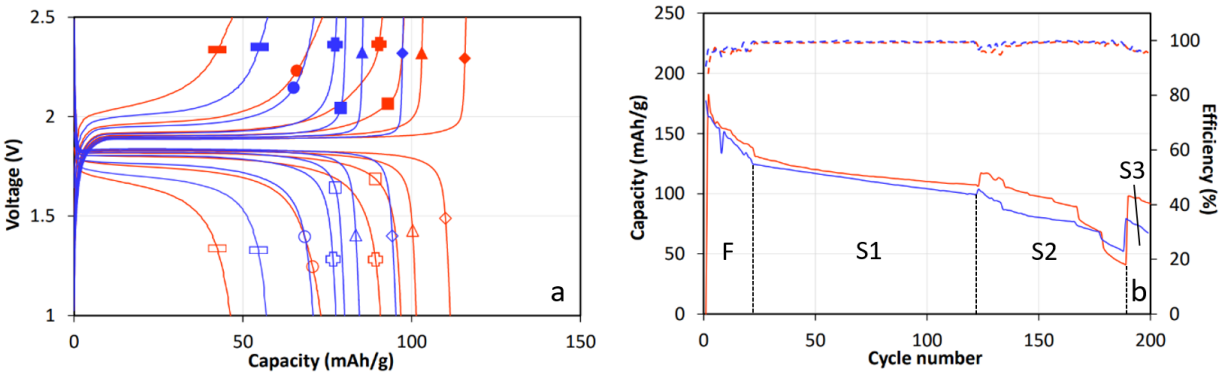

Figure 4.2: Results of galvanostatic charge and discharge for two LFP/LTO full-cell samples, LFP-LTO1 (red) and LFP-LTO2 (blue), with the 1 M $LiPF_6$ in (1:1 vol.%) EC:DEC electrolyte. The capacity is expressed in mAh/g_{LFP}. For simplicity, the subscript LFP is not written in the Figures. a) Voltage profiles as a function of capacity at different C-rates during sequence 2. The 5^{th} cycle is shown for each C-rate. Charge: (◆) C/5, (▲) C/2, (■) C, (⬟) 2C, (●) 5C, (▬) 10C. Discharge: (◇) C/5, (△) C/2, (□) C, (⬠) 2C, (○) 5C, (▭) 10C. b) (——) Charge capacity upon cycling at different C-rates. (- - -) Coulombic efficiency upon cycling at different C-rates.

Figure 4.2a shows the voltage profiles as a function of the capacity for the 5^{th} cycle of each C-rate of sequence 2. The voltage plateau corresponding to the insertion and deinsertion reactions in LFP and LTO can be observed at about 1.85 V. It can also be seen that the charge and discharge curves at moderate C-rates are very steep at the end of the curves, leading to very flat voltage profiles, which means that the battery will operate at a constant voltage. When higher C-rates are considered, the charge and discharge curves become more sloping and the gap between those curves increases due to kinetic limitations. Those kinetic limitations can once again be associated to the hindered movement of lithium ions through the electrolyte or through the electrode materials. The limitations can also be due to a limited movement of electrons within the electrode materials. This means that lower performances will be seen at higher C-rates and that a less constant voltage will be seen during operation.

Figure 4.2b represents the evolution of the charge capacity during cycling at various C-rates and the evolution of the coulombic efficiency.

During sequence 1, where 100 cycles at C are applied, it can be seen that the capacity drops from about 125 mAh/g to about 105 mAh/g. This drop can be explained by the repetition of the cycles, which affect the materials and lead to losses of capacity.

Sequence 2 allows to observe the behaviour of the battery at various C-rates. As expected, increasing C-rates lead to a decreasing capacity. Table 4.3 shows the numerical values of charge capacity associated to the 5^{th} cycle of each C-rate of this sequence and allows to see this drop more precisely.

Sequence 3 shows the application of a C-rate of C/5. It can be seen that the capacity obtained is lower than for the cycles at C/5 applied during sequence 2. Indeed, the capacity of the sample LFP-LTO1 goes from 116 mAh/g at the first cycle at C/5 of sequence 2 to 97

mAh/g at the first cycle at C/5 of sequence 3 while the capacity of the sample LFP-LTO2 goes from 102 mAh/g to 78 mAh/g at the same conditions. This shows that the cycling is less stable than in the case of the LFP and LTO half-cells studied, for which similar capacities were obtained when the sequences were repeated. However, this might be due to the high number of cycles tested in comparison to the half-cell samples. In addition, the cycling performed at high C-rates might have damaged the electrode materials and led to irreversible capacity losses.

Finally, when looking at the coulombic efficiency, it can be seen that it varies between 88 and 99% during the whole galavanostatic cycling experiment. The efficiencies obtained are lower than for the half-cells characterised in Chapter 3. This observation leads to the conclusion that full-cells are more affected by parasitic reactions during cycling and more losses of mobile lithium ions can be observed. The losses of lithium ions are less visible in half-cells than in full-cells due to the presence of the lithium metal negative electrode in half-cells. This lithium metal negative electrode represents a quasi-infinite source of lithium ions and therefore masks the potential losses of lithium ions through parasitic reactions.

Table 4.3: Charge capacity of LFP-LTO full-cells with the 1 M $LiPF_6$ in (1:1 vol.%) EC:DEC electrolyte during the second sequence at different C-rates from C/5 to 5C. The results for the 5^{th} cycle of each C-rate are shown.

Sample	Active material (mg)		Charge capacity (mAh/g)					
	LFP	LTO	C/5	C/2	C	2C	5C	10C
LFP-LTO1	2.8	3.5	116	103	98	91	74	47
LFP-LTO2	2.6	3.5	98	87	81	78	71	57

4.3.2 Cyclic voltammetry results: 1 M $LiPF_6$ in (1:1 vol.%) EC:DEC

The cyclic voltammetry results of a full LFP/LTO battery with the 1 M $LiPF_6$ in (1:1 vol.%) EC:DEC electrolyte can be seen in Figure 4.3. The Figure shows cycle 8, which corresponds to a stable cycle over the 11 cycles performed. All the cycles of Figure 4.3 are available in the Appendices.

The cyclic voltammetry results of Figure 4.3 show the oxidation and reduction peaks associated respectively to the charge and discharge of the battery. The oxidation peak, observed during the positive scan of voltage and linked to the positive current peak, can be associated to the deinsertion of lithium ions from LFP and the insertion of lithium ions within LTO. The reduction peak, observed during the negative scan of voltage and linked to the negative current peak, can be associated to the insertion of lithium ions within LFP and the deinsertion of lithium ions from LTO.

Those peaks occur respectively at around 2.06 V and 1.67 V. This range contains the 1.85 V voltage plateau, which is coherent. However, it can be seen that the peaks are quite

wide, meaning that the movement of lithium ions might be hindered due to a too high scan rate. To obtain more precise results, testing a lower scan rate would be of interest.

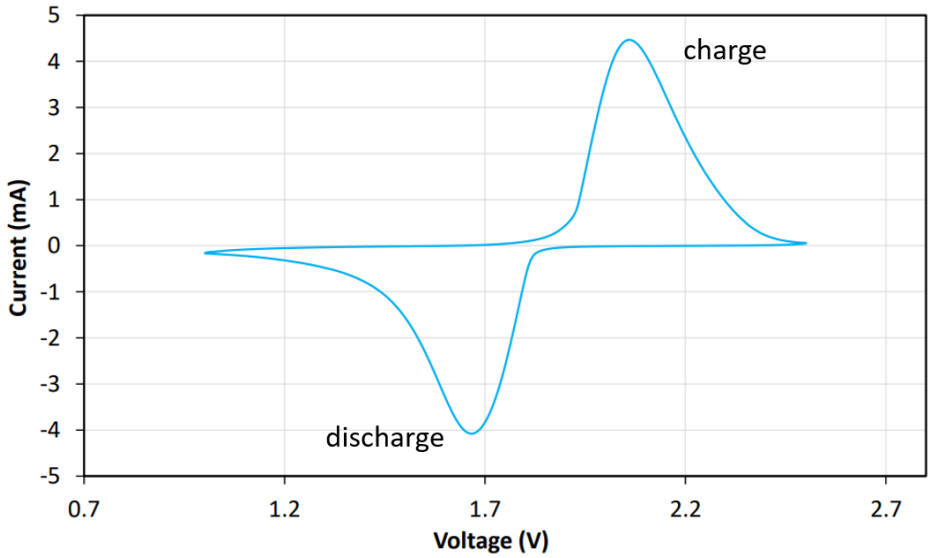

Figure 4.3: Cyclic voltammetry results of a LFP/LTO full-cell sample with the 1 M $LiPF_6$ in (1:1 vol.%) EC:DEC electrolyte. Cycle 8 is shown and corresponds to a stable cycle

4.3.3 Cycling Results: GPE

As a reminder, 4 different configurations were studied for the LFP/LTO batteries with GPE: 50 mg/cm^2 on both LTO and LFP, 40 mg/cm^2 on LTO and 10 mg/cm^2 on LFP, 10 mg/cm^2 on LTO and 40 mg/cm^2 on LFP, and 25 mg/cm^2 on LTO and 25 mg/cm^2 on LFP. The configuration 50 mg/cm^2 on both LTO and LFP leads to a total of 188 mg of GPE within the battery. The other three configurations lead to a total of 94 mg of GPE within the battery.

The results concerning the configuration 40 mg/cm^2 on LTO and 10 mg/cm^2 on LFP led to short-circuits and are not shown. Performing additional tests could allow to study this configuration in more details. However, it is expected that this configuration will behave similarly to the other configurations with a total GPE content of 94 mg.

4.3.3.1 First cycling tests performed: 50 mg/cm^2 on both LTO and LFP

The galvanostatic results concerning the configuration with 50 mg/cm^2 of GPE on both the LTO and LFP electrodes, which leads to a total of 188 mg of GPE in the battery, can be seen in Figure 4.4.

Figure 4.4a shows the voltage profiles as a function of capacity for the first and second charges and discharges of the battery. It can be observed that the first charge stops at a capacity of 159 mAh/g. The plateau obtained is sloping, meaning that the voltage obtained during battery operation will not be constant. In addition, when looking at the

first discharge, it can be seen that almost no capacity is recovered, which indicates an irreversible capacity loss of almost 100%. The second charge observed confirms this loss, as a capacity of 4.7 mAh/g is obtained and almost no capacity is recovered with the second discharge.

Figure 4.4b shows the evolution of the charge and discharge capacities in function of the cycles performed. This Figure confirms the fact that the capacity is lost very quickly.

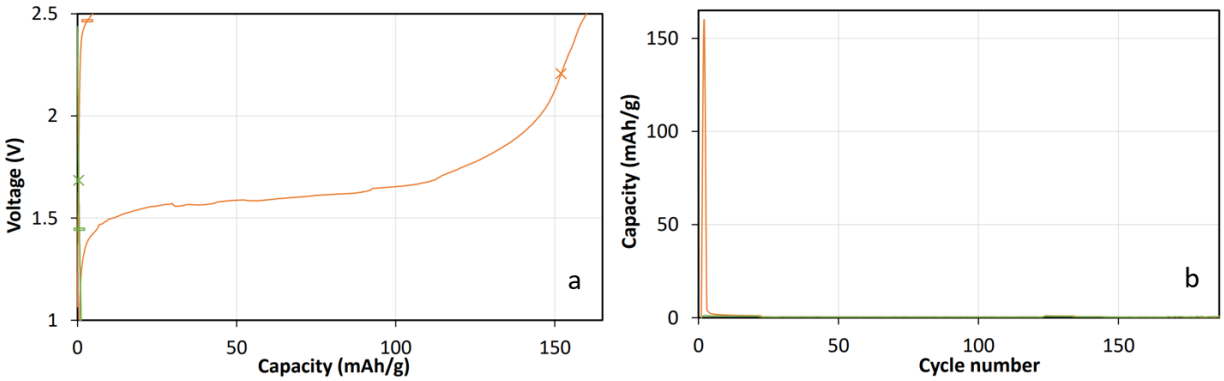

Figure 4.4: Results of galvanostatic charge and discharge for one LFP/LTO GPE full-cell sample with a total of 188 mg of GPE, evenly distributed among both electrodes. The capacity is expressed in mAh/g_{LFP}. For simplicity, the subscript LFP is not written in the Figures. a) Voltage profiles as a function of capacity at a C-rate of C/5. The charge and discharge profiles are respectively in orange and green. First cycle: (×). Second cycle: (▭). b) Orange line: Charge capacity upon cycling at different C-rates. Green line: Discharge capacity upon cycling at different C-rates.

The following reasons for this very high and rapid capacity loss can be discarded:

- The stability of the GPE should not be a problem, as this electrolyte was characterised in half-cell configuration for the LTO electrode between 1 and 2.5 V *vs.* Li^+/Li and for the LFP electrode between 2 V and 4.2 V *vs.* Li^+/Li and showed good performances in terms of cycling. It is therefore not expected that the GPE would be unstable in the case of full-cell configurations.
- The formation of lithium dendrites which could affect battery performances should not be an issue in full-cell configuration. Indeed, full-cell electrodes are composed of intercalation materials. The negative electrode is LTO and has an insertion/deinsertion potential of 1.55 V *vs.* Li^+/Li [23] which is far from the reduction potential of lithium metal. It is therefore not expected that lithium dendrites would form in such batteries. In addition, lithiated clay has been added to the GPE formulation with the objective of preventing lithium dendrite growth.

The bad full-cell performances linked to the very high and rapid capacity loss can probably be explained by the three main following hypotheses:

- The content in GPE present on each electrode might be too high. Indeed, each electrode has 50 mg/cm^2 of electrolyte, leading to a total of 188 mg of electrolyte.

This quantity is the double of what had been used for the half-cell configurations. It was decided to first test such a quantity in order to make sure that no internal short-circuit would happen. However, this might have been an extreme choice and led to high thicknesses of the GPE within the battery. This probably induced an extremely low ionic conductivity and therefore a resistance to the movement of lithium ions. Those lithium ions did not have the time to move from one electrode to the other and this led to low capacities.

- The lithium ions present in the GPE might have reacted with the residual moisture present within the electrolyte. This reaction led to the formation of lithium hydroxide and depleted the GPE of its lithium ions through the first cycles performed. In addition, as both materials used in full-cells are intercalation materials, the lithium ions present initially in the LFP positive electrode have probably reacted with the moisture as well, decreasing even more the quantity of lithium ions available. Since no other source of lithium ions was present within battery, this led to the rapid decay of the capacity of the full-cell. No decay of capacity was observed in half-cell configuration due to the presence of the lithium metal negative electrode, which is a quasi infinite source of lithium ions. Therefore, even if all of the lithium ions within the GPE would have reacted with the residual moisture, the capacity would still remain high because lithium ions were still provided by the lithium metal negative electrode.
- The connections between the GPE and the intercalation materials were probably not optimal, as well as the interface between the two GPE layers. This problem of connection was not visible for half-cell configurations. In half-cells, only one intercalation material was used, on which the electrolyte was casted and against which a flat lithium metal negative electrode was placed. The lithium metal negative electrode provides a lot of lithium ions and can therefore mask some of the connection issues between the electrolyte and the intercalation electrode. In addition, the lithium metal negative electrode was pressed against the GPE layer and the reduction of lithium ions and oxidation of lithium metal could occur directly at the surface of the electrolyte. In the full-cells studied, both electrodes had GPE casted on their surface and were then pressed together. The insertion and deinsertion reactions in intercalation materials are more challenging than the reactions associated to lithium metal. In addition, the connections between the electrode material and the electrolyte, as well as between the surface of both electrolyte layers, might be inadequate and led to a hindered movement of ions.

Different configurations have been studied to try to enhance the performances of batteries containing GPE. Those configurations and the results are presented in the following section.

4.3.3.2 Second cycling tests performed: decrease of the overall quantity of GPE

To determine if the quantity of GPE and the way this electrolyte is casted on the electrodes have major effects on battery performances, different configurations have been studied, as

explained earlier. The total quantity of GPE has been divided by 2, leading to 94 mg in total in the batteries.

The galvanostatic results concerning the configuration with 10 mg/cm^2 of GPE on the LTO electrode and 40 mg/cm^2 of GPE on the LFP electrode, leading to a total of 94 mg of GPE in the battery, can be seen in Figure 4.5.

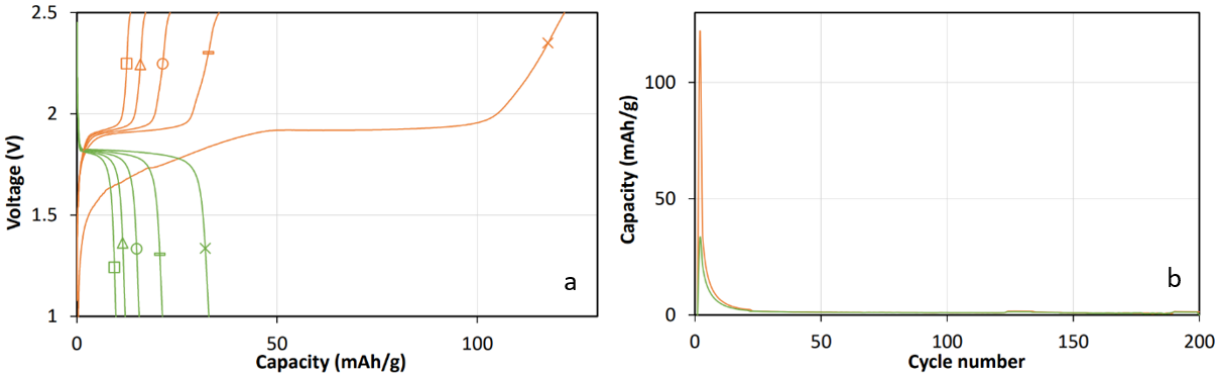

Figure 4.5: Results of galvanostatic charge and discharge for one LFP/LTO GPE full-cell sample with 10 mg/cm^2 of GPE on the LTO electrode and 40 mg/cm^2 of GPE on the LFP electrode. The capacity is expressed in mAh/g$_{\text{LFP}}$. For simplicity, the subscript LFP is not written in the Figures. a) Voltage profiles as a function of capacity at a C-rate of C/5. The charge and discharge profiles are respectively in orange and green. First cycle: (×). Second cycle: (▭). Third cycle: (○). Fourth cycle: (△). Fifth cycle: (□). b) Orange line: Charge capacity upon cycling at different C-rates. Green line: Discharge capacity upon cycling at different C-rates.

Figure 4.5a shows the voltage profiles as a function of capacity for the five first charges and discharges of the battery. It can be observed that the first charge leads to a capacity of 121 mAh/g. The voltage plateau associated to this charge is flatter than the one observed in Figure 4.4a. When looking at the first discharge, a discharge capacity of 32 mAh/g is observed, meaning that a capacity loss of 74% occurred. Afterwards, the second charge has a maximum value of capacity similar to the first discharge, while the second discharge leads once again to a capacity loss, smaller than the first one. The following charges and discharges evolve in the same way, with a capacity loss occurring at each cycle. Figure 4.5b shows the evolution of the charge and discharge capacities as a function of the cycles performed. It can be observed that both capacities become negligible after about 25 cycles and remain around 1 mAh/g.

The galvanostatic results concerning the configuration with 25 mg/cm^2 of GPE on the LTO electrode and 25 mg/cm^2 of GPE on the LFP electrode, leading to a total of 94 mg of GPE in the battery, can be seen in Figure 4.6.

Figure 4.6a shows the voltage profiles as a function of capacity for the five first charges and discharges of the battery and is very similar to Figure 4.5a. It can be seen that the first charge allows to obtain a capacity of 109 mAh/g. The voltage plateau is once again flatter than in Figure 4.4a. Concerning the evolution of the charge and discharge capacities, the

results are very similar to what was obtained for Figure 4.5b, with a decay of the charge and discharge capacities until the 25th cycle and a value around 1 mAh/g after that.

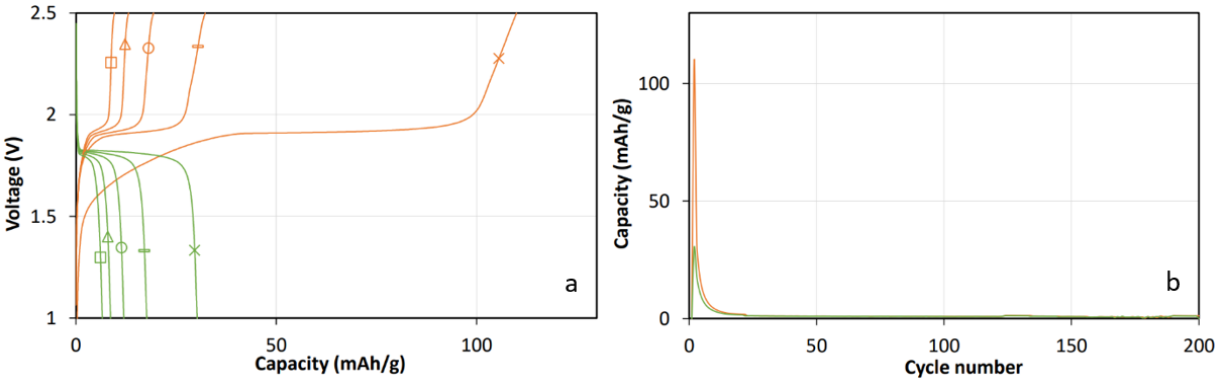

Figure 4.6: Results of galvanostatic charge and discharge for one LFP/LTO GPE full-cell sample with 25 mg/cm^2 of GPE on the LTO electrode and 25 mg/cm^2 of GPE on the LFP electrode. The capacity is expressed in mAh/g$_{LFP}$. For simplicity, the subscript LFP is not written in the Figures. a) Voltage profiles as a function of capacity at a C-rate of C/5. The charge and discharge profiles are respectively in orange and green. First cycle: (×). Second cycle: (▭). Third cycle: (○). Fourth cycle: (△). Fifth cycle: (□). b) Orange line: Charge capacity upon cycling at different C-rates. Green line: Discharge capacity upon cycling at different C-rates.

Concerning the different configurations investigated, it can be seen that both configurations lead to similar results and that the repartition of the GPE on both electrodes does not play such a big role on the cycling performances.

Finally, it is concluded that the performances are still not sufficient for an efficient battery operation. Indeed, the capacity decreases and is very low after 25 cycles, which is really mediocre in terms of performances. This capacity decrease is probably impacted by bad connections between the electrolyte and the intercalation materials. However, the hypothesis which seems the most probable and the most impacting concerning the loss of capacity is the reaction of lithium ions with moisture within the electrolyte.

4.3.4 Cycling Results: Water-in-salt electrolyte

The results of galvanostatic cycling of the LFP/LTO battery with the water-in-salt electrolyte can be seen in Figure 4.7. Similar results were obtained for different samples and only one is shown here.

It can be seen from Figure 4.7a that the battery charged at the first cycle applied at C/5 but lost its capacity in the first discharge, leading to a capacity extremely close to 0 mAh/g for the following cycles. Figure 4.7b confirms this observation, as a unique charge capacity peak is observed and the rest of the charge and discharge capacities are negligible.

Those results were expected and can probably be associated to the decomposition of the electrolyte. Indeed, it was seen in the literature that the electrolyte was supposed to be

stable from around 1.9 V until 4.9 V *vs.* Li^+/Li [56] and a stability window from 2.5 V to 4.92 V *vs.* Li^+/Li was found through experiments. Knowing that the potential of the LTO negative electrode was around 1.55 V *vs.* Li^+/Li [23], it was expected that the use of the water-in-salt electrolyte in full LFP/LTO batteries would lead to electrolyte decomposition. This decomposition led to the formation of hydrogen inside the battery *via* the hydrogen evolution reaction (Equation 2.5) occurring at the negative electrode.

Those results show that the electrolyte is even less stable in full-cell configuration than in the half-cell configuration studied, as expected.

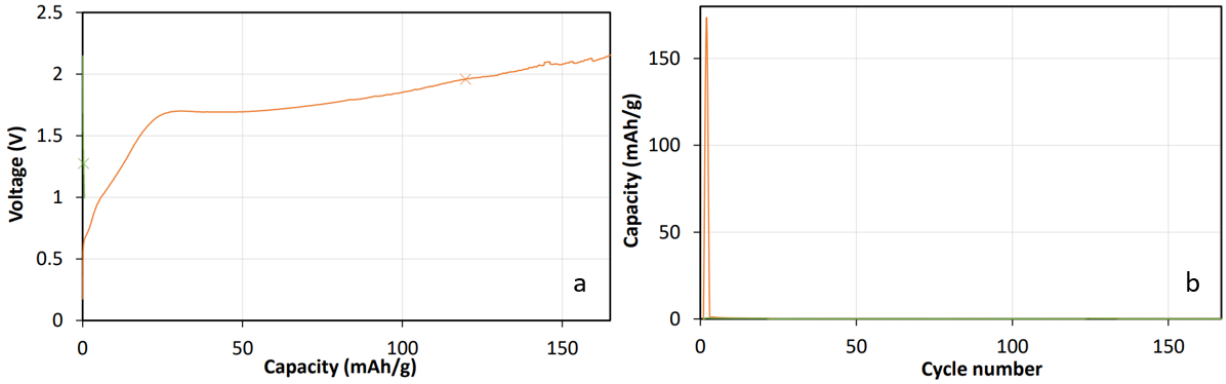

Figure 4.7: Results of galvanostatic charge and discharge for one LFP/LTO full-cell sample with the water-in-salt electrolyte. The capacity is expressed in mAh/g_{LFP}. For simplicity, the subscript LFP is not written in the Figures. a) Voltage profiles as a function of capacity at a C-rate of C/5. The charge and discharge profiles are respectively in orange and green. First cycle: (×). Second cycle: (▭). b) Orange line: Charge capacity upon cycling at different C-rates. Green line: Discharge capacity upon cycling at different C-rates.

The hypothesis of decomposition of the electrolyte is also supported by the appearance of drops on the seal of the coin cells, shown in Figure 4.8. The drops might have appeared due to the production of hydrogen, which pushed unreacted electrolyte outside of the cell due to a pressure change.

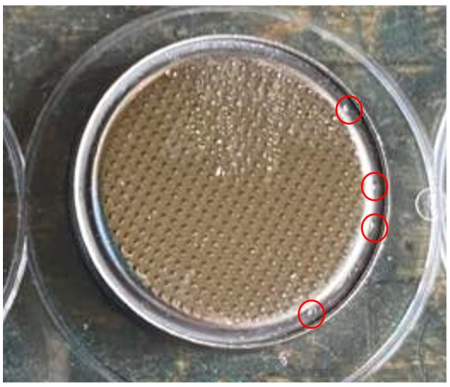

Figure 4.8: Drops formed on the seal of the coin cells during cycling. The drops are indicated by the red circles.

The cells were disassembled after cycling to observe the state of the materials, which can be seen in Figure 4.9. Both electrodes seem to be in good shape based on their exterior appearance. However, by looking at the separators, it can be seen that the separator on the LTO side is of a darker color. This might mean that the structure of the LTO electrode was damaged during the cycling. Additional studies through X-ray diffraction might allow to observe the crystalline structure of the electrodes and determine if they were affected by the cycling and electrolyte decomposition. Moreover, performing X-ray photoelectron spectroscopy on the electrodes could allow to investigate the composition of the surface and thus determine if a change of composition occurred during cycling.

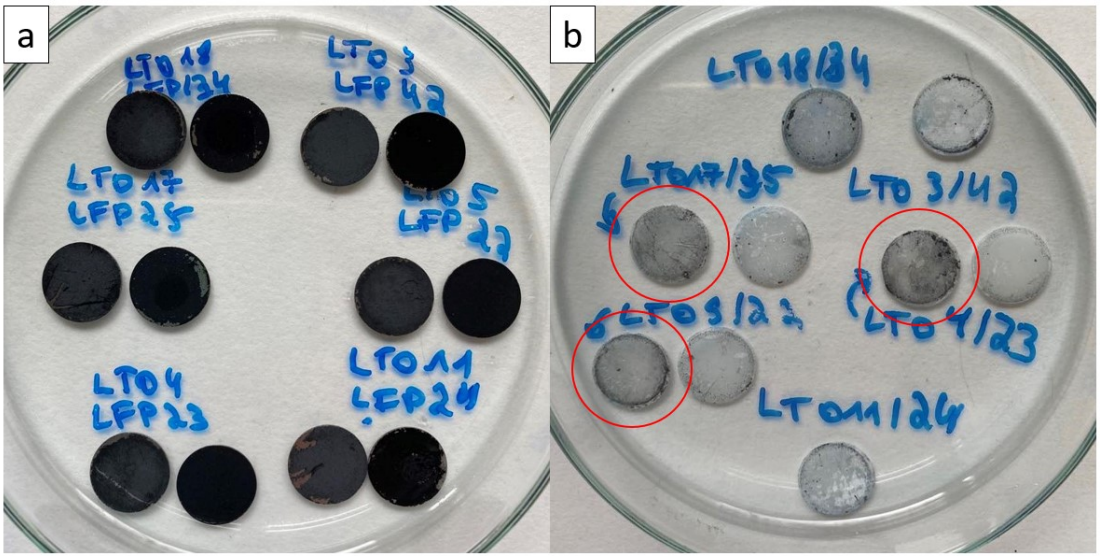

Figure 4.9: a) State of the LTO (left) and LFP (right) electrodes after cycling, five batteries have been dismantled. b) State of the separators after cycling, some separators could not be detached from each other. The separators indicated by the red circles were on the side of the LTO electrodes.

The results presented hereabove suggest that the use of the water-in-salt electrolyte in the LFP/LTO battery is not possible. However, LFP could be combined with another negative electrode with a higher potential than LTO. Nevertheless, it was seen in half-cell configuration that the stability of the electrolyte has to be investigated further, even for the LFP electrode.

4.3.5 Cyclic voltammetry results: Water-in-salt electrolyte

The cyclic voltammetry results of a LFP/LTO battery with water-in-salt electrolyte can be observed in Figure 4.10.

Figure 4.10 is in accordance with what has been observed with the galvanostatic cycling results. A first peak can be observed and then the curve keeps flattening, meaning that no capacity is associated to the battery. However, it would be expected to see current

peaks associated to the decomposition of the electrolyte, which is not the case here. The decomposition of the electrolyte is still the most probable explication of the results.

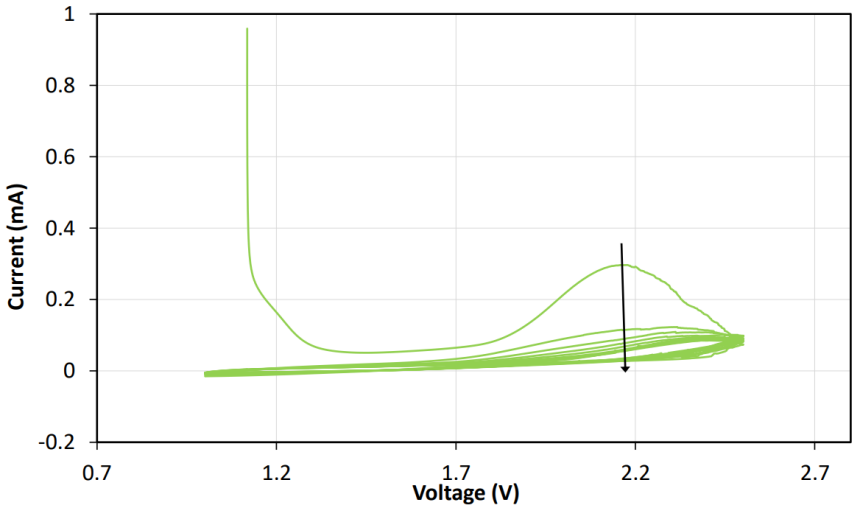

Figure 4.10: Cyclic voltammetry results for a LFP/LTO full-cell with the water-in-salt electrolyte. 11 cycles were performed at 1 mV/s and the arrow shows the direction of increasing cycles.

4.4 Conclusion and perspectives

This chapter studied full-cell configurations with LFP as positive electrode material and LTO as negative electrode material.

The results obtained with the classical liquid electrolyte, 1 M $LiPF_6$ in (1:1 vol.%) EC:DEC, showed good capacities and flat charge and discharge profiles, which give a constant voltage during battery operation. Those results therefore represent the target performances for the unconventional electrolytes studied.

The GPE was studied and the results showed that it was more challenging to obtain good battery performances in a full-cell in comparison to a half-cell. The main difference between the full-cells and half-cells investigated was that the negative electrode was no longer lithium metal in a full-cell but was an intercalation material.

It was determined that decreasing the total amount of GPE in the battery allowed to increase the cycling performances. However, those performances were still not sufficient and all the capacity was lost after 25 cycles. This loss of capacity can probably be explained by the depletion in lithium ions due to their reaction with residual moisture present in the GPE. To determine more precisely the issue with this full-cell configuration, it could be interesting to open the cells post-cycling and observe the state of the electrodes and most importantly of the GPE. If the hypothesis concerning the reaction of lithium ions with moisture is valid, the lithium hydroxide formed, which is a white compound, could probably be seen within the GPE. If it is not visible to the naked eye, it could be interesting to subject samples of pristine GPE and post-cycling GPE to X-ray diffraction, to determine

if the crystalline structure of LiOH can be observed within the GPE post-cycling.

To enhance the operation of such batteries and try to obtain sufficient performances, different possibilities can be considered:

- The amount of GPE within the battery could be decreased as much as possible while still keeping a sufficient thickness to avoid short-circuits. This could allow to obtain better capacities. However, it is not expected that this would decrease the capacity fading observed.
- To enhance the connections between the electrode materials and the GPE, different methods of casting could be applied. For example, as explained in Section 3.4, an alternate spraying of electrode material and casting of GPE or a mixing of the electrode material ink and GPE solution before spraying could be considered. Hopefully, this would enhance the connections and the ionic conductivity and lead to better performances in terms of capacity.
- The electrodes with the casted GPE could be dried at a higher temperature for a longer time to decrease as much as possible the residual moisture. However, it must be kept in mind that LiTFSI is a highly hygroscopic salt and will therefore retain moisture which will not be removed by a prolonged drying process. If full-cells assembled with electrodes and GPE subjected to an extended drying process still show a decaying capacity, it should be considered that the use of two intercalation materials with GPE is probably not a viable option.

Concerning the full-cells characterised with the water-in-salt electrolyte, it was observed that the batteries could not be cycled more than one time. This can probably be attributed to the fact that the battery does not operate completely within the electrochemical stability window of the electrolyte. The electrolyte therefore decomposes on the side of the negative electrode and leads to the production of hydrogen. This decomposition of the electrolyte hinders the battery operation. It is therefore concluded that the use of the water-in-salt electrolyte is not possible for a LFP/LTO battery.

To operate a LFP/LTO battery with such a type of aqueous electrolyte, other salt combinations could be investigated to see if the electrolyte could be more stable during operation. Such examples of electrolytes are the water-in-bisalt [57] and the water-in-hybrid-salt electrolytes [58]. However, the cost of such electrolytes would set back their commercial application. The best option to use the water-in-salt electrolyte would be to apply it in batteries with different electrodes from LFP and LTO, of which the potentials would fit completely within the stability window of the electrolyte. An example of positive electrode material could be LCO because it has a potential of 4.2 V *vs.* Li^+/Li [54], which is within the stability window of the water-in-salt electrolyte. Another example found in the literature is the use of a $LiMn_2O_4$ positive electrode and a TiO_2 negative electrode with the water-in-bisalt electrolyte mentioned previously [57].

Conclusion and perspectives

Conclusion

The main objective of this Master thesis was to investigate two safer and greener alternatives to the classical liquid organic electrolyte used in lithium-ion batteries.

First of all, the classical liquid organic electrolyte, 1 M $LiPF_6$ in (1:1 vol.%) EC:DEC, was studied. Its electrochemical stability and the cycling performances of LFP and LTO electrodes in half-cell and full-cell configurations in the presence of this electrolyte were investigated. The performances obtained served as a basis of comparison for the two less conventional electrolytes studied.

The first alternative studied was a gel polymer electrolyte, which is a semi-solid electrolyte composed of a liquid electrolyte trapped within a polymer matrix.

The electrochemical stability of this electrolyte was studied in two-electrode configuration and the results show that the GPE can be considered stable for a window of about 3-3.5 V. This electrolyte is however less stable than the classical liquid organic electrolyte.

The GPE was then characterised in half-cell configuration with LFP and LTO as positive electrode materials and lithium metal as negative electrode material. The results of galvanostatic cycling show that good cycling stability and sufficient capacities are obtained, even if they are lower than the ones obtained with the classical liquid electrolyte. However, kinetic limitations can be observed through the decrease of the capacity with increasing C-rates and through the increasing gap between the charge and discharge curves with increasing C-rates. Those kinetic limitations can be associated to the limited ionic conductivity of the GPE, mainly due to its crystalline phase.

Afterwards, the GPE was characterised in full-cell configuration, with a LFP positive electrode and a LTO negative electrode. The only sources of lithium ions were therefore the lithium ions present in the GPE and the lithium ions intercalated in the LFP positive electrode. The galvanostatic cycling results show that the capacity is lost very quickly, even when the amount of GPE is decreased. The hypothesis which seems the most plausible for this rapid capacity loss is the reaction of lithium ions with residual moisture within the electrolyte. This reaction leads to the production of LiOH and ultimately depletes completely the cell of its mobile lithium ions. In addition, the connections between the electrode material and the GPE are probably not optimal and participate to the capacity loss.

The second alternative studied was the water-in-salt electrolyte, composed of a 21 $mol/kg_{solvent}$ LiTFSI aqueous solution. The high concentration of salt allows to widen the electrochemical stability window of aqueous electrolytes, usually limited to 1.23 V.

The electrochemical stability of the electrolyte was studied in two-electrode and three-electrode configurations. The results show an electrochemical stability window of 2.42 V, from 2.5 V to 4.92 V *vs.* Li^+/Li. This window therefore restricts the choice of electrode material which can be used. Indeed, theoretically, LFP can be used as electrode material within such a window because its insertion/deinsertion potential is around 3.45 V *vs.* Li^+/Li [21] but LTO cannot be used as electrode material as its insertion/deinsertion potential is around 1.55 V *vs.* Li^+/Li [23].

The water-in-salt electrolyte was then characterised in half-cell configuration, using a three-electrode system for the LFP positive electrode. In this case the LFP positive electrode could not be characterised against lithium metal in a two-electrode system due to the aqueous base of the electrolyte. Therefore, the counter electrode selected was an activated carbon fabric, the reference electrode was Ag^+/Ag and the three-electrode system was a Swagelok T-cell. The results of cycling show that even if the insertion/deinsertion potential of LFP is within the stability window measured for the electrolyte, the cycling results are not satisfactory. The galvanostatic cycling results show that capacity is lost at each cycle. This can probably be explained by the instability of the electrolyte during cycling, even if the electrolyte was considered stable at the cycling conditions through the cyclic voltammetry results.

Finally, the water-in-salt electrolyte was characterised in full-cell configuration with a LFP positive electrode and LTO negative electrode. It was expected that due to the LTO negative electrode, the cell would not be viable due to operation outside the electrochemical stability window of the electrolyte. The results of galvanostatic cycling indeed show that the capacity is lost completely in the first cycle. It is expected that this is due to the decomposition of the electrolyte through the hydrogen evolution reaction and confirms that LTO cannot be used as electrode material with the 21 $mol/kg_{solvent}$ LiTFSI electrolyte.

Perspectives

To go further into the study of both electrolytes, different strategies could be considered.

Concerning the GPE, different possibilities could be considered to improve its performances in half-cell configuration:

- The amount of GPE casted on the electrodes could be reduced. This would decrease the thickness of the GPE layer and therefore lead to an easier movement of lithium ions between both electrodes, especially at higher C-rates. The thickness of this layer would have to optimised to be as thin as possible while avoiding internal short-circuits.
- The connections between the electrode materials and the GPE could be improved by performing a simultaneous spraying of electrode material and casting of GPE. The electrode material would be sprayed in different sequences to obtain multiple layers of material. In between each layer of electrode material, a specific amount of GPE would be casted to fill the void fraction of the electrode material. This quantity of GPE has to be determined precisely to fill the void fraction without forming an

insulating layer of GPE between the layers of electrode material.

- The connections between the electrode materials and the GPE could be improved by mixing the ink of electrode material and part of the solution of GPE before the spray-coating process. The resulting electrodes would contain a mix of active material, binder, conducting carbon and GPE. In addition, a thin layer of GPE would be casted on the electrodes to avoid internal short-circuits.

Concerning the use of GPE in full-cell configuration, the following strategies could be applied to enhance the performances:

- The thickness of the GPE layer could once again be decreased, to enhance the ionic conductivity.
- The connections between the electrode materials and the GPE could be enhanced by applying different casting methods, as explained for half-cells.
- The GPE-casted electrodes could be subjected to a more severe drying process to remove as much moisture as possible. However, it is expected that due to the highly hygroscopic behaviour of LiTFSI, all of the residual moisture cannot be removed.

When focusing on the water-in-salt electrolyte, the following aspects should be investigated for both the half-cell and full-cell configurations:

- The stability of the electrolyte should be studied deeper as it was seen that even when the electrode material had an insertion/deinsertion potential within the stability window, the cycling performances were insufficient.
- The compatibility of the water-soluble binder and the electrolyte during cycling should be investigated.
- Changing the nature of the salt, combining different salts and increasing the salt concentrations could be interesting to obtain an electrolyte with a wider electrochemical stability window.
- Other electrode materials, of which the insertion/deinsertion potentials would fit completely within the stability window of the electrolyte, should be investigated.

When comparing both alternatives, the water-in-salt electrolyte seems the least probable to have commercial applications. Indeed, even if the electrochemical stability window of the water-in-salt electrolyte is wider than the ones of the classical aqueous electrolytes, it is still not wide enough when considering what is done commercially with the classical liquid organic electrolyte. In addition, from the economical point of view, the high concentration of salt required to increase the width of the window and the high cost of the lithium salts will lead to high overall production costs. Concerning the GPE, it could be a good candidate to replace the classical liquid organic electrolyte. However, the capacities obtained during cycling should first be optimised by enhancing the ionic conductivity of the GPE.

Research is therefore still needed concerning different aspects of both the gel polymer and water-in-salt electrolytes before the classical liquid organic electrolyte can be dethroned.

Bibliography

[1] Dunn, B., Kamath, H. & Tarascon, J-M., 2011. Electrical Energy Storage for the Grid: A Battery of Choices. *Science*, 334, 928-935. https://doi.org/10.1126/science.1212741

[2] Yan, H., Zhang, D., Qilu, Duo, X. & Sheng, X., 2021. A review of spinel lithium titanate ($Li_4Ti_5O_{12}$) as electrode material for advanced energy storage devices. *Ceramics International*, 47, 5870-5895. https://doi.org/10.1016/j.ceramint.2020.10.241

[3] Wen, J., Yu, Y. & Chen, C., 2012. A Review on Lithium-Ion Batteries Safety Issues: Existing Problems and Possible Solutions. *Materials Express*, 2, 197-212. https://doi.org/10.1166/mex.2012.1075

[4] Mekonnen, Y., Sundararajan, A. & Sarwat, A.I., 2016. A review of cathode and anode materials for lithium-ion batteries. *SoutheastCon 2016*, Norfolk, VA, USA, 1-6. https://doi.org/10.1109/SECON.2016.7506639

[5] Li, J., Daniel, C. & Wood, D., 2011. Materials processing for lithium-ion batteries. *Journal of Power Sources*, 196, 2452-2460. https://doi.org/10.1016/j.jpowsour.2010.11.001

[6] Roy, P. & Srivastava, S.K., 2015. Nanostructured anode materials for lithium ion batteries. *Journal of Materials Chemistry A*, 3, 2454-2484. https://doi.org/10.1039/C4TA04980B

[7] Xu, B., Qian, D., Wang, Z. & Meng, Y.S., 2012. Recent progress in cathode materials research for advanced lithium ion batteries. *Materials Science and Engineering R*, 73, 51-65. http://doi.org/10.1016/j.mser.2012.05.003

[8] Chung, D.D.L., 2002. Review Graphite. *Journal of Materials Science*, 37, 1475-1489. https://doi.org/10.1023/A:1014915307738

[9] Teshima, K., Inagaki, H., Tanaka, S., Yubuta, K., Hozumi, M., Kohama, K., Shishido, T. & Oishi, S., 2011. Growth of Well-Developed $Li_4Ti_5O_{12}$ Crystals by the Cooling of a Sodium Chloride Flux. *Crystal Growth and Design*, 11, 4401-4405. https://doi.org/10.1021/cg200578r

[10] Wang, Q., Jiang, L., Yu, Y. & Sun, J., 2019. Progress of enhancing the safety of lithium ion battery from the electrolyte aspect. *Nano Energy*, 55, 93-114. https://doi.org/10.1016/j.nanoen.2018.10.035

[11] Aravindan, V., Gnanaraj, J., Madhavi, S. & Liu, H-K., 2011. Lithium-Ion Conducting Electrolyte Salts for Lithium Batteries. *Chemistry A European Journal*, 17, 14326-14346. https://doi.org/10.1002/chem.201101486

[12] Hess, S., Wohlfahrt-Mehrens, M. & Wachtler, M., 2015. Flammability of Li-Ion Battery Electrolytes: Flash Point and Self-Extinguishing Time Measurements. *Journal of The Electrochemical Society*, 162, A3084-A3097. https://doi.org/10.1149/2.0121502jes

[13] Balakrishnan, P.G., Ramesh, R. & Prem Kumar, T., 2006. Safety mechanisms in lithium-ion batteries. *Journal of Power Sources*, 155, 401-414. https://doi.org/10.1016/j.jpowsour.2005.12.002

[14] Zhu, M., Wu, J., Wang, Y., Song, M., Long, L., Siyal, S.H., Yang, X. & Sui, G., 2019. Recent advances in gel polymer electrolyte for high-performance lithium batteries. *Journal of Energy Chemistry*, 37, 126-142. https://doi.org/10.1016/j.jechem.2018.12.013

[15] Shen, Y., Liu, B., Liu, X., Liu, J., Ding, J., Zhong, C. & Hu, W., 2021. Water-in-salt electrolyte for safe and high-energy aqueous battery. *Energy Storage Materials*, 34, 461-474. https://doi.org/10.1016/j.ensm.2020.10.011

[16] Suo, L., Borodin, O., Gao, T., Olguin, M., Ho, J., Fan, X., Luo, C., Wang, C. & Xu, K., 2015. "Water-in-salt" electrolyte enables high-voltage aqueous lithium-ion chemistries. *Science*, 350, 938-943. https://doi.org/10.1126/science.aab1595

[17] Léonard, A., Piedboeuf, M-L. & Job, N., 2017. WO2017211555 - Process To Prepare An Electrode For An Electrochemical Storage Device. https://patentscope.wipo.int/search/en/detail.jsf?docId=WO2017211555

[18] Li, J., Fleetwood, J., Hawley, W.B. & Kays, W., 2022. From Materials to Cell: State-of-the-Art and Prospective Technologies for Lithium-Ion Battery Electrode Processing. *Chemical Reviews*, 122, 903-956. https://doi.org/10.1021/acs.chemrev.1c00565

[19] Gonçalves, R., Lanceros-Méndez, S. & Costa, C.M., 2022. Electrode fabrication process and its influence in lithium-ion battery performance: State of the art and future trends. *Electrochemistry Communications*, 135, 107210. https://doi.org/10.1016/j.elecom.2022.107210

[20] Job, N., 2022. Electrochemical energy conversion and storage CHIM0664: Chapter 3 - Description of electrochemical cells. Course at the University of Liège, Belgium.

[21] Léonard, A.F. & Job, N., 2019. Safe and green Li-ion batteries based on $LiFePO_4$ and $Li_4Ti_5O_{12}$ sprayed as aqueous slurries with xanthan gum as common binder. *Materials Today Energy*, 12, 168-178. https://doi.org/10.1016/j.mtener.2019.01.008

[22] Whittingham, M.S., 2004. Lithium Batteries and Cathode Materials. *Chemical Reviews*, 104, 4271-4302. https://doi.org/10.1021/cr020731c

[23] Sandhya, C.P., John, B. & Gouri, C., 2014. Lithium titanate as anode material for lithium-ion cells: a review. *Ionics*, 20, 601-620. https://doi.org/10.1007/s11581-014-1113-4

[24] Warner, J.T., 2019. Chapter 3 - Lithium-ion battery operation. *In*: Warner, J.T. *Lithium-Ion Battery Chemistries: A Primer*, Elsevier, 139-170. https://doi.org/10.1016/B978-0-12-814778-8.00003-X

[25] Warner, J.T., 2019. Chapter 6 - The Anodes. *In*: Warner, J.T. *Lithium-Ion Battery Chemistries: A Primer*, Elsevier, 115-138. https://doi.org/10.1016/B978-0-12-814778-8.00006-5

[26] Zhang, Y., Huo, Q-Y., Du, P-P., Wang, L-Z., Zhang, A-Q., Song, Y-H., Lv, Y. & Li, G-Y., 2012. Advances in new cathode material $LiFePO_4$ for lithium-ion batteries. *Synthetic Metals*, 162, 1315-1326. https://doi.org/10.1016/j.synthmet.2012.04.025

[27] Warner, J.T., 2019. Chapter 5 - The Cathodes. *In*: Warner, J.T. *Lithium-Ion Battery Chemistries: A Primer*, Elsevier, 99-114. https://doi.org/10.1016/B978-0-12-814778-8.00005-3

[28] Kasnatscheew, J., Placke, T., Streipert, B., Rothermel, S., Wagner, R., Meister, P., Laskovic, I.C. & Winter, M., 2017. A Tutorial into Practical Capacity and Mass Balancing of Lithium Ion Batteries. *Journal of The Electrochemical Society*, 164, A2479-A2486. https://doi.org/10.1149/2.0961712jes

[29] Piedboeuf, M-L., 2016. Xérogels de carbone comme matériaux modèles pour l'étude du comportement électrochimique en tant qu'anodes de batteries Li-ion. PhD thesis. University of Liège. 251p.

[30] Zhang, Z.J., Ramadass, P. & Fang, W., 2014. 18 - Safety of Lithium-Ion Batteries. *In*: Pistoia, G. *Lithium-Ion Batteries Advances and Applications*, Elsevier, 409-435. https://doi.org/10.1016/B978-0-444-59513-3.00018-2

[31] Castaing, R., Reynier, Y., Dupré, N., Schleich, D., Jouanneau Si Larbi, S., Guyomard, D. & Moreau, P., 2014. Degradation diagnosis of aged $Li_4Ti_5O_{12}/LiFePO_4$ batteries. *Journal of Power Sources*, 267, 744-752. http://dx.doi.org/10.1016/j.jpowsour.2014.06.002

[32] Murthy, N.S., 2011. 9 - Techniques for analyzing biomaterial surface structure, morphology and topography. *In*: Williams, R. *Surface Modification of Biomaterials*, Woodhead Publishing, 232-255. https://doi.org/10.1533/9780857090768.2.232

[33] Chappard, D., Degasne, I., Huré, G., Legrand, E., Audran, M. & Baslé, M.F., 2003. Image analysis measurements of roughness by texture and fractal analysis correlate with contact profilometry. *Biomaterials*, 24, 1399-1407. https://doi.org/10.1016/S0142-9612(02)00524-0

[34] Han, D-W., Ryu, W-H., Kim, W-K., Lim, S.J. & Kwon, H-S., 2010. Synthesis of Porous $LiFePO_4/C$ Composites using $LiFePO_4$ Self-Template Prepared by Hydrother-

mal Process. *The 15th International Meeting on Lithium Batteries*, the Electrochemical Society, Abstract 392. https://doi.org/10.1149/MA2010-03/1/392

[35] Seo, J-H., Verlinde, K., Rajagopalan, R., Gomez, E.D., Mallouk, T.E. & Randall, C.A., 2019. Cold sintering process for fabrication of a high volumetric capacity $Li_4Ti_5O_{12}$ anode. *Materials Science and Engineering B*, 250, 114435. https://doi.org/10.1016/j.mseb.2019.114435

[36] Cambridge Energy Solutions, 2023. TIMCAL SUPER C65 Conductive Carbon Black Powder. https://cam-energy.com/product/timcal-super-c65-conductive-carbon-black-powder/

[37] Talukdar, M.M., Vinckier, I., Moldenaers, P. & Kinget, R., 1996. Rheological characterization of xanthan gum and hydroxypropylmethyl cellulose with respect to controlled-release drug delivery. *Journal of Pharmaceutical Sciences*, 85, 537-540. https://doi.org/10.1021/js950476u

[38] Weisstein, E.W., 2023. "Standard Deviation". From Mathworld–A Wolfram Web Resource. https://mathworld.wolfram.com/StandardDeviation.html

[39] Xu, K., 2004. Nonaqueous Liquid Electrolytes for Lithium-Based Rechargeable Batteries. *Chemical Reviews*, 104, 4303-4418. https://doi.org/10.1021/cr030203g

[40] Marcinek, M., Syzdek, J., Marczewski, M., Piszcz, M., Niedzicki, L., Kalita, M., Plewa-Marczewska, A., Bitner, A., Wieczorek, P., Trzeciak, T., Kasprzyk, M., Lezak, P., Zukowska, Z., Zalewska, A. & Wieczorek, W., 2015. Electrolytes for Li-ion transport - Review. *Solid State Ionics*, 276, 107-126. https://doi.org/10.1016/j.ssi.2015.02.006

[41] Jouyban, A., Soltanpour, S. & Chan, H-K., 2004. A simple relationship between dielectric constant of mixed solvents with solvent composition and temperature. *International Journal of Pharmaceutics*, 269, 353-360. https://doi.org/10.1016/j.ijpharm.2003.09.010

[42] Warner, J.T., 2019. Chapter 7 - Inactive materials. *In*: Warner, J.T. *Lithium-Ion Battery Chemistries: A Primer*, Elsevier, 139-170. https://doi.org/10.1016/B978-0-12-814778-8.00007-7

[43] Chagnes, A., 2015. Chapter 5 - Lithium Battery Technologies: Electrolytes. *In*: Chagnes, A. & Swiatowska, J. *Lithium Process Chemistry*, Elsevier, 167-189. https://doi.org/10.1016/B978-0-12-801417-2.00005-0

[44] Tarascon, J.M., & Guyomard, D., 1994. New electrolyte compositions stable over the 0 to 5 V voltage range and compatible with the $Li_{1+x}Mn_2O_4$/carbon Li-ion cells. *Solid State Ionics*, 69, 293-305. https://doi.org/10.1016/0167-2738(94)90418-9

[45] Chagnes, A., 2015. Chapter 2 - Fundamentals in Electrochemistry and Hydrometallurgy. *In*: Chagnes, A. & Swiatowska, J. *Lithium Process Chemistry: Resources, Extraction, Batteries and Recycling*, Elsevier, 41-80. http://doi.org/10.1016/B978-0-12-801417-2.00002-5

[46] Franger, S., Bourbon, C. & Le Cras, F., 2004. Optimized Lithium Iron Phosphate for High-Rate Electrochemical Applications. *Journal of The Electrochemical Society*, 151, A1024-A1027. https://doi.org/10.1149/1.1758721

[47] Ngai, K.S., Ramesh, S., Ramesh, K. & Juan, J.C., 2016. A review of polymer electrolytes: fundamental, approaches and applications. *Ionics*, 22, 1259-1279. https://doi.org/10.1007/s11581-016-1756-4

[48] Cheng, X., Pan, J., Zhao, Y., Liao, M. & Peng, H., 2018. Gel Polymer Electrolytes for Electrochemical Energy Storage. *Advanced Energy Materials*, 8, 1702184. https://doi.org/10.1002/aenm.201702184

[49] Porthault, H., Calberg, C., Amiran, J., Martin, S., Páez, C., Job, N., Heinrichs, B., Liquet, D. & Salot, R., 2021. Development of a thin flexible Li battery design with a new gel polymer electrolyte operating at room temperature. *Journal of Power Sources*, 482, 229055. https://doi.org/10.1016/j.jpowsour.2020.229055

[50] Wang, Y. & Zhong, W-H., 2015. Development of Electrolytes towards Achieving Safe and High-Performance Energy-Storage Devices: A Review. *ChemElectroChem*, 2, 22-36. https://doi.org/10.1002/celc.201402277

[51] Arya, A. & Sharma, A.L., 2017. Polymer electrolytes for lithium ion batteries: a critical study. *Ionics*, 23, 497-540. https://doi.org/10.1007/s11581-016-1908-6

[52] Kim, S., Kang, J.Y., Lee, S.G., Lee, J.R. & Park, S.J., 2006. Influence of Clay Addition on Ion Conductivity of Polymeric Electrolyte Composites. *Solid State Phenomena*, 111, 155-158. http://doi.org/10.4028/www.scientific.net/SSP.111.155

[53] Kim, S., Hwang, E-J., Jung, Y., Han, M. & Park, S-J., 2008. Ionic conductivity of polymeric nanocomposite electrolytes based on poly(ethylene oxide) and organoclay materials. *Colloids and Surfaces A: Physicochemical and Engineering Aspects*, 313-314, 216-219. https://doi.org/10.1016/j.colsurfa.2007.04.097

[54] Wu, Q., Zhang, B. & Lu, Y., 2022. Progress and perspective of high-voltage lithium cobalt oxide in lithium-ion batteries. *Journal of Energy Chemistry*, 74, 283-308. https://doi.org/10.1016/j.jechem.2022.07.007

[55] Kim, H., Hong, J., Park, K-Y., Kim, H., Kim, S-W. & Kang, K., 2014. Aqueous Rechargeable Li and Na Ion Batteries. *Chemical Reviews*, 114, 11788-11827. https://doi.org/10.1021/cr500232y

[56] Lv, T. & Suo, L., 2021. Water-in-salt widens the electrochemical stability window: Thermodynamic and kinetic factors. *Current Opinion in Electrochemistry*, 29, 100818. https://doi.org/10.1016/j.coelec.2021.100818

[57] Suo, L., Borodin, O., Sun, W., Fan, X., Yang, C., Wang, F., Gao, T., Ma, Z., Schroeder, M., von Cresce, A., Russel, S.M., Armand, M., Angell, A., Xu, K. & Wang, C., 2016. Advanced High-Voltage Aqueous Lithium-Ion Battery Enabled by "Water-in-Bisalt" Electrolyte. *Angewandte Chemie International Edition*, 55, 7136-7141. https://doi.org/10.1002/anie.201602397

[58] Chen, L., Zhang, J., Li, Q., Vatamanu, J., Ji, X., Pollard, T.P., Cui, C., Hou, S., Chen, J., Yang, C., Ma, L., Ding, M.S., Garaga, M., Greenbaum, S., Lee, H-S., Borodin, O., Xu, K. & Wang, C., 2020. A 63 m Superconcentrated Aqueous Electrolyte fo High-Energy Li-Ion Batteries. *ACS Energy Letters*, 5, 968-974. https://doi.org/10.1021/acsenergylett.0c00348

[59] Giurlani, W., Sergi, L., Crestini, E., Calisi, N., Poli, F., Soavi, F. & Innocenti, M., 2022. Electrochemical stability of steel, Ti and Cu current collectors in water-in-salt electrolyte for green batteries and supercapacitors. *Journal of Solid State Electrochemistry*, 26, 85-95. https://doi.org/10.1007/s10008-020-04853-2

[60] Muench, S., Wild, A., Friebe, C., Häupler, B., Janoschka, T. & Schubert, U.S., 2016. Polymer-Based Organic Batteries. *Chemical Reviews*, 116, 9438-9484. https://doi.org/10.1021/acs.chemrev.6b00070

[61] Rowden, B. & Garcia-Araez, N., 2021. Estimating lithium-ion battery behavior from half-cell data. *Energy Reports*, 7, 97-103. https://doi.org/10.1016/j.egyr.2021.02.048

[62] Nölle, R., Beltrop, K., Holtstiege, F., Kasnatscheew, J., Placke, T. & Winter, M., 2020. A reality check and tutorial on electrochemical characterization of battery cell materials: How to choose the appropriate cell setup. *Materials Today*, 32, 131-146. https://doi.org/10.1016/j.mattod.2019.07.002

[63] Heubner, C., Maletti, S., Lohrberg, O., Lein, T., Liebmann, T., Nickol, A., Schneider, M. & Michaelis, A., 2021. Electrochemical Characterization of Battery Materials in 2-Electrode Half-Cell Configuration: A Balancing Act Between Simplicity and Pitfalls. *Battery and Supercaps*, 4, 1310-1322. https://doi.org/10.1002/batt.202100075

[64] Liu, B., Zhang, J-G. & Xu, W., 2018. Advancing Lithium Metal Batteries. *Joule*, 2, 833-845. https://doi.org/10.1016/j.joule.2018.03.008

[65] Kim, T., Choi, W., Shin, H-C., Choi, J-Y., Kim, J.M., Park, M-S. & Yoon, W-S., 2020. Applications of Voltammetry in Lithium Ion Battery Research. *Journal of Electrochemical Science and Technology*, 11, 14-25. https://doi.org/10.33961/jecst.2019.00619

[66] Handa, N., Sugimoto, T., Yamagata, M., Kikuta, M., Kono, M. & Ishikawa, M., 2008. A neat ionic liquid electrolyte based on FSI anion for electric double layer capacitor. *Journal of Power Sources*, 185, 1585-1588. https://doi.org/10.1016/j.jpowsour.2008.08.086

[67] Job, N., 2022. Electrochemical energy conversion and storage CHIM0664: Chapter 4 - Real cells. Course at the University of Liège, Belgium.

[68] Yang, F., Wang, D., Zhao, Y., Tsui, K-L. & Bae, S.J., 2018. A study of the relationship between coulombic efficiency and capacity degradation of commercial lithium-ion batteries. *Energy*, 145, 486-495. https://doi.org/10.1016/j.energy.2017.12.144

[69] Smith, A.J., Burns, J.C., Trussler, S. & Dahn, J.R., 2010. Precision Measurements of the Coulombic Efficiency of Lithium-Ion Batteries and of Electrode Materials for Lithium-Ion Batteries. *Journal of The Electrochemical Society*, 157, A196-A202. https://doi.org/10.1149/1.3268129

[70] Yue, X., Kiely, J., Ghauri, S., Kauer, M., Bellanger, M. & Gibson, D., 2017. A successive approximation method to precisely measure leakage current of the rechargeable Lithium coin battery. *Journal of Energy Storage*, 13, 442-446. http://dx.doi.org/10.1016/j.est.2017.08.006

[71] Bard, A.J. & Faulkner, L.R., 2000. Chapter 1 - Introduction and Overview of Electrode Processes. *In:* Bard, A.J. & Faulkner, L.R. *Electrochemical Methods: Fundamentals and Applications, 2nd Edition*, Wiley, 1-43.

Appendices

Electrode manufacturing

Active material masses obtained during spray-coating

Table A.1: Active material masses, average active material mass and standard deviation of a batch of 15 LFP electrodes produced *via* spray-coating.

LFP electrode n°	LFP active material mass (mg)
1	3.1
2	3
3	2.9
4	2.9
5	2.9
6	3.2
7	3.3
8	3.1
9	3
10	3
11	3.3
12	3.2
13	3.2
14	3.1
15	3
Average active material mass (mg)	3.1
Standard deviation (mg)	0.1

Contact profilometry results

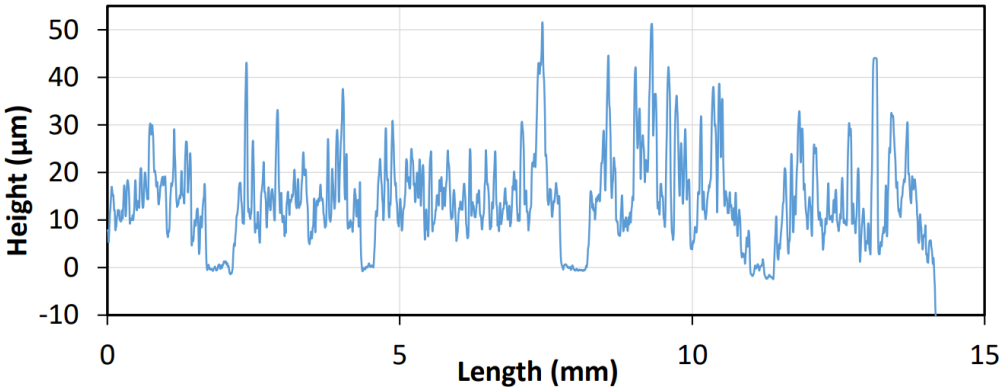

Figure A.1: Profilometry results for the LTO electrode, second measurement.

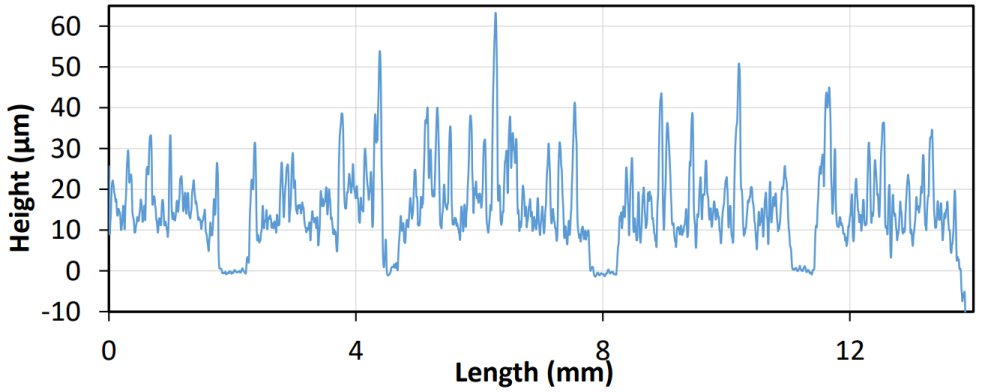

Figure A.2: Profilometry results for the LTO electrode, third measurement.

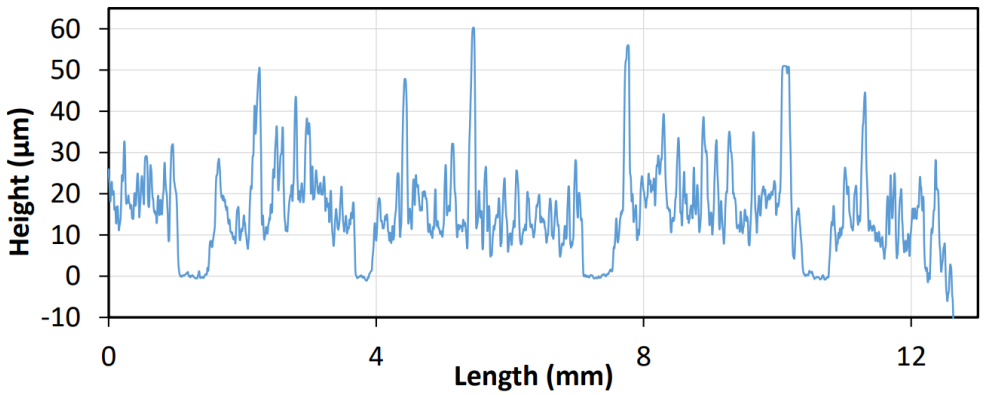

Figure A.3: Profilometry results for the LTO electrode, fourth measurement.

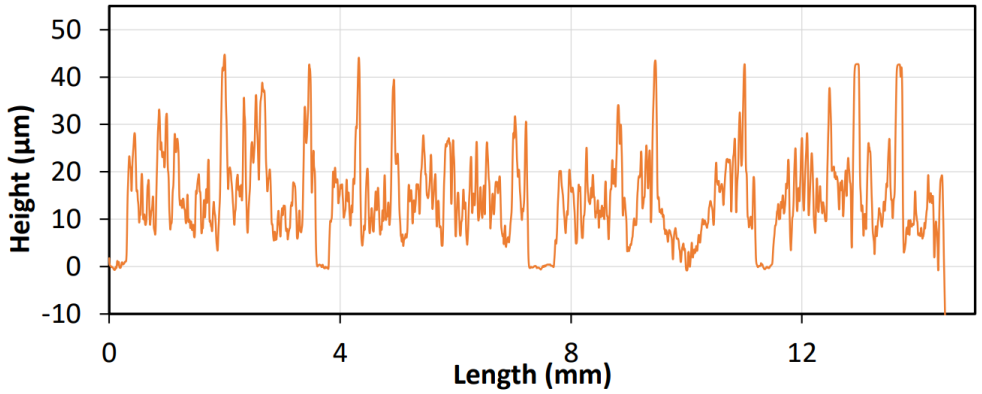

Figure A.4: Profilometry results for the LFP electrode, second measurement.

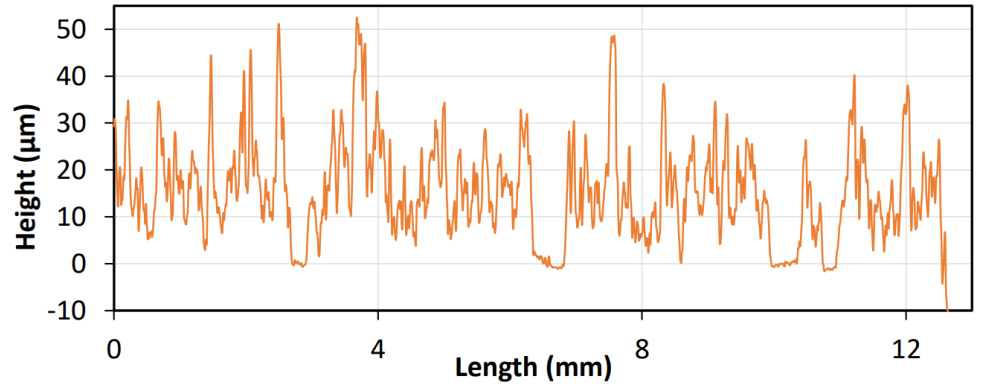

Figure A.5: Profilometry results for the LFP electrode, third measurement.

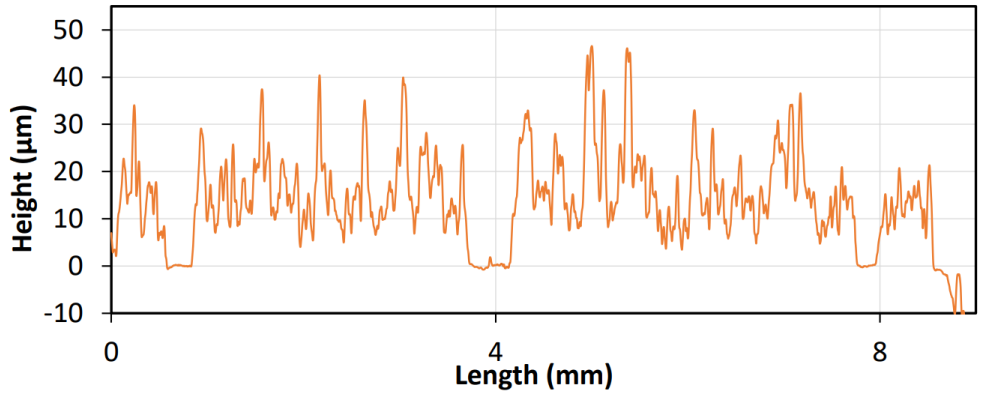

Figure A.6: Profilometry results for the LFP electrode, fourth measurement.

Electrolyte study

Water-in-salt: Electrode stability

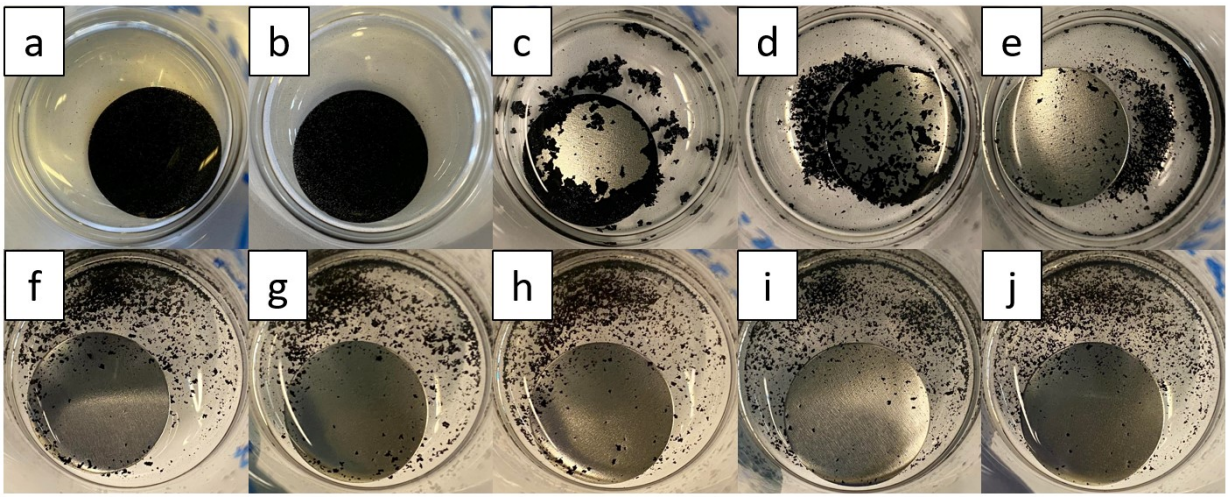

Figure A.7: Degradation of electrode W2 in MilliQ water: a) t_0, b) t_0 + 1 h, c) t_0 + 19 h, d) t_0 + 21 h, e) t_0 + 27 h, f) t_0 + 43 h, g) t_0 + 49 h, h) t_0 + 115 h, i) t_0 + 166 h, j) t_0 + 213 h.

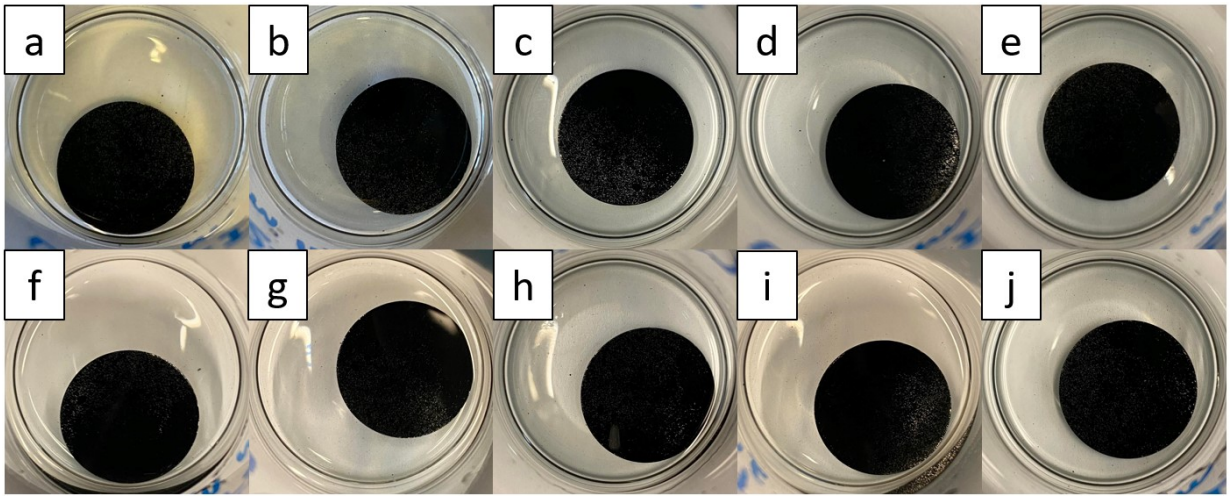

Figure A.8: Degradation of electrode W4 in the LiTFSI 21 mol/$kg_{solvent}$ aqueous solution: a) t_0, b) t_0 + 1 h, c) t_0 + 19 h, d) t_0 + 21 h, e) t_0 + 27 h, f) t_0 + 43 h, g) t_0 + 49 h, h) t_0 + 115 h, i) t_0 + 166 h, j) t_0 + 213 h.

Water-in-salt: Cyclic voltammetry results: three-electrode system

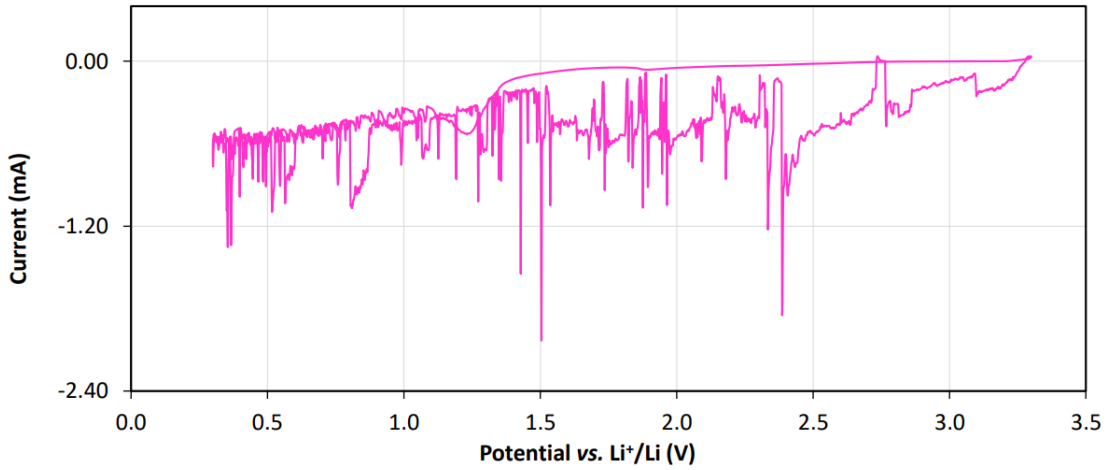

Figure A.9: Cyclic voltammetry results: water-in-salt electrolyte in three-electrode system: complete anodic results, scan rate of 0.05 mV/s.

Half-cell characterisation

Water-in-salt electrolyte

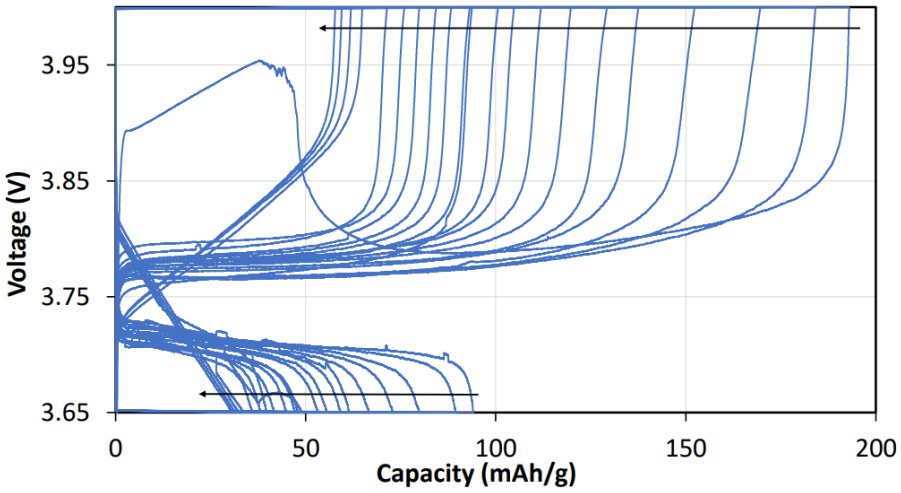

Figure A.10: Results of galvanostatic charge and discharge for the three-electrode system containing the LFP electrode, the Ag^+/Ag reference, the activated carbon fabric negative electrode and the water-in-salt electrolyte. All of the cycles at C/5 are shown. The successive cycles are indicated by the directions of the arrows.

Full-cell characterisation

1 M $LiPF_6$ in (1:1 vol.%) EC:DEC

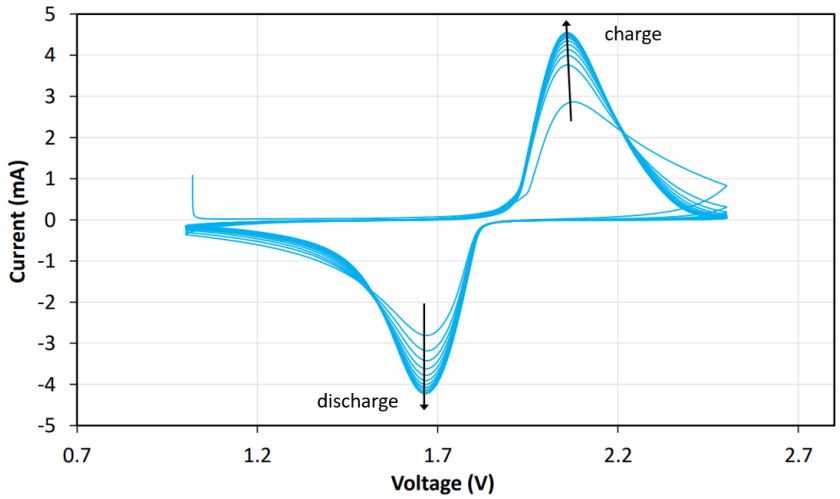

Figure A.11: Cyclic voltammetry results of a LFP/LTO battery sample with 1 M $LiPF_6$ in (1:1 vol.%) EC:DEC electrolyte. Scan rate of 1 mV/s. 11 cycles were performed, the directions of the arrows indicate the increasing cycles.